Ad suppl.

COO-3060-6
MITNE-143

LMFBR BLANKET PHYSICS PROJECT PROGRESS REPORT NO. 3

June 30, 1972

Department of Nuclear Engineering
Massachusetts Institute of Technology
Cambridge, Massachusetts 02139

Contract AT(11-1)-3060
U.S. Atomic Energy Commission

MASSACHUSETTS INSTITUTE OF TECHNOLOGY
DEPARTMENT OF NUCLEAR ENGINEERING
Cambridge, Massachusetts 02139

COO-3060-6 MITNE-143
AEC Research and Development Contract
UC-34 Physics

LMFBR BLANKET PHYSICS PROJECT PROGRESS REPORT NO. 3

June 30, 1972

Contract AT(11-1)3060

U.S. Atomic Energy Commission

Editors:

M.J. Driscoll
D.D. Lanning
I. Kaplan

Contributors:

S.T. Brewer
G.J. Brown
P. Delaquil
M.J. Driscoll
G.A. Ducat
I.A. Forbes
M.V. Gregory
S.Y. Ho
M.S. Kalra
C.S. Kang
L.T. Kim
D.D. Lanning
J.L. Lazewatsky
T.C. Leung
E.A. Mason
N.R. Ortiz
N.C. Rasmussen
I.C. Rickard
K.D. Roberson
A.T. Supple
A.M. Thompson
C.P. Tzanos

DISTRIBUTION

COO-3060-6 MITNE-143

AEC Research and Development Contract

AT(11-1)3060

UC-34 Physics

1-3. U.S. Atomic Energy Commission, Headquarters
Division of Reactor Development and Technology
Reactor Physics Branch

4,5. U.S. Atomic Energy Commission
Cambridge Office

6. Dr. Paul Greebler, Manager
Nuclear Energy Division
Breeder Reactor Department
General Electric Company
310 DeGuigne Drive
Sunnyvale, California 94086

7. Dr. Harry Morewitz, Manager
LMFBR Physics and Safety Projects
Atomics International
P.O. Box 309
Canoga Park, California 91305

8. Mr. Malcolm Dyos, Manager
Nuclear Development, LMFBR Project
Westinghouse Electric Corporation
Advanced Reactors Division
Waltz Mill Site
P.O. Box 158
Madison, Pennsylvania 15663

9. Dr. Robert Avery, Director
Reactor Physics Division
Argonne National Laboratory
9700 South Cass Avenue
Argonne, Illinois 60439

10. Dr. Charles A. Preskitt, Jr., Manager
Atomic and Nuclear Department
Gulf Radiation Technology
P.O. Box 608
San Diego, California 92112

ABSTRACT

This is the third annual report of an experimental program for the investigation of the neutronics of benchmark mock-ups of LMFBR blankets.

During the period covered by the report, July 1, 1971 through June 30, 1972, work was devoted to completion of data analysis on Blanket Mock-Up No. 2, a simulation of a typical large LMFBR radial blanket and its steel reflector; and to experimental measurements on Blanket Mock-Up No. 3, a graphite reflected blanket.

Extensive instrumental neutron spectroscopy data from Blanket Mock-Up No. 2 (from He-3, Li-6 and p-recoil spectrometers) are analyzed; as are foil activation traverses from Mock-Up No. 3. Some systematic discrepancies are noted, but in general the agreement between multigroup calculations and the experimental data is good.

Analysis of advanced blanket configurations is also reported.

TABLE OF CONTENTS

LIST OF FIGURES

LIST OF TABLES

1. INTRODUCTION

1.1 Foreword

This is the third annual report of the LMFBR Blanket Physics Project. This report covers work done since the last progress report, Reference 1, during the time period from July 1, 1971 through June 30, 1972.

The MIT Blanket Research Project is part of the AEC's LMFBR development program, having as its primary objective the experimental investigation of clean, but realistic, benchmark mock-ups of the blanket-reflector region of large LMFBR reactors. The key experimental tool used in this work is the Blanket Test Facility at the MIT Research Reactor, which contains a fission-converter plate tailored to deliver a spectrum simulating LMFBR core leakage and used to drive blanket mock-ups.

Blanket subassemblies are constructed of uranium metal fuel rods, clad in carbon steel, surrounded by anhydrous sodium chromate. The homogenized mixture closely simulates UO_2 fuel, stainless steel clad and sodium metal coolant.

To date, two blankets have been investigated: No. 2, a three-subassembly-row, steel reflected mock-up of a typical large LMFBR design; and No. 3, a two-row, graphite reflected mock-up of an advanced design.

1.2 Work Areas

During the report period, work was carried out in the following areas:

1. analysis of instrumental neutron spectrometry data collected on Blanket Mock-Up No. 2 (Chapter 2);

2. intensification of the efforts on the development and improvement of foil methods for neutron spectrometry (Chapter 3);

3. analysis of foil activation traverses in Mock-Up No. 3 (Chapter 4);

4. extensive experimental and theoretical work on the phenomenon of U^{238} self shielding (Chapter 5);

5. continued engineering and economic evaluations of advanced blanket configurations (Chapters 6 and 7);

6. parametric studies in support of blanket design and analysis of experimental results (Chapter 8).

In the final chapter, general trends are noted and the projected future research program is outlined.

1.3 Staff

The project staff, including thesis students, during the report period was as follows:

*M.J. Driscoll, Associate Professor of Nuclear Engineering, Project Director
*I. Kaplan, Professor of Nuclear Engineering
*D.D. Lanning, Professor of Nuclear Engineering
†E.A. Mason, Professor of Nuclear Engineering
N.C. Rasmussen, Professor of Nuclear Engineering
I.A. Forbes, DSR Staff (Summer 1971, 1972)
C.P. Tzanos, DSR Staff (Summer 1972)
I.C. Rickard, DSR Staff (Summer 1971)
*A.T. Supple, Jr., Engineering Assistant
†S.T. Brewer, Ph.D. Student
*G.J. Brown, Research Assistant, S.M., Ph.D. Student
P. Delaquil, Research Assistant (to Jan. 1972)
*†G.A. Ducat, Ph.D. Student (since May 1972)
*†M.V. Gregory, Ph.D. Student (since Oct. 1972)

---

* Continuing on staff after Summer 1972.

†Salary not paid from contract funds during FY 1972.

S.Y. Ho, Research Assistant, S.M. Student (since Feb. 1972)

†M.S. Kalra, Special Project Student (Spring 1972)

C.S. Kang, Research Assistant, Ph.D. Student (to Nov. 1971)

†L.T. Kim, Special Project Student (Spring 1972)

T.C. Leung, Research Assistant, Ph.D. Student (to Feb. 1972)

N.R. Ortiz, Research Assistant, Ph.D. Student (to April 1972)

†A.M. Thompson, B.S. Student (to June 1972)

J.L. Lazewatsky, Laboratory Assistant (part-time starting Feb. 1972)

K.D. Roberson, Laboratory Assistant (part-time, Feb.-May 1972)

1.4 References

(1) LMFBR Blanket Physics Project Progress Report No. 2, COO-3060-5, MITNE-131, June 30, 1971.

---

†Salary not paid from contract funds during FY 1972.

2. INSTRUMENTAL NEUTRON SPECTROSCOPY ON BLANKET MOCK-UP NO. 2

The work summarized in the present chapter is primarily concerned with the use of Li^6, He^3 and p-recoil spectrometers for the measurement of neutron spectra in Blanket Mock-Up No. 2. The complete results are presented in the topical report:

> N.R. Ortiz, I.C. Rickard, M.J. Driscoll and N.C. Rasmussen, "Instrumental Methods for Neutron Spectroscopy in the MIT Blanket Test Facility," COO-3060-3, MITNE-129, May, 1972.

2.1 Background

The United States Atomic Energy Commission has given high priority to the development of the liquid metal cooled fast breeder reactor (LMFBR) because of the general consensus that this system is best suited to insure a reliable and economical source of electrical power for the foreseeable future. The economic attractiveness of the LMFBR stems from its ability to breed more fissible fuel than it consumes. Since the blanket region of the LMFBR core accounts for a large fraction of the breeding, M.I.T. has undertaken, under A.E.C. contract, a detailed program of blanket physics analysis, of which the present research is a part.

The central objective of reactor physics analysis is an accurate description of neutron interaction rates, which can be represented as the product of a target material property – the cross section – and a projectile flux, the neutron flux. Both of these properties are energy-dependent. It is the second of these two factors, the energy spectrum of the neutron flux, which is the subject of the present research. More specifically, the objective of the work reported here has been the application and evaluation of instrumental methods for neutron spectroscopy for the determination of an accurate ambient spectrum in Blanket Test Facility Mock-Up No. 2, a simulation of the blanket

region of a large LMFBR designed for central station power generation.

The energy range of interest is from a few keV to several MeV. Over this energy range, instrumental methods can compete favorably with noninstrumental methods such as nuclear emulsions and foil activation.

2.2 Instruments and Techniques Used in this Work

The instrumental methods used in this work involved use of Li^6 and He^3 semiconductor detectors and proton-recoil proportional counters.

The Li^6 semiconductor detector was used in three different modes of operation, denoted as the Sum, Difference and Triton Methods. The last two methods were used in an attempt to improve the useful energy range and the resolution of the spectrometer.

The He^3 detector was operated in the Sum and Difference Modes. The latter mode improves the resolution, useful energy range and gamma discrimination of the detector.

The proton-recoil proportional counter selected was similar to that developed by Bennett (1,2) and extensively applied to fast critical experiments at ANL.

2.3 Description of the Blanket Test Facility and Test Assembly

A detailed description of the experimental facility is given in references (3) and (4). Only a brief description will be presented here. The Blanket Test Facility (BTF) is at the rear of the graphite-lined cavity comprising the MITR hohlraum; Fig. 2.1 shows a section view of the facility. The key component in the BTF is a converter lattice made up of graphite and slightly enriched uranium oxide fuel rods, which converts the incident hohlraum thermal spectrum into a spectrum of fast neutrons typical of that leaking from a large LMFBR core. The total power of the converter lattice is about 50 watts and the fast neutron flux approximately 10^9 n/cm^2-sec.

Blanket Assembly No. 2 is a mock-up of a representative large LMFBR blanket. It consists of three rows of subassemblies containing

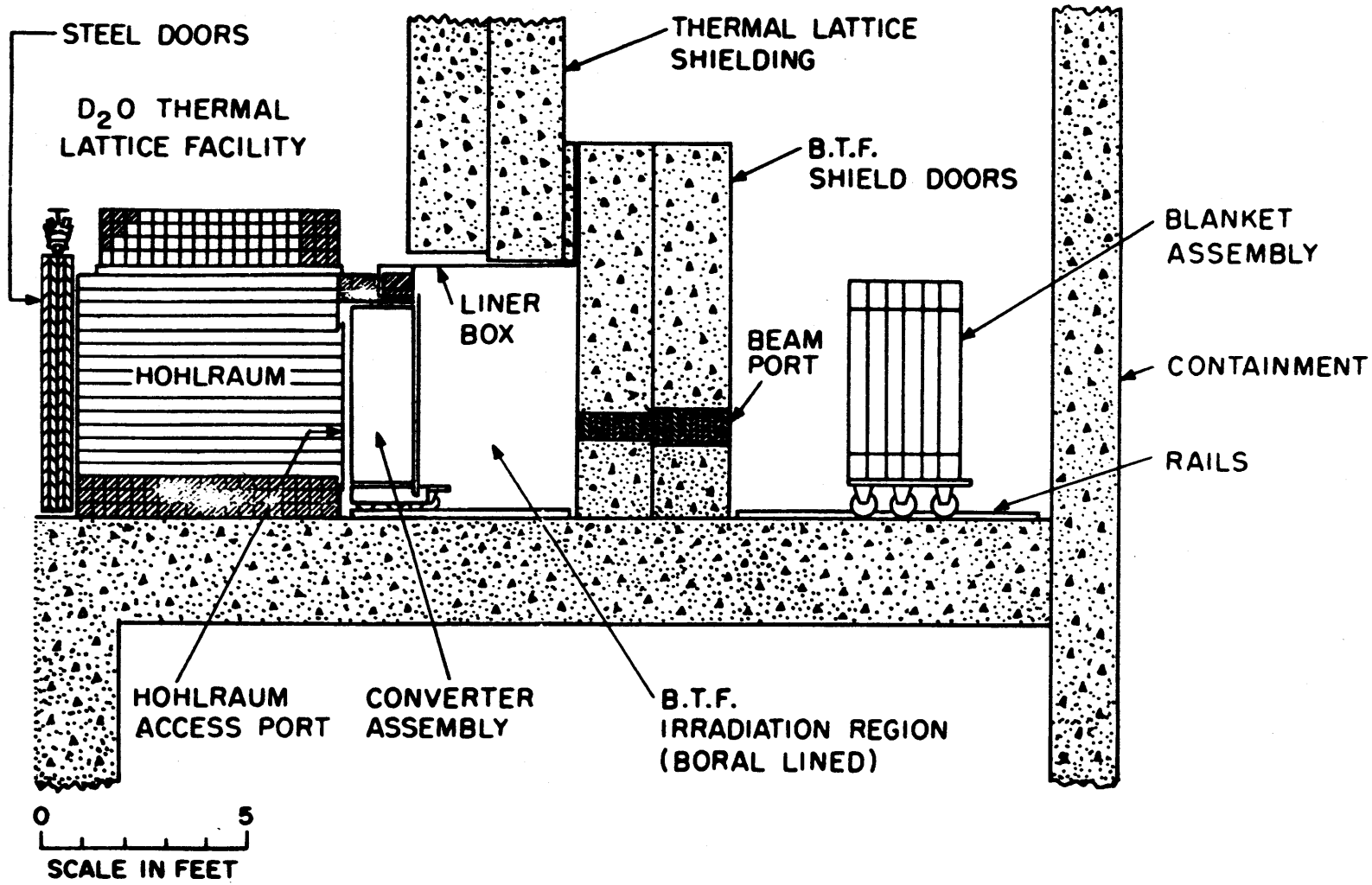

FIG. 2.1 SCHEMATIC CROSS SECTION VIEW OF HOHLRAUM AND BLANKET TEST FACILITY

steel-clad uranium metal fuel rods and anhydrous sodium chromate powder (Fig. 2.2). The relative proportions of the various constituents have been chosen to correctly simulate the UO_2 fuel, stainless steel clad and sodium coolant of a real LMFBR blanket (see Table 2.1). The blanket has an 18-inch-thick reflector of mild steel plate.

The blanket subassembly boxes are 5.92 inches square, 60 inches high, and have an approximate wall thickness of 3/32 inch. Each subassembly contains 121 fuel rods arranged in an 11 × 11 square lattice with a spacing of 0.511 inch. The fuel rods have a mean U^{235} enrichment of 1.08%.

Figure 2.3 shows the position of the test subassembly employed to hold the instruments used to measure the neutron flux. The subassembly is within the 30-inch center region which has been shown to have reached spectral equilibrium (4). The test subassembly is similar to the subassemblies described above except that a 1.75 × 1.75-inch center section has been removed and replaced by a hollow steel channel (see Fig. 2.4). Figure 2.5 shows the inner subassembly insert which fits into the center of the test subassembly. The insert consists of two sections: a bottom section and a top section. The bottom section is a 1.5 × 1.5 × 21 inch-long square box, with nine uranium metal fuel elements, carbon steel clad and 5/16-inch O.D. The top section is similar to the one described above, but two fuel elements in opposite corners have been removed to leave space for instrument cables. The detector (e.g., Li^6, He^3, proton-recoil) is placed between the two sections of the inner subassembly insert, in a cavity 1.5 × 1.5 inches in cross section and 8 inches long. With the exception of the thin steel channel walls, the special subassembly has been designed to have a composition similar to the other standard subassemblies to avoid creation of large flux perturbations. The same experimental setup was used with the Li^6 and He^3 semiconductor detectors and the proton-recoil detector. Figure 2.6 shows a schematic of the upper section of the inner subassembly with the proton-recoil detector installed.

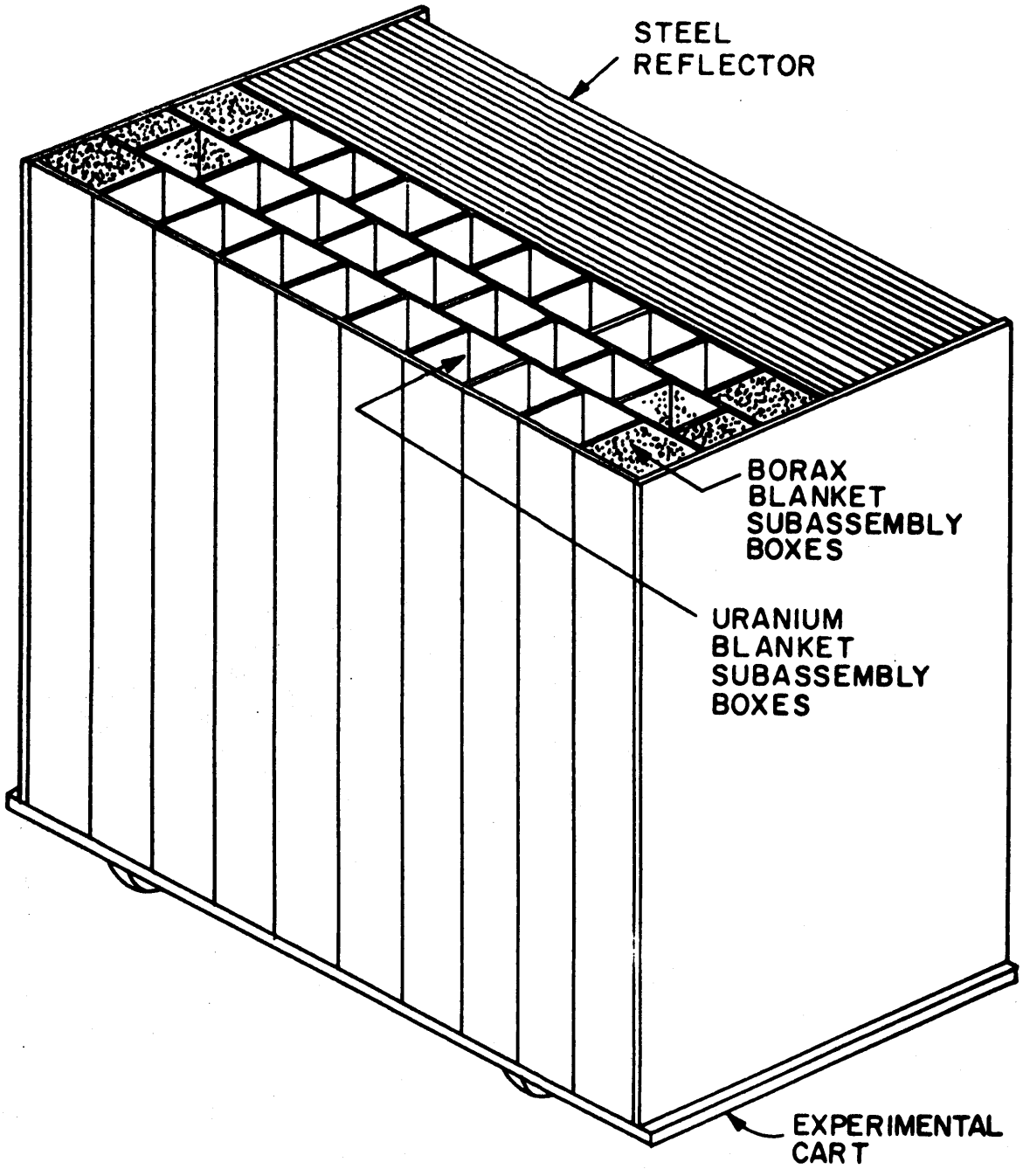

FIG. 2.2 SCHEMATIC VIEW OF BLANKET ASSEMBLY NO. 2

TABLE 2.1

Homogenized Atom Densities in BTF Blanket No. 2

Nuclide	Blanket No. 2		Equivalent Realistic Blanket*	
U^{235}	0.000088		0.000016	
U^{238}	0.008108		0.008131	
O	0.016293		0.016293	
Na	0.008128		0.008128	
Cr	0.004064	0.017814	0.003728	0.017814
Fe	0.013750		0.012611	
Ni	0.000000		0.001475	
H	0.000073		0.000000	
C	0.000096		0.000082	

* Composed of 37.0 v/o depleted UO_2 (at 90% of theoretical density), 20.7 v/o Type 316 stainless steel, 32 v/o sodium and 10.3 v/o void.

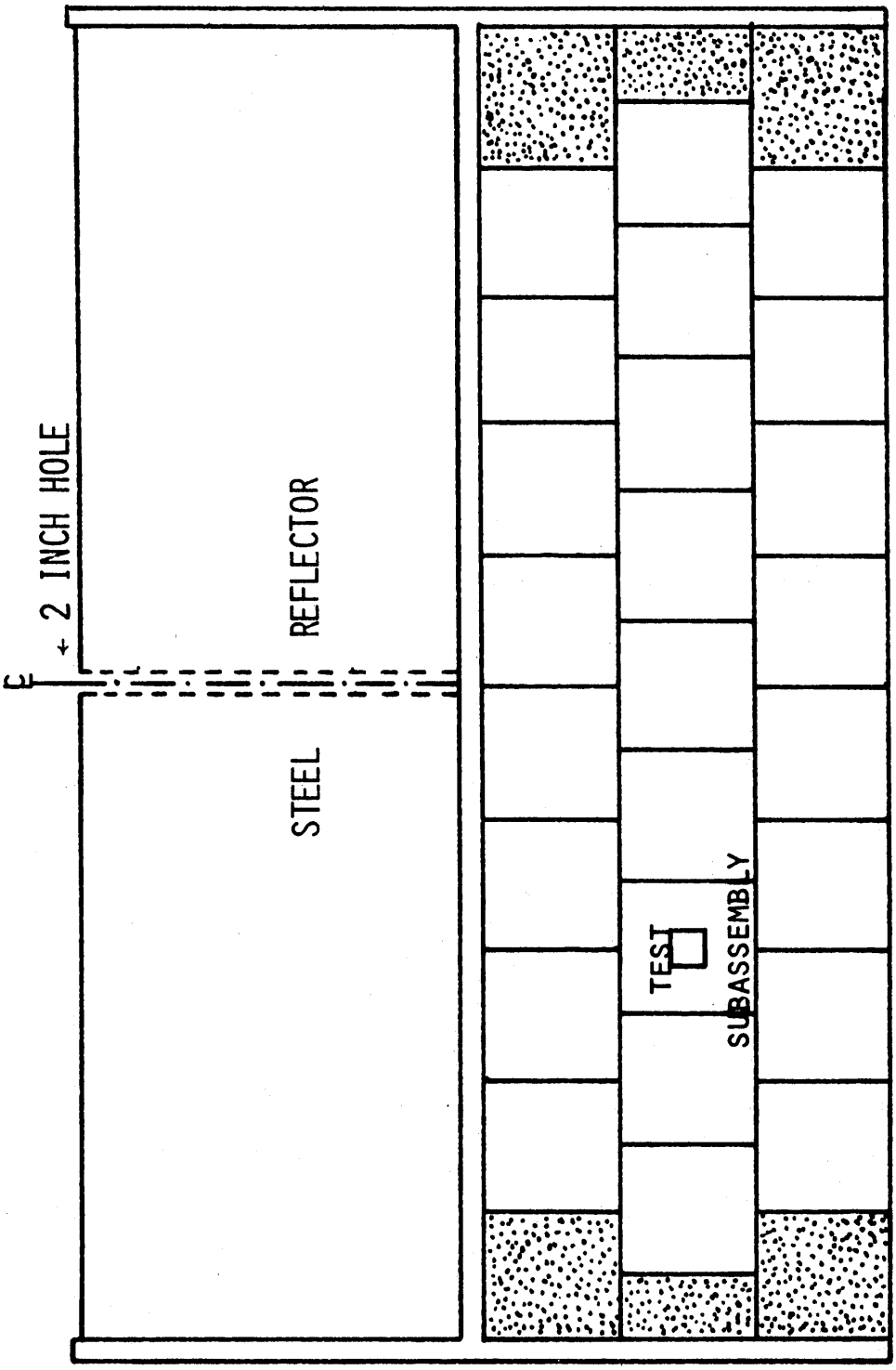

FIG. 2.3 PLAN VIEW OF BLANKET ASSEMBLY SHOWING THE TEST SUBASSEMBLY POSITION

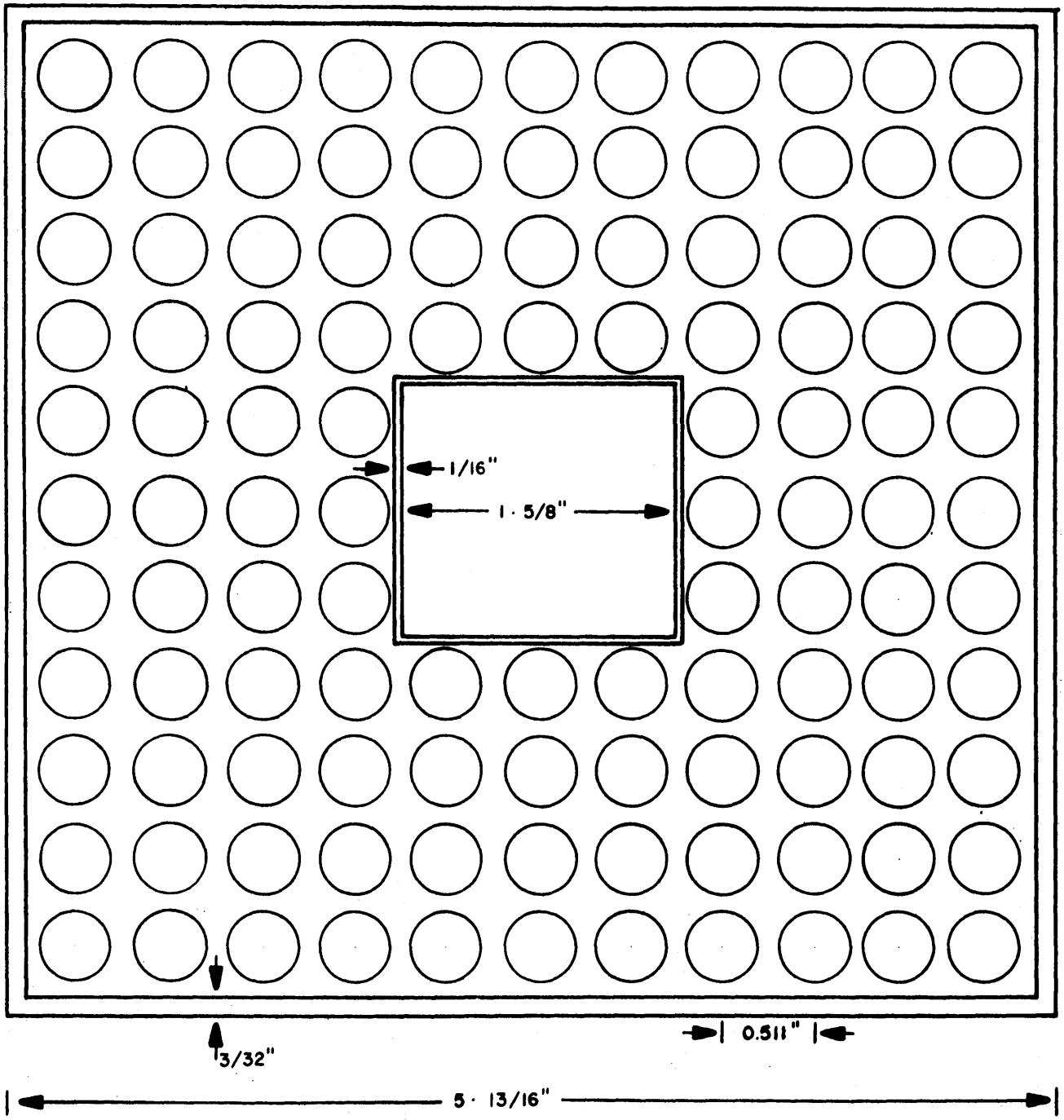

CROSS SECTION THROUGH
B T F TEST SUBASSEMBLY

Fig. 2.4

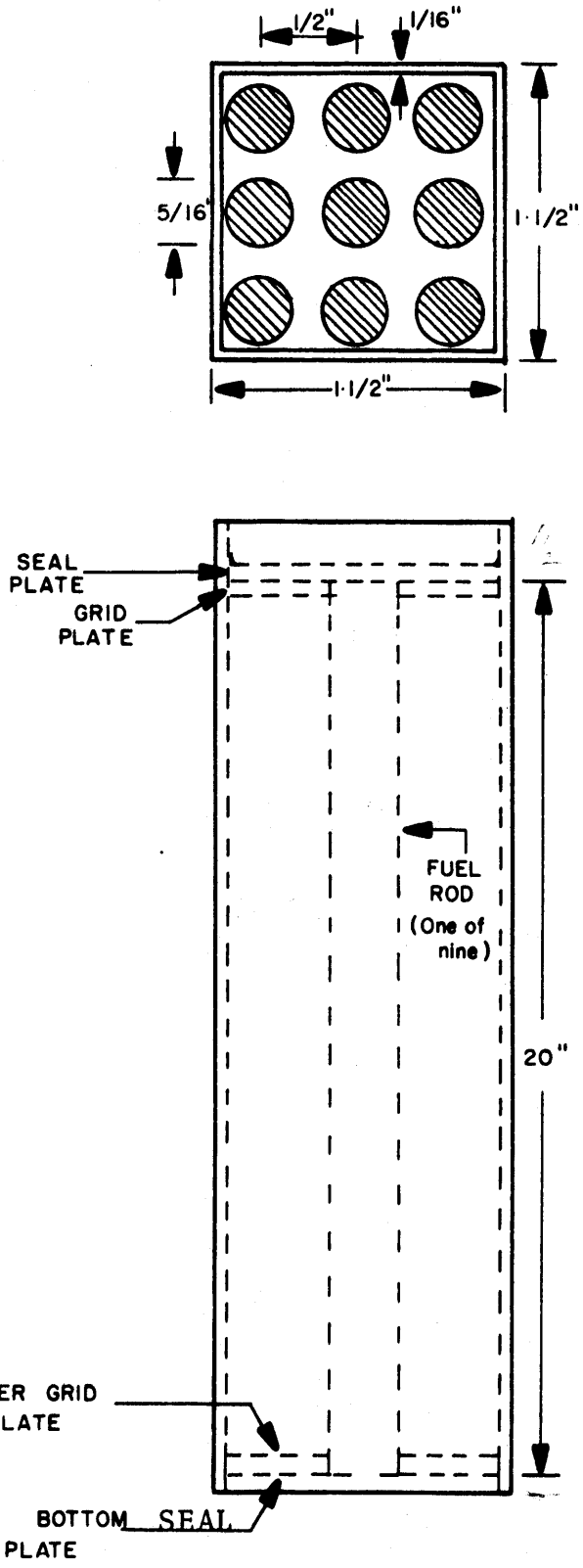

FIG. 2.5 Bottom Inner Subassembly Insert

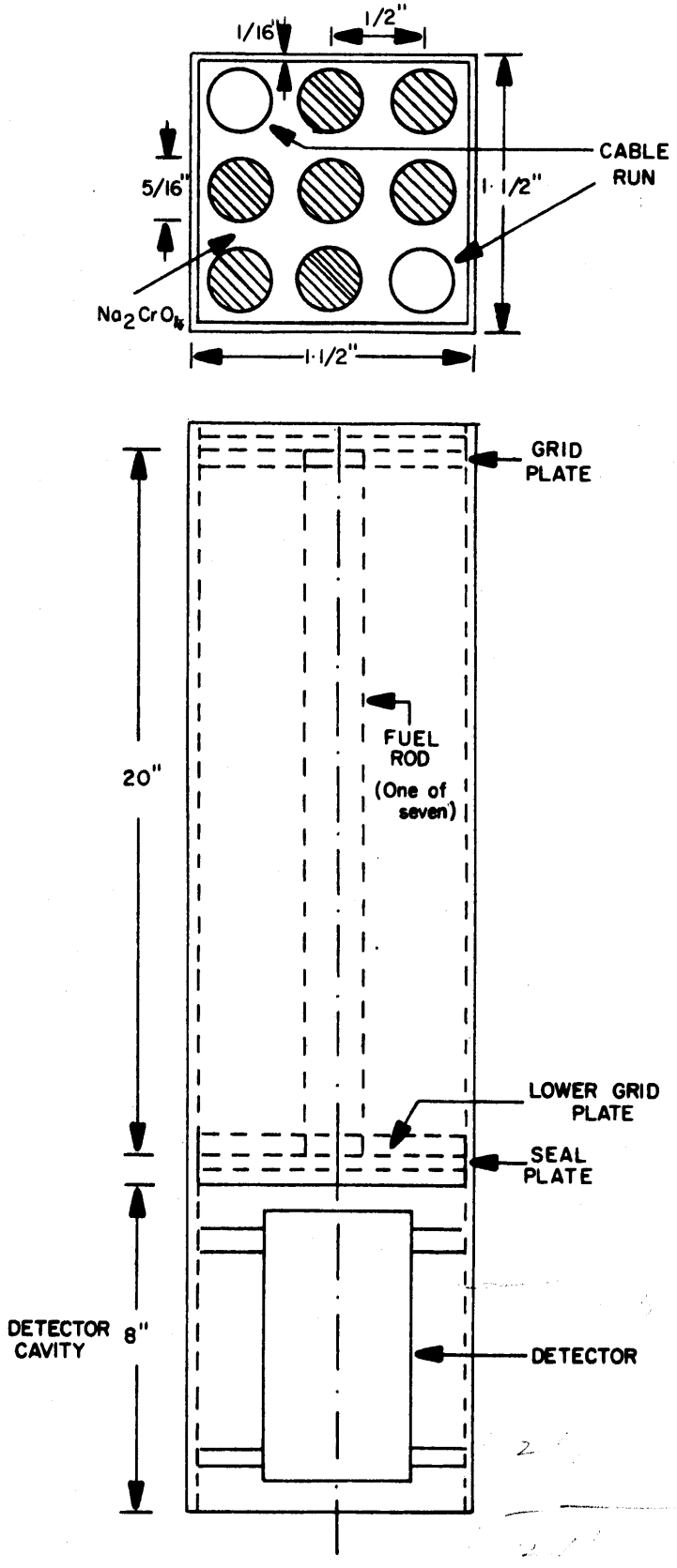

FIG. 2.6 Top Inner Subassembly Showing Detector Installed In Cavity

2.4 Helium-3 Semiconductor Detector

2.4.1 Introduction

This system consists of two silicon semiconductor detectors in a sandwich configuration; the space between the two detectors is filled with He^3 gas. Detection is based on the reaction:

$$ {}_0n^1 + {}_2He^3 \rightarrow {}_1H^1 + {}_1H^3 + Q \qquad (2.1) $$

In this reaction the neutron and the nucleus interact to form two product particles. Energy is released; this energy plus the energy of the incident neutron appears as kinetic energy of the product particles.

$$ E_n + Q = E_p + E_T \qquad (2.2) $$

2.4.2 Sum Method

2.4.2.1 Description of the Method

In the Sum Method, the output of both detectors is added and only those which fulfill the coincidence requirements are accumulated in the multichannel pulse-height analyzer. Figure 2.7 shows the block diagram of the neutron spectrometer electronic system. According to Eq. 2.2, the height of the sum pulse is proportional to the energy of the neutron plus the Q value (764 keV) of the reaction. The neutron energy is therefore obtained with no ambiguity from a measurement of the total energy released.

2.4.2.2 Effect of the Discriminator Settings

To discriminate against the noise inherent in the electronic system and to reduce the number of small gamma-ray induced pulses reaching the coincidence unit, a baseline setting equivalent to 150 keV was selected for the timing single-channel analyzer. The application of this energy discrimination will cause the rejection of some real events in which one of the emitted particles does not carry away enough kinetic energy. This effect is taken into account in the unfolding of the measured spectrum.

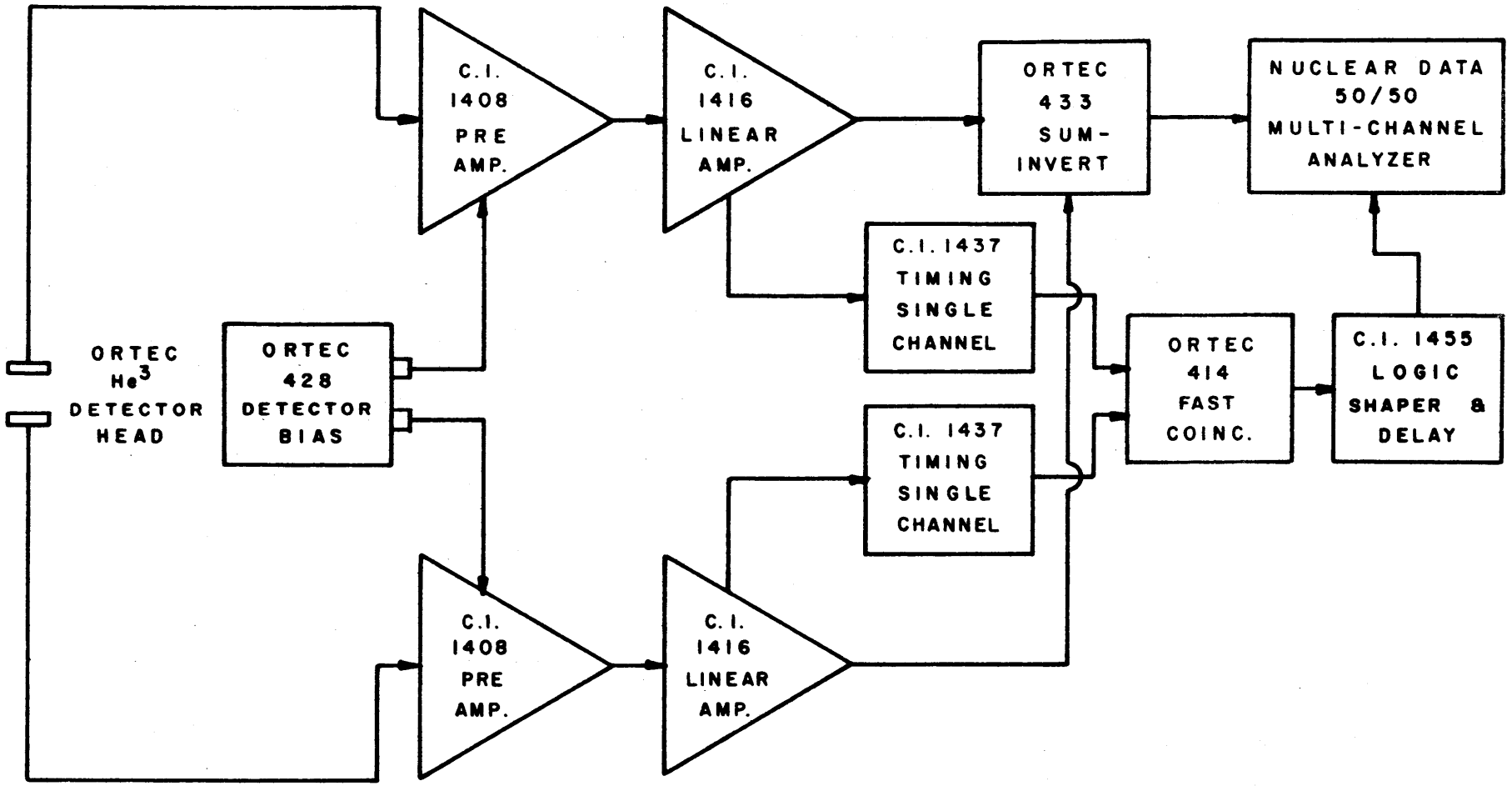

FIG. 2.7 Electronic System For He-3 Neutron Spectrometer

2.4.2.3 Experimental Results

The He^3 detector was placed in the test subassembly located in the second row of Blanket Mock-Up No. 2 to measure the ambient fast neutron flux. The steel doors controlling the thermal neutron flux incident on the converter cart were opened only two and a half (of a normal 30) turns, to limit the converter power and thereby avoid the pile-up of events at the output of the detector preamplifier. The same experimental conditions were used in all the experiments performed with the He^3 detector, Li^6 detector and proton-recoil proportional counter. The unfolded neutron spectrum, plotted per unit lethargy in Fig. 2.8 ($\phi(u) = E\phi(E)$), shows a broad peak around 350 keV. Only the region above a neutron energy of about 200 keV was measured with the Sum Method just described, since the large value of the absorption cross section for low-energy neutrons produces a large background peak which affects the measurements.

The estimated errors in the neutron flux range from about 9% to 13% in the energy region from 200 keV to 1.3 MeV.

2.4.3 Difference Method

The Difference Method is used in an attempt to improve the low-energy resolution of the system and to improve the rejection of gamma and noise background. This technique was first used with Li^6 semiconductor detectors (5). In this technique, the signals of both detectors are fed into a C.I.-1417 Amplifier operating in the difference mode; the amplified output is then fed in coincidence with the output of the logic shaper and delay to the multichannel analyzer. The rest of the electronic system is similar to the Sum Method electronics (see Fig. 2.9).

This method has the advantage that any equal-amplitude noise common to both detectors is cancelled in the subtraction process. Similarly, those gamma events which cause the same or nearly the same ionization in both detectors are rejected, improving the gamma discrimination.

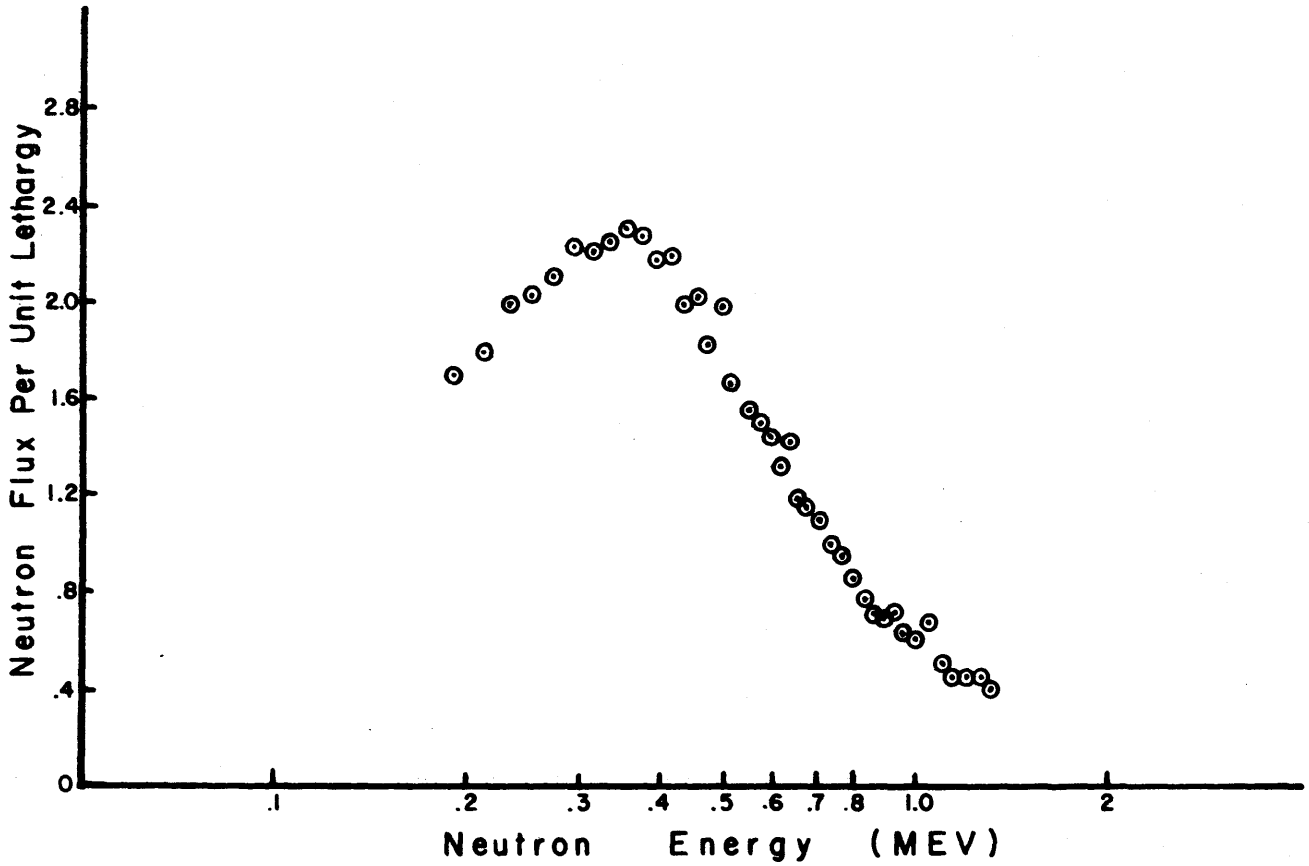

FIG. 2.8 Neutron Spectrum In Blanket Mockup NO.2 Using The He-3 System Sym Method

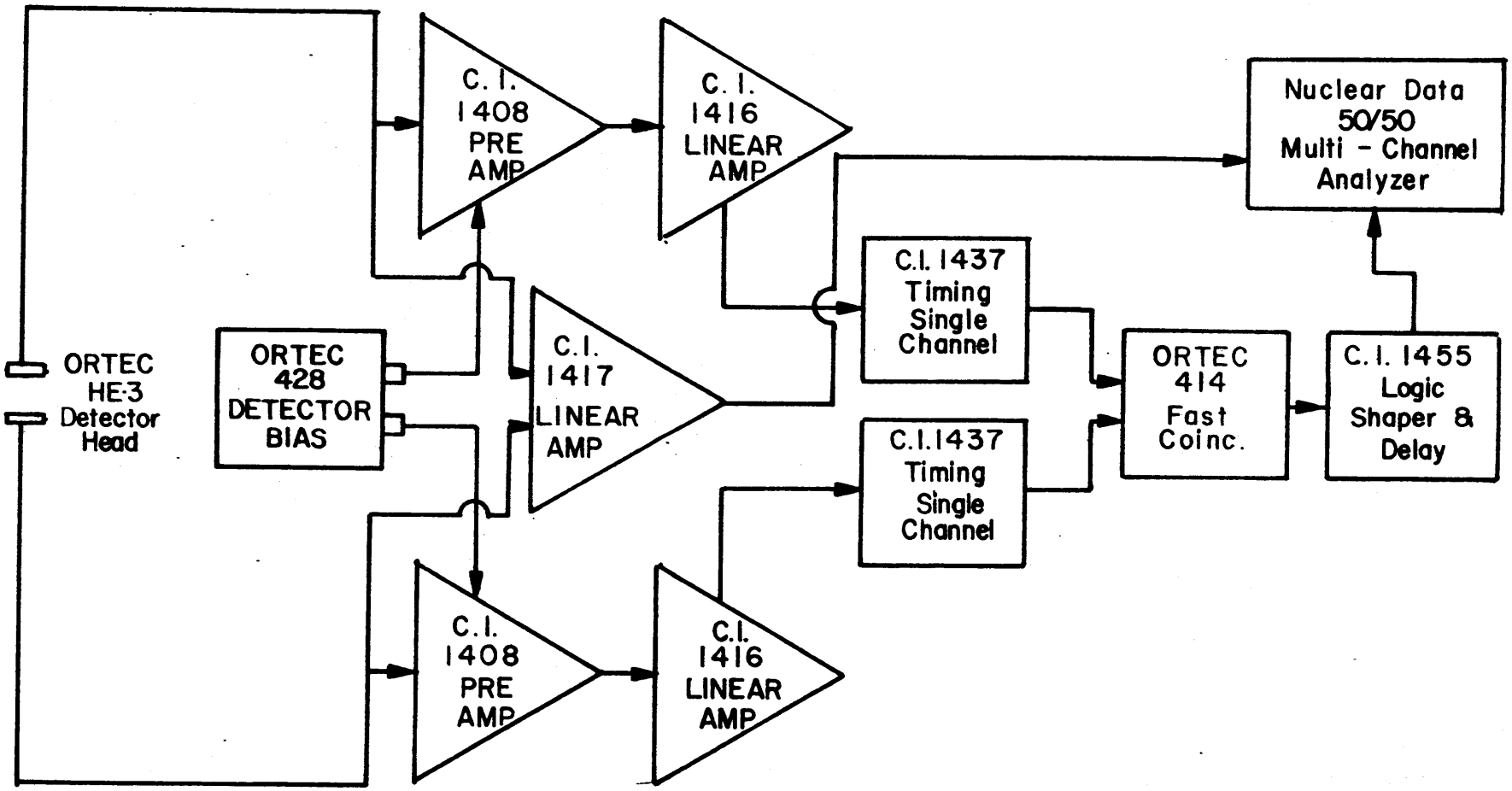

FIG. 2.9 He-3 Neutron Spectrometer, Difference Method Electronic System

The equations for the kinematics of the reaction show that the difference between the product particle energies changes much more rapidly at neutron energies in the low-keV region than does the sum of the product energies. Replacement of the sum amplifier by a difference amplifier should therefore improve the energy resolution (Table 2.2).

2.4.3.1 Unfolding Using the Derivative Technique

The equation relating the measured difference spectrum to the incident neutron flux is

$$M(\Delta) = N \int_0^\infty \varepsilon(E) P(E,\Delta) \sigma(E) \phi(E)\, dE \qquad (2.3)$$

where

$M(\Delta)$ = measured charged particle spectrum at a difference energy Δ.

$\varepsilon(E)$ = detector efficiency, including discriminator and electronic effects.

$P(E,\Delta)$ = probability that a reaction which takes place at a neutron energy E contributes to the counting rate at Δ.

$\sigma(E)$ = absorption cross section at energy E.

$\phi(E)$ = incident neutron flux.

It can be shown that for an isotropic reaction in the center of mass system

$$P(E,\Delta) = \frac{2/3}{\sqrt{E_1(E_1+0.75Q)}}$$

where

E_1 = neutron energy.

Two ways of solving Eq. 2.3 will be considered: the derivative technique and the integral technique. The first method is discussed

TABLE 2.2

He^3 System – Comparison of Difference Method and Sum Method

E_1 (keV)	E_3 (keV)	E_4 (keV)	Δ^* max $E_3 - E_4$ (keV)	$E_3 + E_4$ (keV)
0	573.	191.	382.	764.
0.5	582.	182.5	399.5	764.5
1.0	586.	179.	407.	765.
2.0	591.	175.	416.	766.
3.0	595.	172.	423.	767.
10.0	617.	157.	460.	774.
25.0	649.	140.	509.	789.
50.0	691.	123.	568.	814.
100.0	761.	103.	658.	864.
200.0	883.	81.	802.	964.
500.0	1212.	52.	1160.	1264.
750.0	1474.	40.	1434.	1514.
1000.0	1731.	33.	1698.	1764.
1500.0	2239.	25.	2214.	2264.

* For observation of products at $\theta = 0°$, $\phi = 180°$.

in this section; the latter is explained in the next section.

To take into account the effect of the electronics, which cannot distinguish between $(E_T - E_\alpha)$ and $(E_\alpha - E_T)$, Eq. 2.3 is written as:

$$M(\Delta) = \int_{E'=E}^{E'=E_L} \varepsilon(E')\, P(E',\Delta)\, \Sigma(E')\, \phi(E')\, dE'$$

$$+ \int_{E'=E_L}^{E_{max}} \varepsilon(E')\, P_o(E',\Delta)\, \Sigma(E')\, \phi(E')\, dE' \qquad (2.4)$$

where

E_L = neutron energy at which the effect of the electronics will affect (actually double) the value of the probability function.

E_{max} = maximum neutron energy.

Applying Leibnitz's rule to Eq. 2.4, one can show that

$$\phi(E) = \frac{-dM(\Delta)}{dE} \frac{1}{\varepsilon(E)\, P(E,\Delta)\, \Sigma(E)} + \frac{P(E_L,\Delta)\Sigma(E_L)\phi(E_L)}{\varepsilon(E)P(E,\Delta)\Sigma(E)} \frac{dE_L}{dE} \qquad (2.5)$$

At high neutron energies, the second term vanishes and the expression becomes

$$\phi(E) = \frac{-dM(\Delta)}{dE} \frac{1}{P(E,\Delta)\Sigma(E)\, \varepsilon(E)} \qquad (2.6)$$

The neutron flux is calculated first at high neutron energies ($E > 1$ MeV) using Eq. 2.6. In other words, the measured data are unfolded starting with the highest channel. As the energy is decreased, the second term of Eq. 2.5 becomes important and Eq. 2.5 is used to continue the unfolding down to the lowest neutron energy. A computer program called DIFFE was written to perform the unfolding of the measured spectrum.

2.4.3.2 Unfolding Using the Integral Technique

The integral equation (2.3) can be replaced by the (approximate) matrix equation

$$M_i(\Delta) = \sum_{j=1}^{n} K_{ij} P_{ij} \phi_j \tag{2.7}$$

or

$$\overline{M} = \overline{A}\,\overline{\phi} \tag{2.8}$$

where

K_{ij} is a square n × n matrix

$$A_{ij} = \sum_{j} K_{ij} P_{ij} \tag{2.9}$$

$\overline{A}$ is known as the detector response matrix. The first task is to determine the elements of the matrix $\overline{A}$ for a particular problem. In this case, they are calculated from the kinematics equations of the reaction. The second portion of the analysis is common to all problems of this type, i.e., the solution of Eq. 2.8 for $\overline{\phi}$, the neutron flux. The equation cannot be solved by simply inverting matrix $\overline{A}$ because of the instability of the solutions obtained (for example, negative fluxes with large oscillations). The unfolding technique devised by R. Gold is used; this is discussed in detail in reference (6). A computer program MATRIX was written to solve the problem.

2.4.3.3 Experimental Results

The He^3 semiconductor detector operating in the Sum and Difference Modes was used to measure the neutron spectrum in Blanket Mock-Up No. 2. The Sum Method covers an energy range from 200 keV to 1.3 MeV. The Difference Method extends the low energy limit and covers an energy range from 10 keV to 1.1 MeV. The overlap region for both methods (200 keV to 1.1 MeV) shows good agreement between the two neutron flux measurements (Fig. 2.10). The Difference Method improves the gamma and noise discrimination.

The integral technique and differential technique used to unfold the difference spectrum are in good agreement over the entire energy range of the measurements (Fig. 2.11). This consistency gives confidence in the procedures applied to each technique.

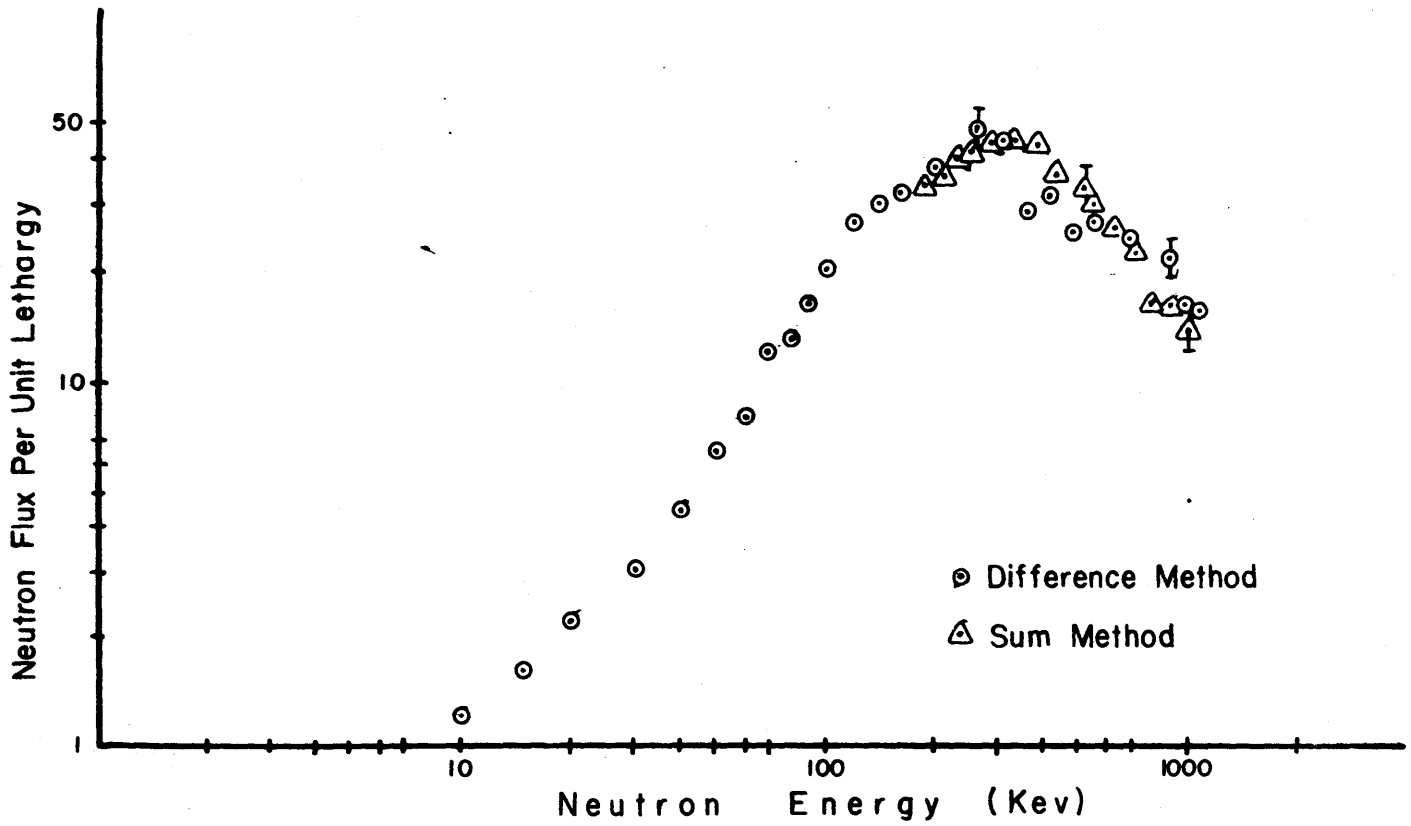

FIG. 2.10 Neutron Flux Measurement In The Blanket Mockup NO. 2 - He-3 System

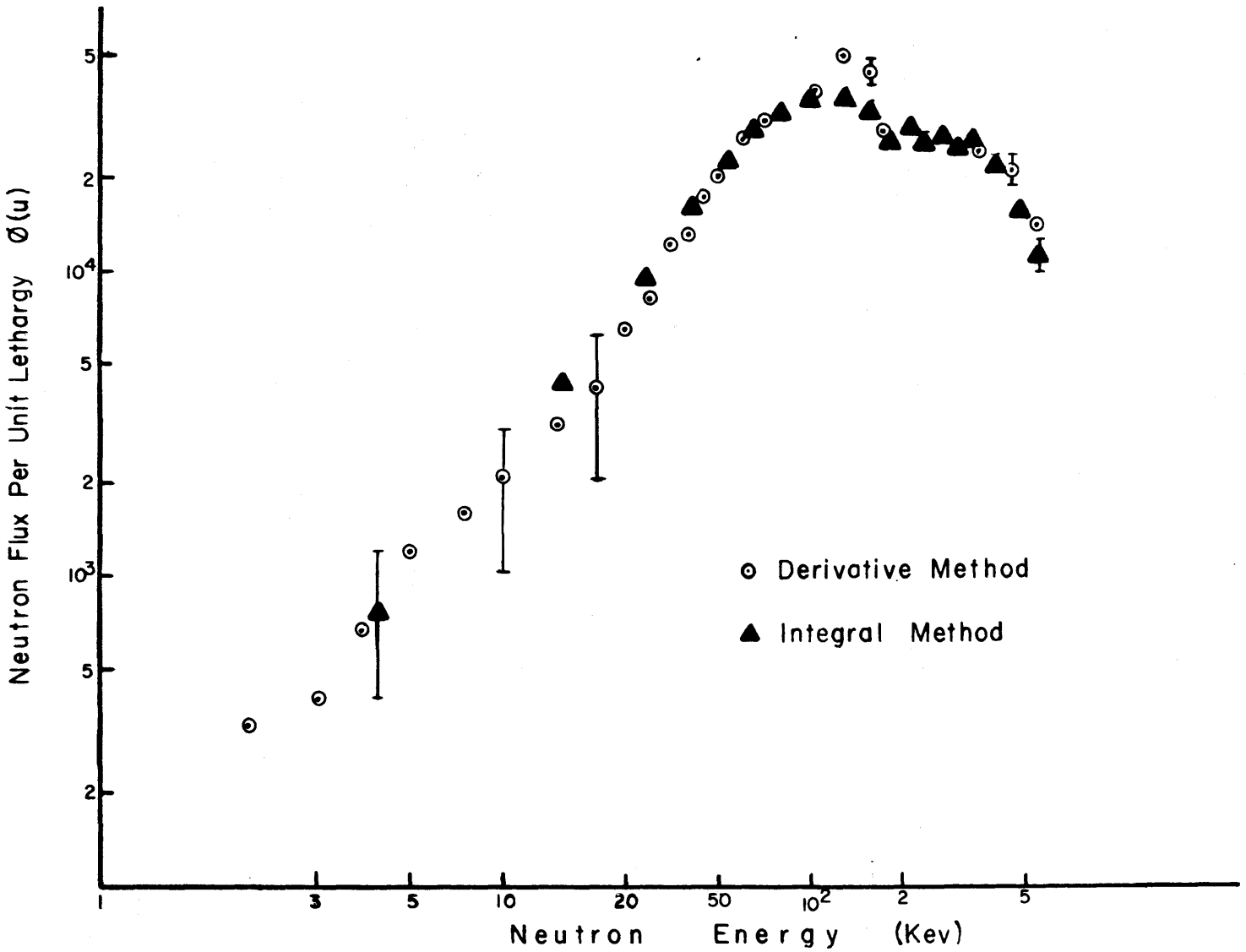

FIG. 2.11 Neutron Spectrum In The Blanket Mockup NO. 2 - He-3 System Difference Method

The uncertainty introduced by the discriminator settings affects the accuracy of the measurements in the low-energy region and reduces the sensitivity of the detector to low-energy neutrons.

2.5 Lithium-6 Semiconductor Detector

2.5.1 Introduction

The Li^6 semiconductor detector consists of a sandwich configuration of two closely spaced surface barrier detectors with a thin layer of Li^6F located between the detectors (7). The detector is based on the reaction

$$ {}_0N^1 + {}_3Li^6 \rightarrow {}_1H^3 + {}_2He^4 + Q \qquad (2.10) $$

If the triton and the alpha particles are absorbed by the semiconductor detectors, each produces a pulse whose height is proportional to the energy deposited by the particle.

In this section, three different modes of operation of the detector are described to cover the energy range from 10 keV to 3 MeV: The Sum Method from 500 keV to 3 MeV, the Triton Method from 10 keV to 600 keV, and the Difference Method from 10 keV to 600 keV.

A Cf^{252} neutron source was used as a standard to calculate the response function of the detector. The correction obtained with this source allows one to extend the low-energy limit of the Sum Method down to 160 keV.

Finally, it should be noted that the high Q value (4.78 MeV) of the Li^6 (n,α) T-reaction improves the gamma discrimination of the system in comparison with the He^3 system.

2.5.2 Sum Method

The alpha and triton particles are detected in the two semiconductor detectors, and the total energy shared by these particles is indicated by summing in coincidence the output pulses from the two detectors. The amplitude of the Sum pulse thus has a one-to-one correspondence with the energy of the incident neutron. The neutron

energy is equal to the total energy minus the Q value of the reaction.

The electronics associated with this system are similar to the electronics used with the He^3 system. Only the settings of the linear amplifiers and the timing single-channel analyzer are different.

2.5.2.1 Measurements of the Cf^{252} Spontaneous-Fission Neutron Spectrum

In order to provide a basis for direct normalization of data on unknown spectra to a known reference, the Cf^{252} neutron spectrum was measured using the Li^6 detector operating in the Sum Mode. The theoretical spectrum (8) and the unfolded spectrum are shown in Fig. 2.12. The charged particle spectrum was unfolded using the computer program SUMMA. It can be seen that the agreement is good over most of the energy range observed. The larger discrepancies occur in the lowest energy region, due to the strong variation of the $Li^6(n,\alpha)$ T-cross section (9) around the broad resonance at 250 keV. The ratio of the theoretical spectrum to the measured spectrum is used to correct the systematic anomaly shown by the detector in the energy region from 10 keV to 400 keV. This correction was applied to the neutron flux measurements in Blanket Mock-Up No. 2, as discussed in the next section.

2.5.2.2 Neutron Flux in Blanket Mock-Up No. 2

The Li^6 semiconductor detector was placed in the test subassembly, described in section 2.3, to measure the fast neutron flux. The experimental data were unfolded with the SUMMA program. The computer program output was corrected by hand, using the response function of the detector (sec. 2.5.2.1). The unfolded neutron spectrum covers an energy range from 160 keV to 3.1 MeV; it shows a small variation from 160 keV to 350 keV and falls rapidly as the neutron energy increases (Fig. 2.13). Around 1 MeV, a small dip is observed, caused by a scattering resonance in oxygen. Two small peaks at 1.5 MeV and 2.3 MeV are shown. These have also been observed in several fast neutron spectrum measurements (10, 11, 12). They are

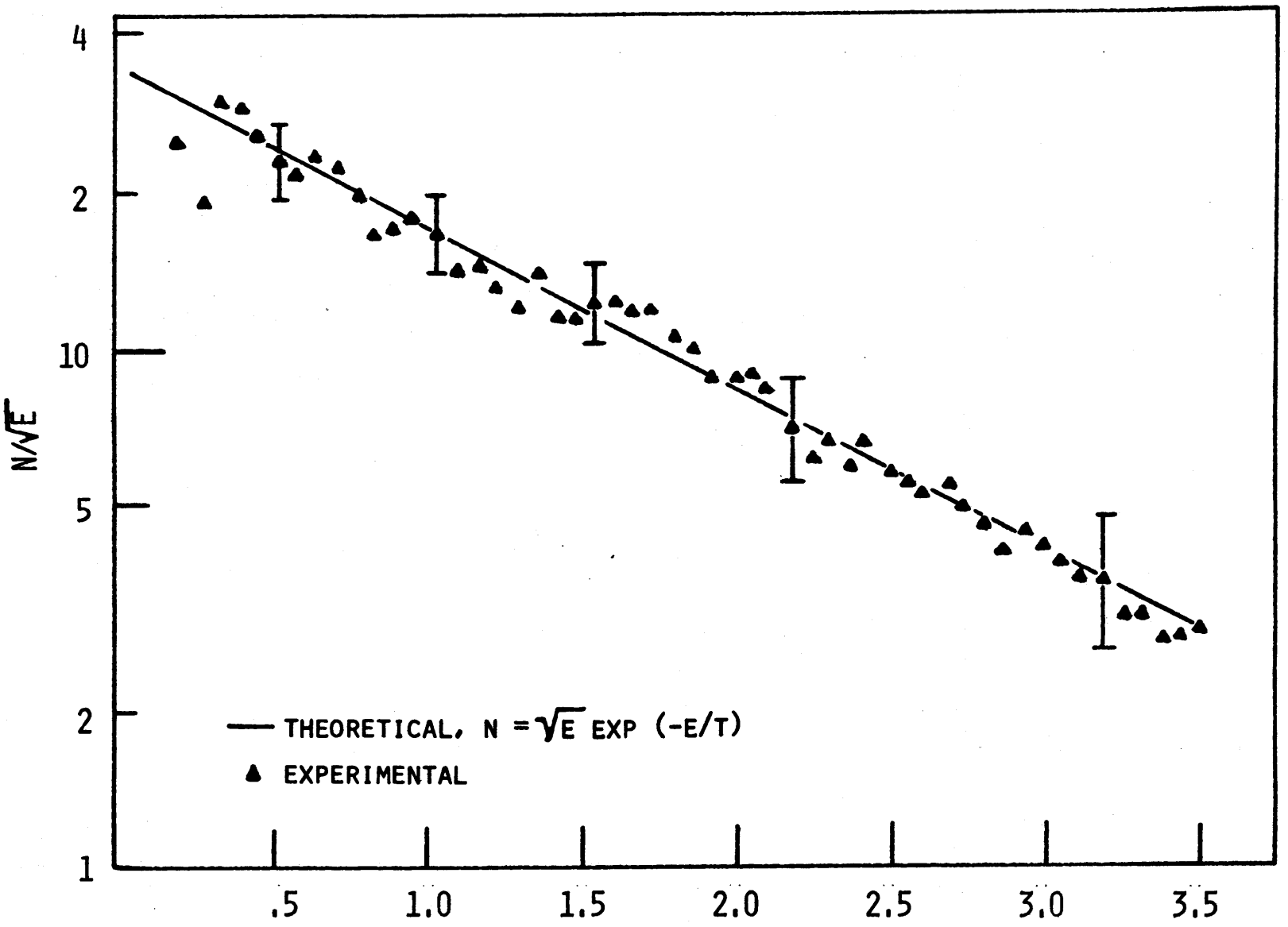

FIG.2.12 CF-252 SPONTANEOUS NEUTRON SPECTRUM

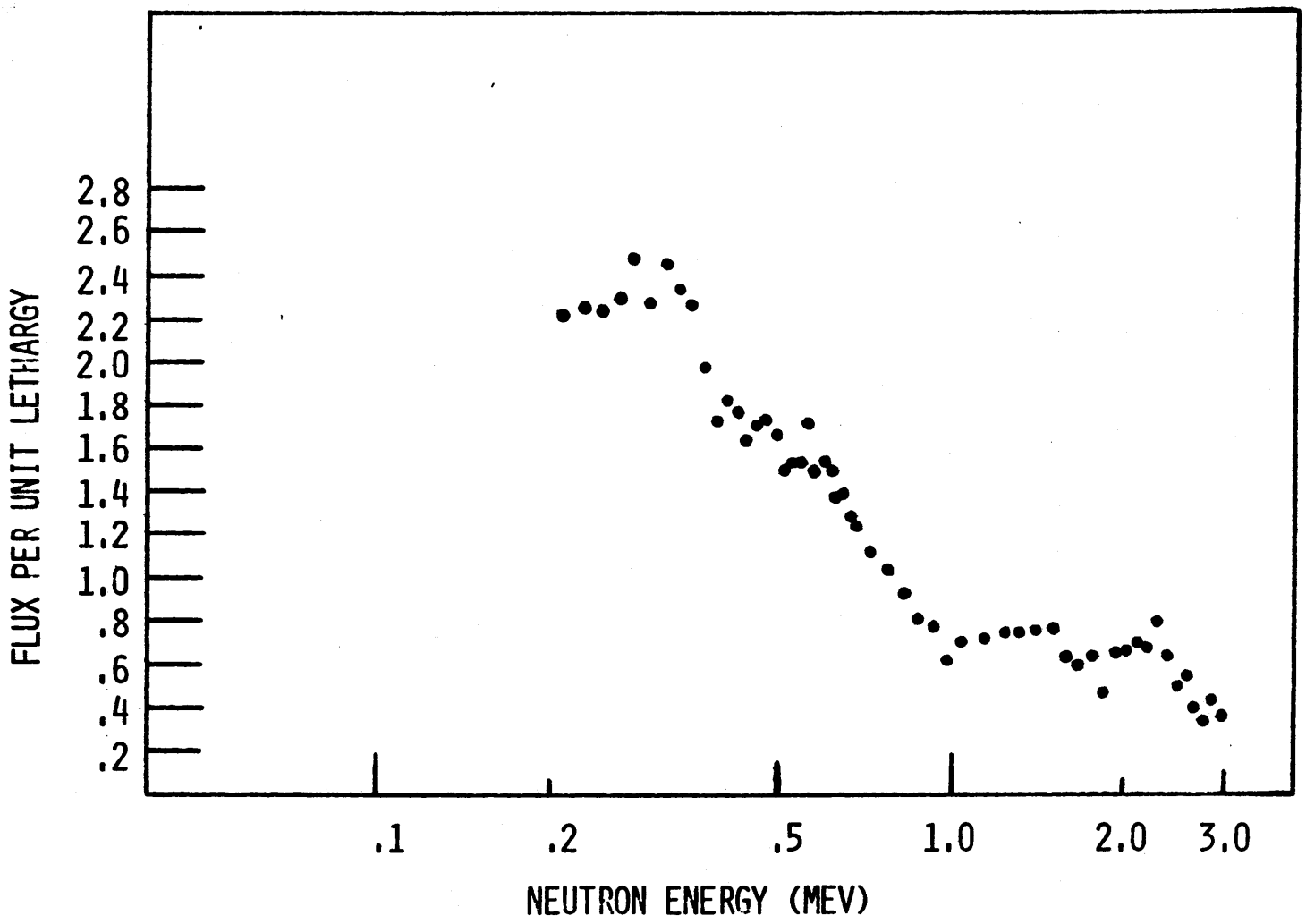

FIG. 2.13 NEUTRON SPECTRUM IN BLANKET NO.2, Li-6 SYSTEM, SUM METHOD

a consequence of pronounced minima in the sodium and oxygen cross sections in these energy regions. Measurements done in Blanket Mock-Up No. 2, using a neutron spectrometer based on gamma spectroscopy (13), also show peaks near 1.5 MeV and 2.3 MeV.

2.5.3 Difference Method

The Difference Method is mainly used to improve the resolution of the system at low neutron energies (see Table 2.3), since the gamma and noise rejection of the system is very good due to the high Q value of the reaction. The block diagram of the electronic system is the same as described in section 2.4.3 and shown in Fig. 2.9.

2.5.3.1 Construction of Response Function

The measured difference spectrum is related to the incident neutron flux by Eq. 2.3. The probability function is given by Eq. 2.11 because the $Li^6(n,\alpha)$ T-reaction is nonisotropic in the center of mass

$$P(E,\Delta)\, d\Delta = 2\pi d(\cos\Psi)\, \sigma_\Omega(E,\cos\Psi) \qquad (2.11)$$

where

$\sigma_\Omega(E,\cos\Psi)$ = differential cross section of the reaction for neutrons of energy E.

Following the discussion of reference (14), the differential cross section is represented by a second-order Legendre polynomial expansion.

2.5.3.2 Unfolding Using the Derivative Technique

The unfolding technique discussed in section 2.4.3.1 also applies to the Li^6 semiconductor detector. The only difference is that the differential absorption cross section is nonisotropic in the center of mass, and therefore a subroutine called THETA2 was included in the DIFFE program to take into account the nonisotropic effect.

TABLE 2.3

Li^6 System – Comparison of Difference Method and Sum Method

E_1 (keV)	E_3 (keV)	E_4 (keV)	Δ^* max $E_3 - E_4$ (keV)	SUM $E_3 + E_4$ (keV)
0	2730	2050	680	4780
0.5	2750	2030.5	719.5	4780.5
1.0	2758	2022	736	4781
2.0	2769	2013	756	4782
3.0	2778	2005	773	4783
10.0	2819	1971	848	4790
25.0	2875	1930	945	4805
50.0	2943	1887	1056	4830
100.0	3047	1833	1214	4880
200.0	3214	1766	1448	4980
500.0	3610	1670	1940	5280
750.0	3899	1631	2268	5530
1000.0	4170	1610	2560	5780
1500.0	4636	1594	3092	6280

* Corresponding to $\theta = 0°$, $\phi = 180°$.

Equations 2.5 and 2.6 are used to obtain the unfolded neutron spectrum from the measured difference spectrum.

2.5.3.3 Unfolding Using the Integral Technique

The unfolding technique of section 2.4.3.2 can also be applied to the Li^6 semiconductor detector. A subroutine in the computer program MATRIX calculates the neutron flux per unit lethargy at fifty different energies fixed by the program. It also calculates the response function based on the kinematics equation of the $Li^6(n,\alpha)$ T-reaction. Other subroutines contained in the program take into account the anisotropic nature of the reaction and the effect of the electronics.

2.5.3.4 Experimental Results

The neutron flux in Blanket No. 2 was measured using the Li^6 semiconductor detector operating in the difference mode. Figure 2.14 shows the flux per unit lethargy as a function of neutron energy from 10 keV to 600 keV. It was unfolded using the integral technique discussed in the previous section. For reasons explained below, the differential unfolding technique did not yield acceptable results.

By unfolding theoretical particle spectra (i.e., spectra having realistic shapes, but for which exact relations between charged particle and neutron spectra could be formulated), it was found that the computer program using the derivative technique for unfolding is very sensitive to errors associated with the differential cross section and to statistical errors in the measured particle spectra. This leads to spurious oscillations and anomalies in the unfolded neutron spectra. Hence, at the minimum, a subroutine to smooth the data before calculating derivatives should be added to improve the stability of the program before further application to the Li^6 detector is attempted. From the results reported in section 2.4.3.1, we may conclude that the smoother and more accurately known absorption cross section of He^3, and the isotropic nature of the reaction in the center of mass make use of the unimproved differential approach at least marginally acceptable for that system.

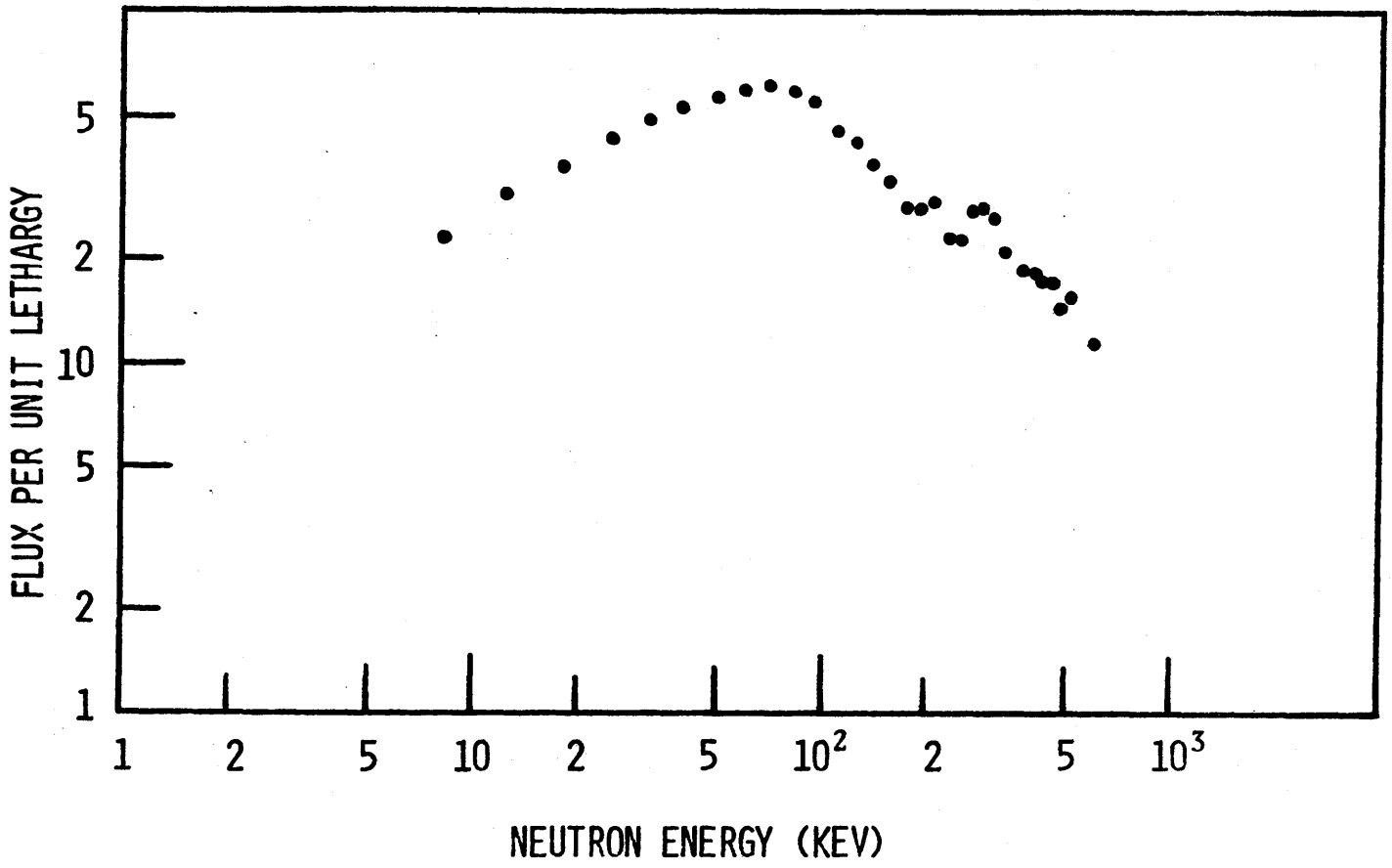

FIG. 2.14 FAST NEUTRON SPECTRUM IN BLANKET MOCKUP NO.2, Li-6 SYSTEM DIFFERENCE METHOD

2.5.4 Triton Technique

2.5.4.1 Description of the Technique

In this technique (9, 15), only one of the detector outputs is registered in the multichannel analyzer, but the outputs of both detectors are required to be in coincidence to register a count. The alpha and triton spectra obtained from the output of the detector are well separated, so that it is possible to analyze the data above the center of the triton peak without having to correct for the presence of the alpha spectrum.

2.5.4.2 Response Function Calculation

By analogy with Eq. 2.11, the response function for the Triton Method can be represented as

$$P(E, E_3)\, dE_3 = 2\pi d(\cos\Psi)\sigma_\Omega(E, \cos\Psi)$$

where

E_3 = kinetic energy of the triton particle.

The differential cross section, $\sigma_\Omega(E, \cos\Psi)$, is strongly nonisotropic in the center of mass and is approximated by a second-order Legendre polynomial expansion.

2.5.4.3 Neutron Flux Measurements

The Li^6 semiconductor detector, operating in the triton mode, was placed in Blanket Mock-Up No. 2 to measure the fast neutron spectrum. The matrix equation discussed in section 2.4.3.2 is used to unfold the measured spectrum of the triton particles. Figure 2.15 shows the unfolded neutron flux per unit lethargy as a function of neutron energy from 10 keV to 600 keV. In the energy range from 200 keV to 400 keV, the flux per unit lethargy, $\phi(u)$, experiences a large decrease in magnitude. This may be an anomaly due to the presence of the Li^6 cross-section resonance at about 250 keV, even though this spectrum has been corrected with the response function calculated from the Cf^{252} neutron spectrum measurements. The

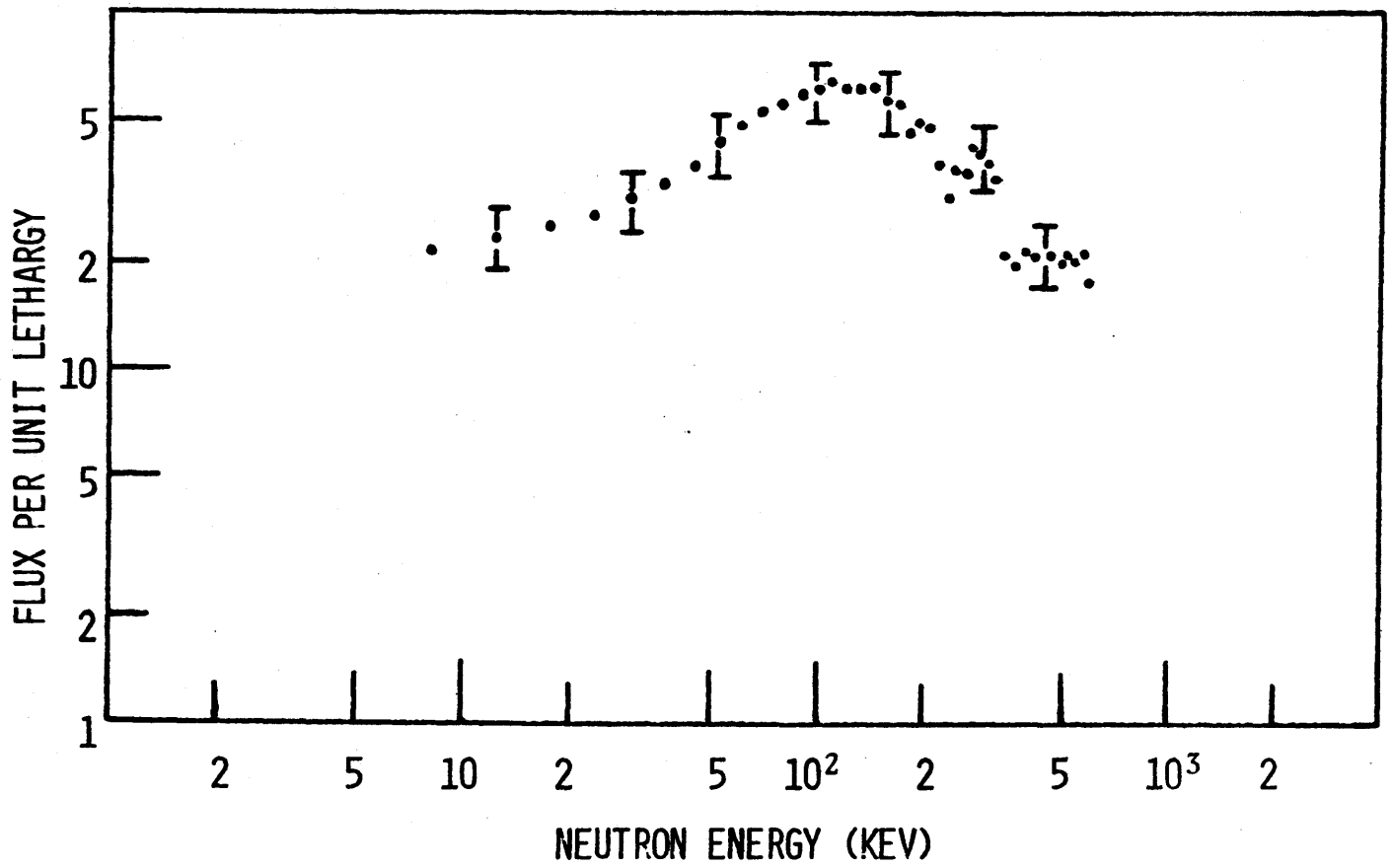

FIG. 2.15 NEUTRON SPECTRUM IN BLANKET MOCKUP NO. 2 Li-6 DETECTOR-TRITON METHOD

presence of large scattering resonances at 250 keV and 400 keV in sodium and oxygen also contributes to a decrease in neutron flux.

Figure 2.16 shows the neutron flux per unit lethargy as a function of neutron energy, obtained by combining the results of the Triton and Sum Methods.

2.6 Proton-Recoil Proportional Counter

2.6.1 Basic Considerations

Proton-recoil proportional counters have been used extensively to measure neutron spectra (1,2). In a neutron-proton collision, all neutron energies below that of the incident neutron energy are equally probable. This rectangular response function of the proton spectrum has to be unfolded to arrive at the neutron spectrum. One method of unfolding consists of differentiation of the proton-recoil distribution. The relationship between the corrected proton-recoil distribution, M(E), and the neutron flux per unit lethargy, $\phi(u)$, is

$$\phi(u) = - \frac{E^2}{NT\sigma_H(E)} \frac{dM(E)}{dE} \qquad (2.12)$$

where

$\sigma_H(E)$ is the neutron-proton scattering cross section.

Two detectors were used in the measurements; the smaller detector is filled with about 8 atm of predominately hydrogen gas. It was used to measure proton-recoil spectra below 100 keV. The larger detector is filled with about 3 atm of predominately methane gas. The methane detector was used for energies greater than 100 keV.

A block diagram of the system is shown in Fig. 2.17. The system has two channels, the energy channel and the rise-time-to-amplitude converter channel. The former records a pulse whose height is proportional to the ionization. The other channel measures the rise time of the pulses, which is used to reject gamma-induced events.

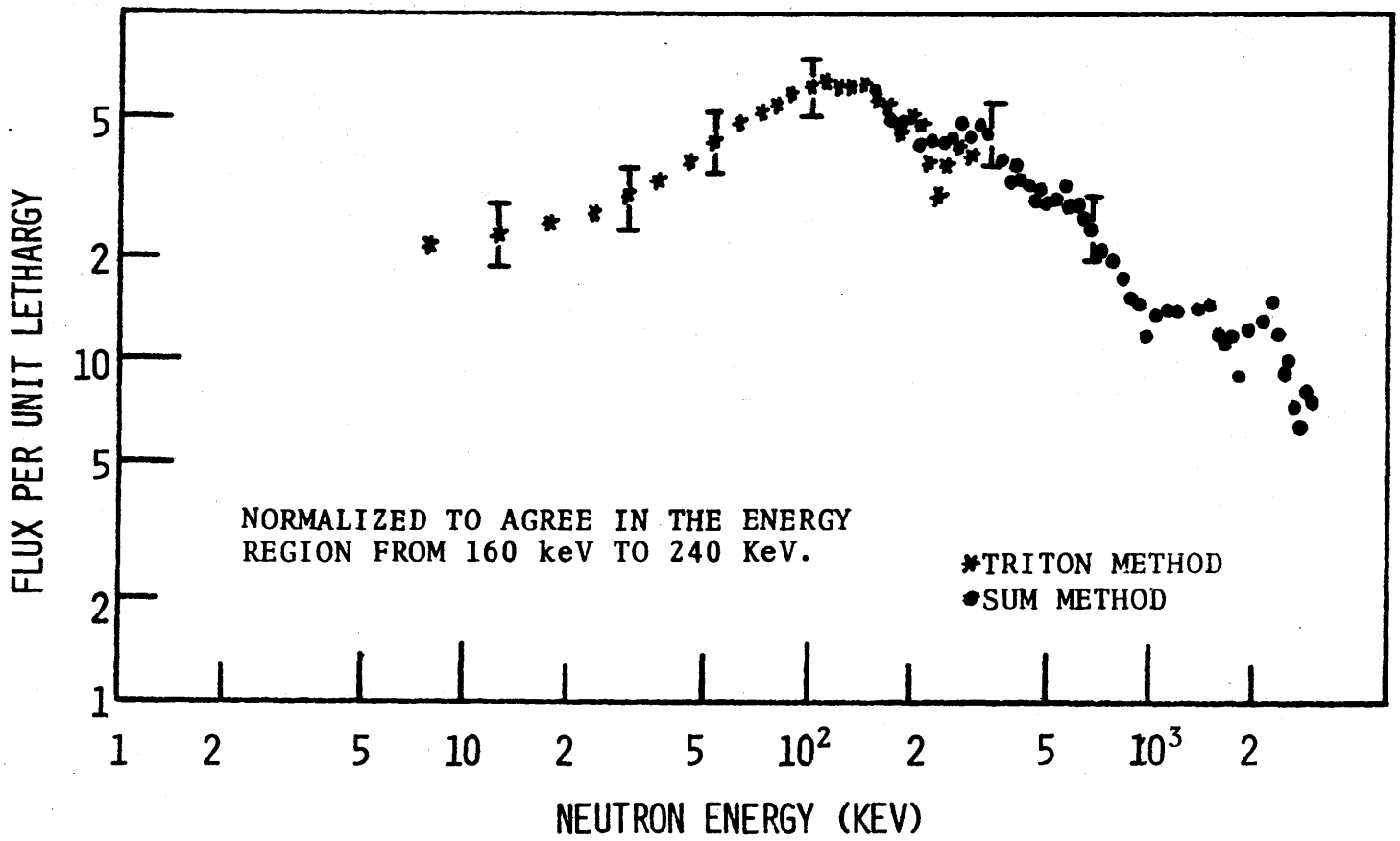

FIG. 2.16 NEUTRON SPECTRUM IN BLANKET MOCKUP NO. 2 Li-6 SEMICONDUCTOR DETECTOR

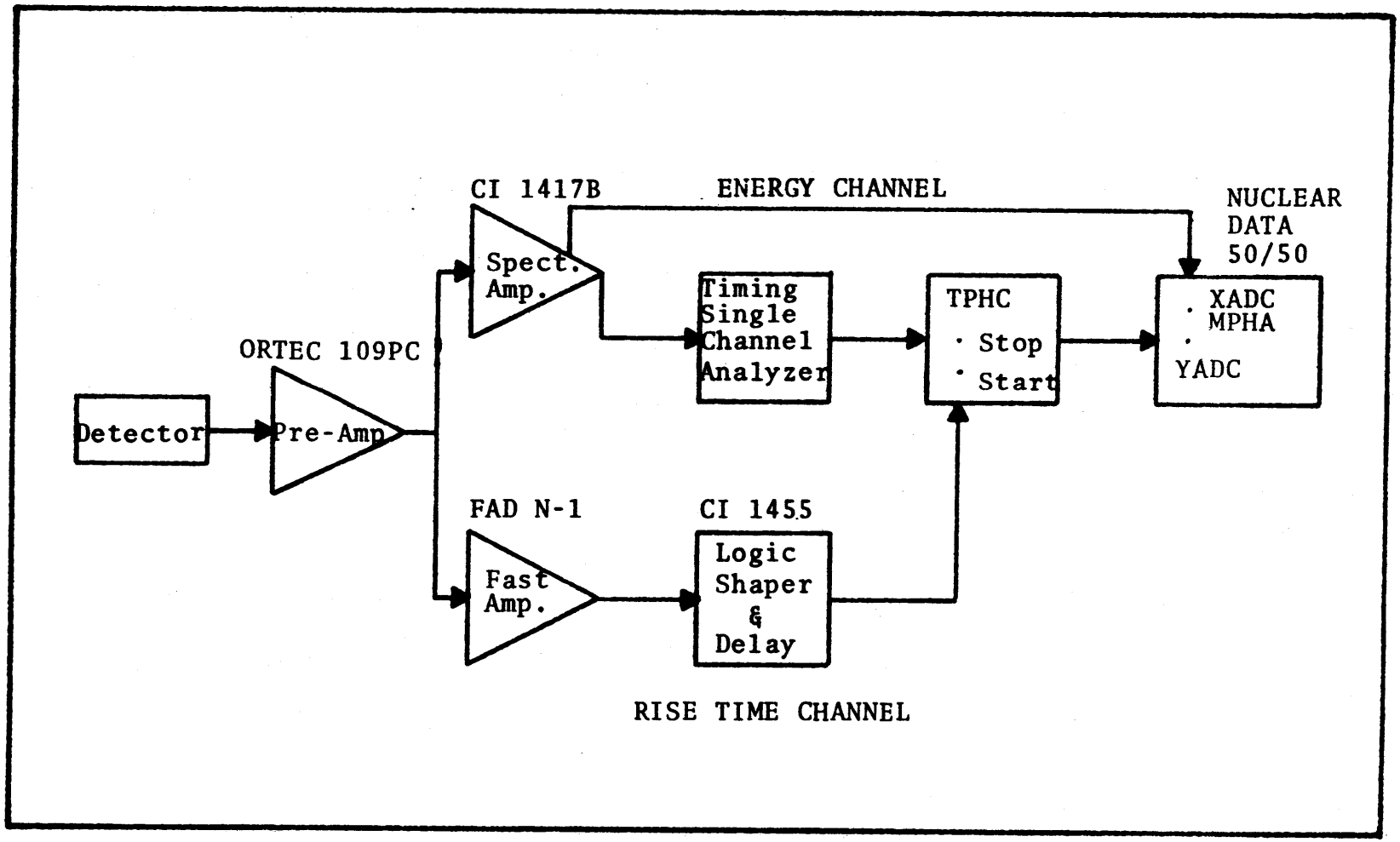

FIG. 2.17 BLOCK DIAGRAM OF THE SYSTEM USED FOR NEUTRON SPECTROSCOPY WITH PROTON-RECOIL PROPORTIONAL COUNTERS

2.6.2 Unfolding of Neutron Spectra from Proton-Recoil Distributions

The computer program PSNS written at ANL (16) was used to unfold the measured proton-recoil spectrum. The original program was rewritten in Fortran IV language and the energy dependence of W (energy per ion pair) was modified to include the results of recent measurements (17). Corrections for wall-and-end effects, and the recoil of heavy nuclei are also included in the program. The calculation of the neutron flux per unit lethargy is based on Eq. 2.12, and the results are given at a constant fractional energy increment.

2.6.3 Experimental Results

The fast neutron spectrum was measured over the energy region from 2 keV to 1.5 MeV in Blanket Mock-Up No. 2. Data were obtained with the hydrogen-filled counter using eight high voltage settings at 150-volt intervals, beginning at 3250 volts. The methane-filled detector was used with high voltage settings of 3200 volts, 3500 volts and 3750 volts. An energy overlap was maintained between the two counters to assure that the data were properly normalized. The three methane-filled counter data sets were also overlapped in energy.

The neutron spectrum is shown in Fig. 2.18. Depressions due to various scattering resonances are seen: oxygen resonances at 400 keV and 1 MeV, a chromium resonance at 50 keV, an iron resonance at 30 keV and a sodium resonance at 3 keV. The experimental error varies from about ±13% over most of the energy range to almost ± 33% in the region around 3 keV, where the statistics of ionization become very poor.

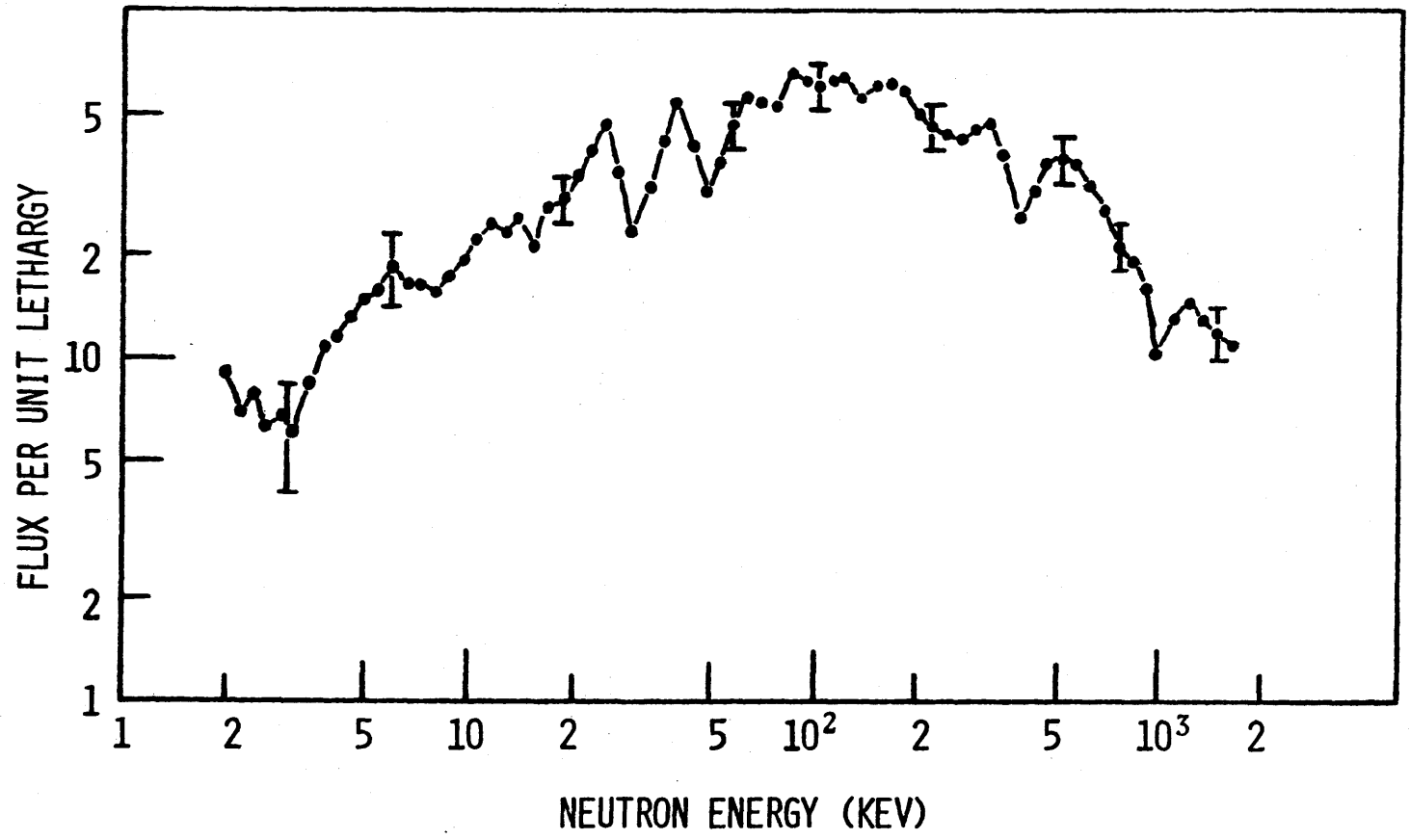

FIG. 2.18 FAST NEUTRON SPECTRUM IN BLANKET MOCKUP NO.2, PROTON RECOIL PROPORTIONAL COUNTER

2.7 Results and Conclusions

2.7.1 Discussion of Results

This work has involved evaluation of different instrumental methods for measuring the fast neutron spectrum in Blanket Mock-Up No. 2. The methods applied are shown in Table 2.4. In this final section, the experimental results from previous chapters are intercompared. They are also compared with numerical calculations from the ANISN code, and to foil activation measurements.

2.7.1.2 Intercomparison of Present Results

The results obtained with the He^3 semiconductor detector operating in the Sum and Difference Modes are in reasonable agreement (Fig. 2.10). The He^3 Sum Method results are also in good agreement with the Li^6 semiconductor detector Sum Mode measurements over the energy region from 200 keV to 1.1 MeV (Fig. 2.19). In the low-energy region (10 keV to 100 keV), the He^3 Difference Method results differ from those obtained using the Li^6 detector (Fig. 2.20). This is mainly due to the effect of the discriminator setting on the He^3 Difference Method, which introduces large uncertainties and reduces the sensitivity for measuring low-energy neutrons. The results from the Li^6 semiconductor detector and the Proton-Recoil proportional counter are in very good agreement over the entire energy range of the measurements (Fig. 2.21).

2.7.1.3 Comparison with ANISN Calculations

The one-dimensional transport code ANISN, with the ABBN cross section set and self-shielded U^{238} cross sections, was used in the S_8 option to calculate the theoretical neutron spectrum in Blanket No. 2, at 24.75 cm into the blanket (18). Figure 2.22 shows the 26-group calculation and the experimental results obtained by collapsing the Proton-Recoil data into the same group structure. Relatively poor agreement in the low-energy region is observed between the calculated and measured spectra; the former shows a

TABLE 2.4

Summary of Instrumental and Unfolding Methods Used to Measure the Fast Neutron Spectrum

Detector	Operating Mode	Unfolding Method	Remarks
He-3	Sum	direct	See Figs. 2.8 and 2.19 for results.
	Difference	integral	See Figs. 2.10 and 2.11 for results.
		derivative	See Fig. 2.11 for results.
Li-6	Sum	direct	See Figs. 2.13 and 2.19 for results.
	Difference	integral	See Fig. 2.14 for results.
		derivative	It was not successfully employed on the Li-6 data. See section 2.5.3.4.
	Triton	integral	See Figs. 2.15 and 2.21 for results.
Proton-Recoil		derivative	PSNS code from ANL. See Figs. 2.18 and 2.21 for results.

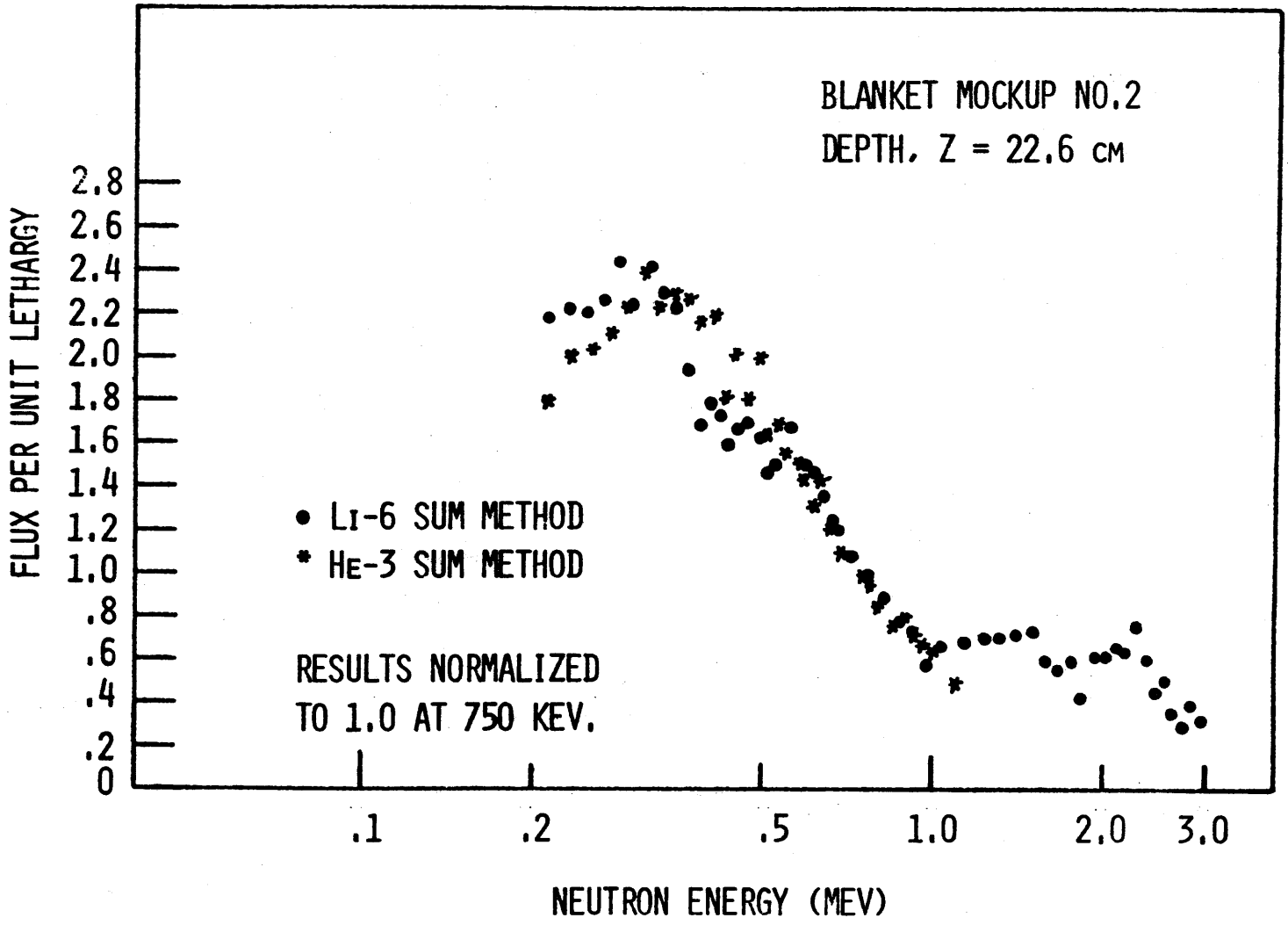

FIG. 2.19 COMPARISON OF NEUTRON SPECTRA FOR THE LI-6 AND HE-3 SUM METHODS

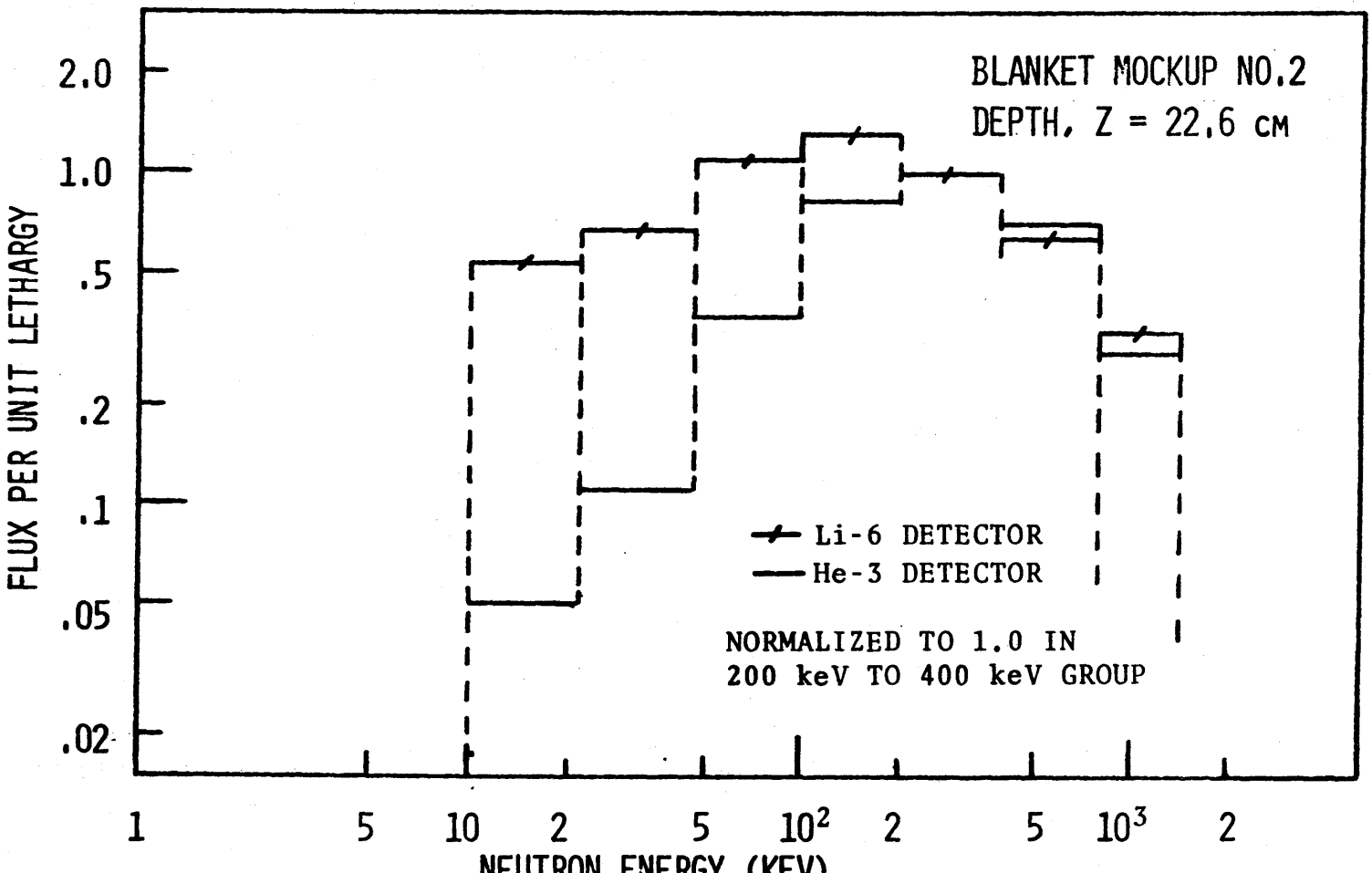

FIG. 2.20 COMPARISON OF NEUTRON SPECTRA FOR Li-6 AND He-3 DETECTORS IN DIFFERENCE MODE

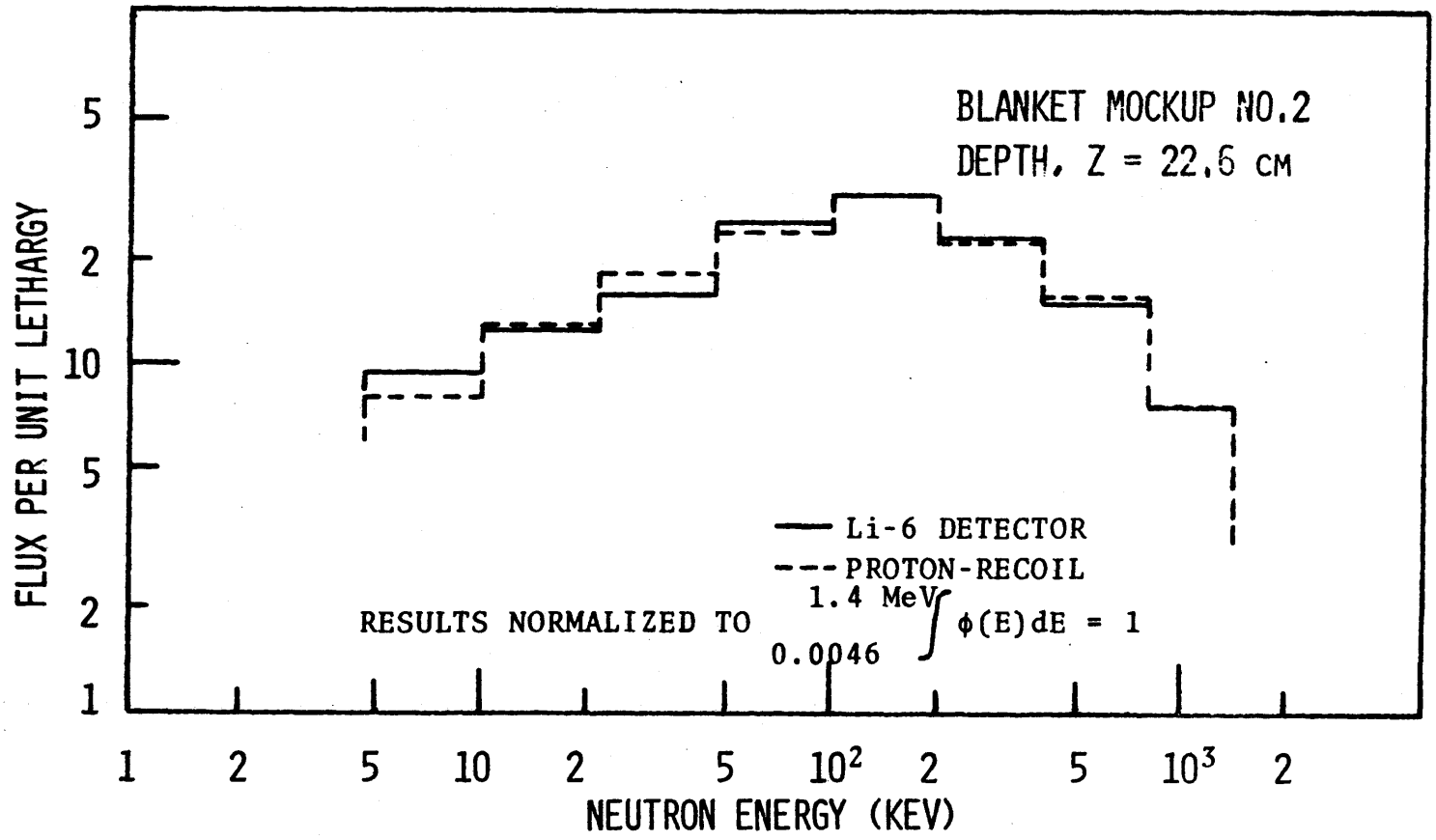

FIG. 2.21 COMPARISON OF NEUTRON SPECTRA FROM PROTON-RECOIL AND Li-6 DETECTORS

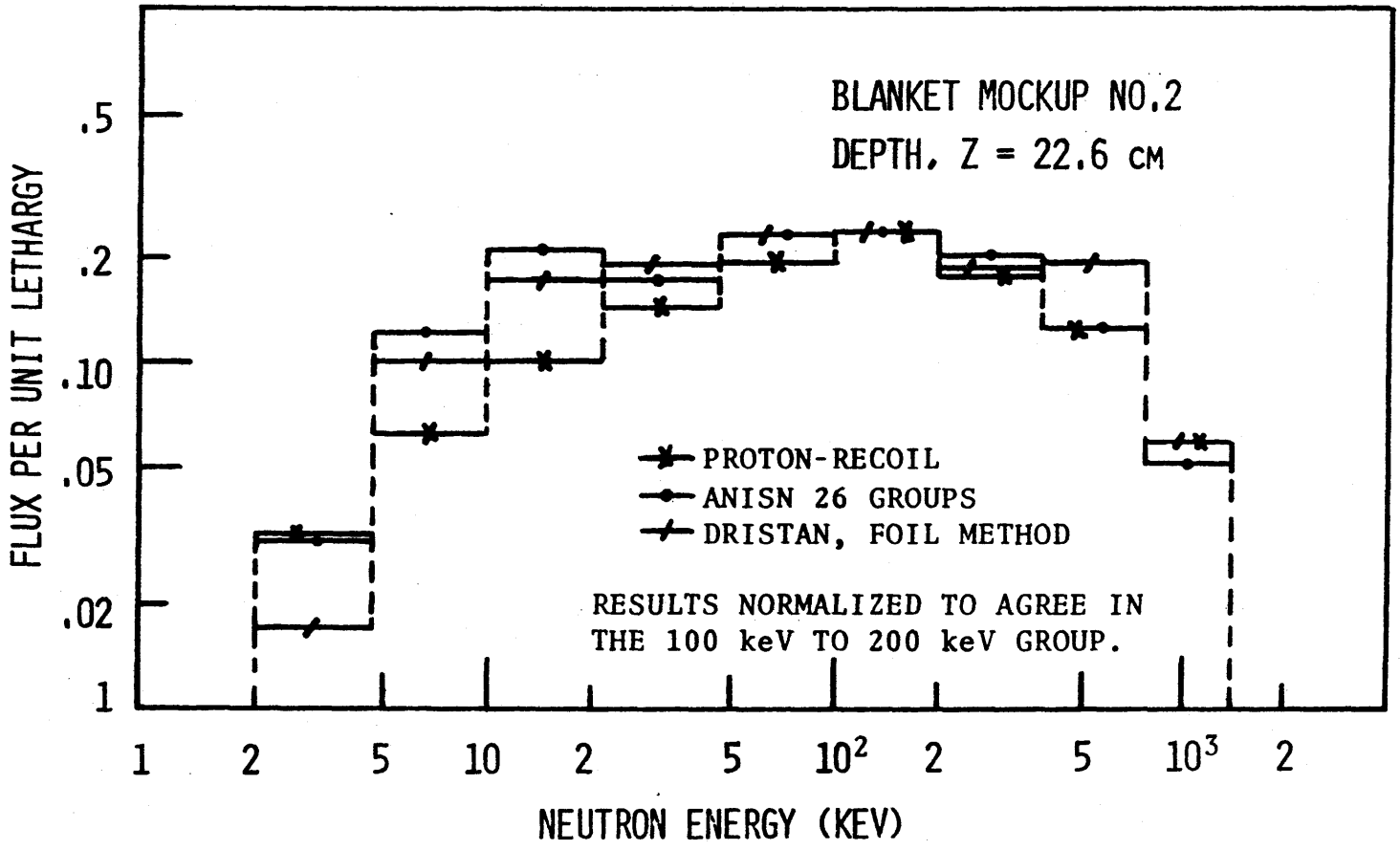

FIG. 2.22 COMPARISON OF 26 GROUP RESULTS

flatter distribution in the energy region from 5 keV to 100 keV. A likely explanation is that the averaging-out of the iron and chromium scattering resonances involved in the original preparation of the 26-group cross section set has contributed errors which lead to overestimation of the neutron flux in that energy region. The good agreement obtained between the different instrumental measurements, however, engenders considerable confidence in the reliability of the experimental results: different combinations of detectors, operating modes and unfolding techniques all gave comparable results.

2.7.1.4 Comparison with Foil Results

The three-foil experimental data unfolded by Leung with the DRISTAN code (18) are shown in Fig. 2.22 together with the Proton-Recoil results. The agreement is again poor in the low-energy region. Leung's results are subject to the same source of systematic error in the iron and chromium scattering cross sections as the ANISN calculations, since his unfolding method is based upon fitting to a smooth slowing-down density and extracting the flux through division by $\xi\Sigma_T$. Leung used the ABBN cross section set to determine $\xi\Sigma_T$, which may explain the consistency of his results with the ANISN calculations using the same cross section set. Foil experiments which include a larger number of foils sensitive in the energy region from 3 keV to 50 keV should be performed to resolve the discrepancy. Leung's unfolding method should also be applied using $\xi\Sigma_T$ values derived from an independent source.

2.7.1.5 Comparison with Ge(Li) Data

The neutron spectrum above 0.8 MeV leaking from Blanket Mock-Up No. 2 was measured by C. S. Kang (13) using a Ge(Li) crystal and a novel approach based on gamma line broadening. His results and the measurements from the Li^6 Sum Method are compared in Fig. 2.23. There is relatively good agreement between the experimental results.

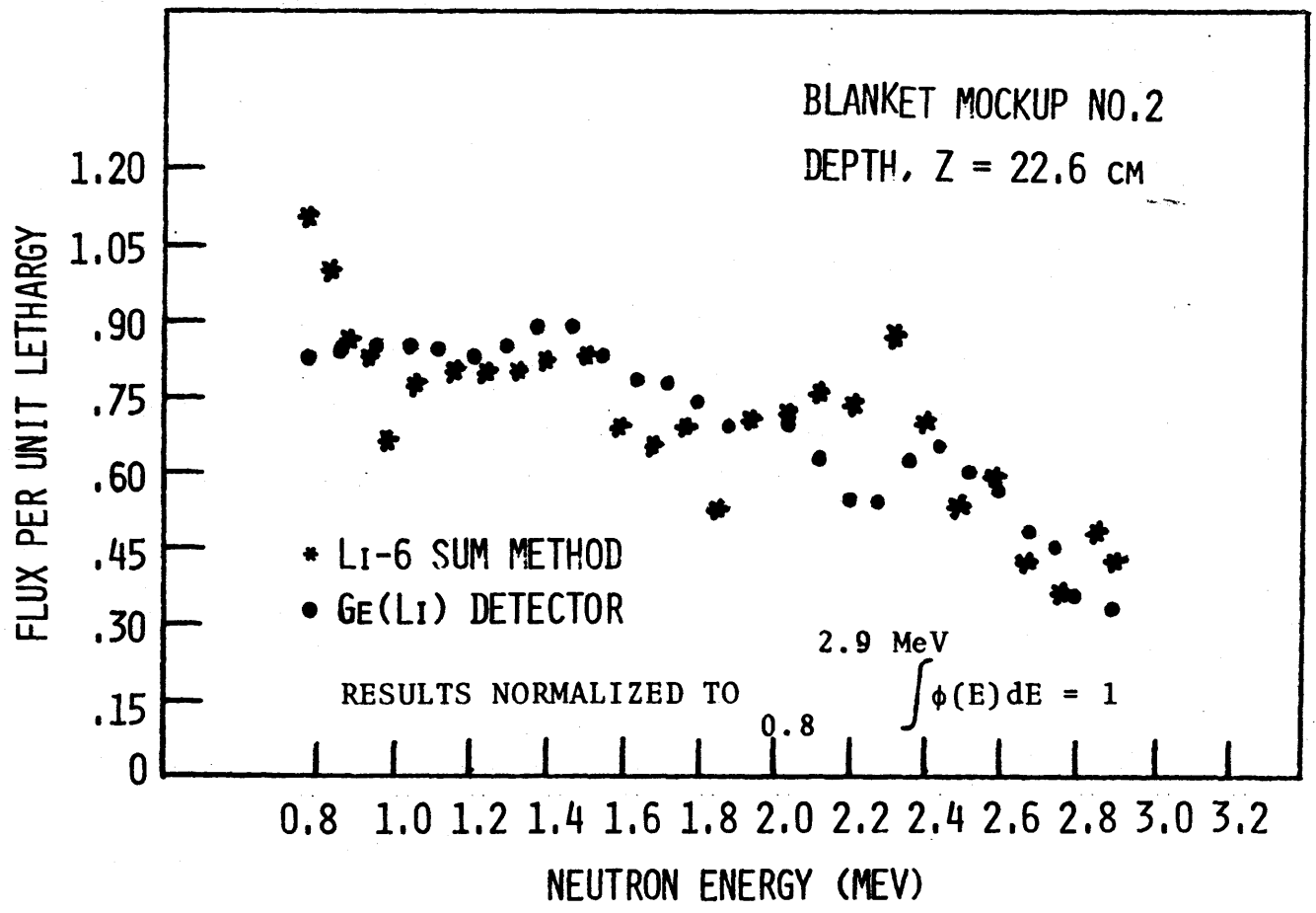

FIG. 2.23 COMPARISON OF NEUTRON SPECTRA FOR Li-6 SUM METHOD AND GE(Li) DETECTOR

2.7.1.6 Comparison with ZPPR-2-Core-Neutron Spectrum

The converter lattice that provides the fast neutron spectrum to drive Blanket Mock-Up No. 2 was designed (3) to achieve a neutron leakage spectrum similar to that of the ZPPR-2 Core. Figure 2.24 shows the ZPPR-2-Core-Neutron Spectrum (19) and the Blanket Mock-Up No. 2 Neutron Spectrum, both measured with Proton-Recoil proportional counters. The experimental results were collapsed into the same group structure. Both neutron spectra have a similar shape, but the Blanket Mock-Up No. 2 spectrum is systematically softer, as expected. As shown in Fig. 2.25, the fine-group spectra show the same characteristic signature of the scattering resonances in sodium, iron, chromium and oxygen.

2.7.2 Conclusion

In conclusion, the results from the instrumental methods used in this work are in relatively good agreement and no unexplained behavior was observed in the neutron spectrum measurements from 2 keV to 3.1 MeV. This result inspires further confidence in the Blanket Test Facility concept as a valid technique to study mock-ups of LMFBR blankets.

Further work is called for in the areas of numerical calculations of spectra and foil unfolding methods. Finally, for general purpose use in future mock-up runs, it is recommended that the Li^6 detector be used: it has better performance characteristics overall than the He^3 system and is considerably more convenient than the Proton-Recoil system.

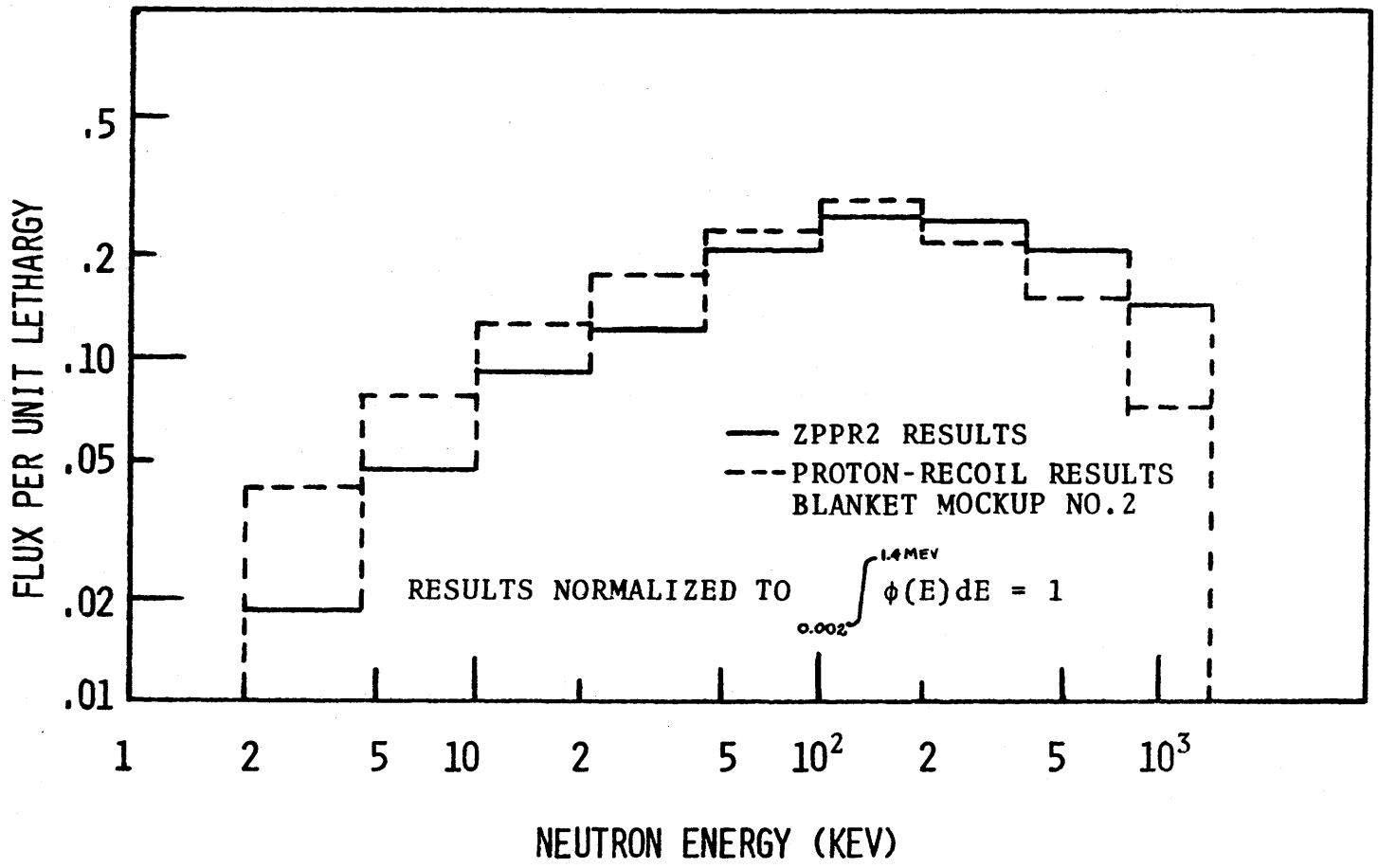

FIG. 2.24 COMPARISON OF ZPPR-2 AND BLANKET MOCKUP NO. 2 SPECTRA

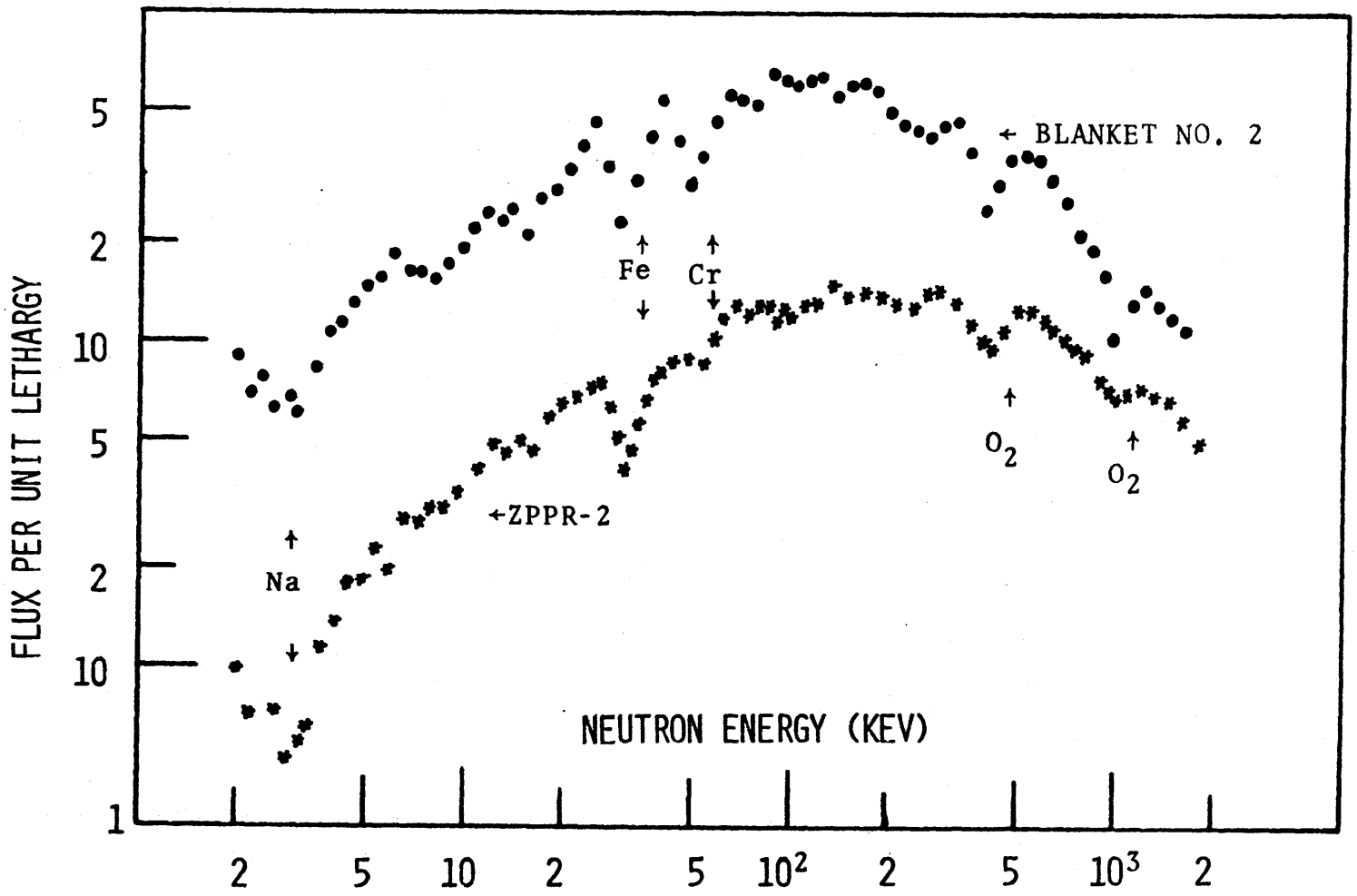

FIG. 2.25 COMPARISON OF ZPPR-2 AND BLANKET MOCKUP NO. 2 FINE-GROUP SPECTRA

2.8 References

(1) Bennett, E.F., Nucl. Sci. and Eng., 27, 28-33 (1967).

(2) Bennett, E.F., Nucl. Sci. and Eng., 27, 16-27 (1967).

(3) Forbes, I.A., "Design, Construction and Evaluation of a Facility for the Simulation of Fast Reactor Blankets," MIT-4105-2, MITNE-110 (February, 1970).

(4) LMFBR Blanket Physics Project Progress Report No. 1, MIT-4105-3, MITNE-116 (June, 1970).

(5) Maroni, C., Russo, F. and Verondini, E., Nucl. Instr. and Meth., 74, 256-260 (1969).

(6) Gold, R., "An Iterative Unfolding Method for Response Matrices," ANL-6984, December, 1964.

(7) Instruction Manual 525: Neutron Spectrometer System, ORTEC.

(8) Green, L., Nucl. Sci. Eng., 37, 232-242 (1969).

(9) Rickard, I.C., Ph.D. Thesis, University of London (1971).

(10) Silk, M.G., Nucl. Instr. and Meth., 66, 93-101 (1968).

(11) Bluhm, H. and D. Stegemann, Nucl. Inst. and Meth., 70, 141-150 (1969).

(12) Yule, T.J. and Bennett, B.F., Nucl. Sci. and Eng., 46, 236-242 (1971).

(13) Kang, C.S., "Use of Gamma-Spectroscopy for Neutronic Analysis of LMFBR Blankets," MIT-4105-8, MITNE-130 (January, 1972).

(14) Mahaux, C. and Robaye, G., Nucl. Phys., 74, 165-171 (1965).

(15) Meadows, J.W., Phys. Rev., 157, 1076 (1967).

(16) Bennett, E.F., R. Gold and I.K. Olson, ANL-7394, Argonne National Laboratory (1968).

(17) Werle, H., Fieg, G., Seufert, H., Stegemann, D., Nucl. Instr. and Meth., 72, 111 (1969).

(18) Leung, T.C. et al., "Neutronics of an LMFBR Blanket Mock-Up," COO-3060-1, MITNE-127 (January, 1972).

(19) Simons, G. G., "Fast Neutron Spectrum Measurements in the ZPPR and ZPR-3 Critical Assemblies," in ANL-APD Annual Report July 1, 1969 to June 30, 1970, ANL-7710.

3. FOIL METHODS FOR NEUTRON SPECTROMETRY

3.1 Introduction

While instrumental methods for neutron spectroscopy have some compelling advantages, there are at least two areas in which their shortcomings invite development of alternate approaches. First, they provide no information on the spectrum below several (or in some cases, several hundred) keV, a region of considerable interest in the blanket-reflector region of the LMFBR. Second, in some environments, particularly if one contemplates measuring spectra in operating LMFBR's, the instrumental spectrometers cannot be employed at all due to high background or excessive radiation damage.

The use of multiple foil activation methods for spectrum determination is of long standing and several comprehensive reviews of past progress have been published (1, 2, 3). Nevertheless, further work is still called for in order to meet some of the specific requirements established for the present task, and also to further the development of improved methods for unfolding neutron spectra from the foil data – at present a major drawback to more widespread reliance on foil methods.

3.2 Criteria for LMFBR Foil Method

The foil method now being investigated as part of the blanket research program has evolved from previous work at M.I.T. (4, 5) and has been further modified to satisfy a number of additional criteria. For this reason, it is worthwhile to review the many criteria and exercises of judgment involved in arriving at the present approach:

(1) Encapsulated mixtures of powders are being employed, and the activated samples are counted using high-resolution Ge(Li) detectors based on the following rationale:

(a) Mixing fine powders reduces resonance self-shielding effects and the attendant necessity for correction of the cross section data to account for them.

(b) The one-step counting procedure and use of available data analysis codes such as GAMANL greatly reduces the amount of tedious (and error-introducing) intermediate steps involved in conventional foil methods.

(c) It is easier to find compounds which are suitable for high temperature service than forms which can be fabricated into foils.

This approach was adopted despite the recognized disadvantage that it eliminates potential target materials which produce identical activation products, such as all fissionable materials, and other combinations (e.g., $Na^{23}(n,\gamma)$, $Mg^{24}(n,p)$, $Al^{27}(n,\alpha)$, and a few others which produce gamma lines too close for independent resolution (e.g., In(n,n') and La(n,γ)).

(2) Materials were selected with half lives greater than about one hour and less than roughly one month: the lower limit to allow for handling time and the upper because we wish to reuse foil capsules and also to calibrate them in a thermal spectrum in order to increase experimental precision. This latter objective, and also the greater interest in keV-region spectra, indicates preference for nonthreshold type absorbers.

(3) Other obvious criteria also apply: the material must activate sufficiently in a LMFBR spectrum, decay with sufficiently energetic, high-yield gammas to facilitate detection, and not contain isotopes which produce unwanted background in the composite gamma spectrum.

With these criteria in mind, a comprehensive survey of potential capsule constituents has been started, as described in the following section.

3.3 Selection of Candidate Foil Materials

Based upon the criteria just listed, a series of screening tests was carried out on the entirety of the periodic table of elements, including irradiation of samples in the blanket test facility. The results are summarized in Table 3.1.

As can be seen from this preliminary evaluation, only six materials (Na, Mn, As, In, La, Au) have qualified, five have been selected for further screening and four are yet to be evaluated. Although this may appear to be a rather sparse selection, it is also an unfortunate reality of foil methods that cross section shapes are so similar over broad energy ranges that one could not make very productive use of a larger number of activation products.

In addition to selection of the foil materials, the screening tests have also been employed to select candidate capsule materials, together with the additional criteria that they be compatible with exposure to high temperature sodium. Both vanadium and niobium appear equally suitable; both were used as cladding in the original Dounreay FBR core, and neither activates substantially in an LMFBR spectrum. Further tests will be conducted to select one of the two as a final choice.

3.4 Comments and Conclusions

In addition to selection of appropriate foil materials, one must have available a satisfactory means for unfolding neutron spectra from the activation data. Methods employed at M.I.T. to date have included an approach developed by Leung (6), and the SAND-II program. The former appears to overly restrict the shape of the allowable flux, while the latter appears to be overly flexible (7). Thus, current efforts have been devoted to evaluation of an improved version of the SPECTRA code (8, 9). Results to date are too preliminary to draw any definitive conclusions.

Considerable work remains to be done in this area: completion of screening tests, demonstration applications using prototype capsules including thermal spectrum calibration, and final selection of a well-evaluated version of a spectrum unfolding program. All but the last of these tasks should be completed during the coming year.

TABLE 3.1

Screening of Candidate Foil Materials

Z	Element	Rating	Z	Element	Rating	Z	Element	Rating
1	H	RN	29	Cu	Xa	57	La	C
2	He	RG	30	Zn	XH	58	Ce	T
3	Li	RN	31	Ga	T	59	Pr	T
4	Be	RN	32	Ge	T	60	Nd	RH
5	B	RN	33	As	C	61	Pm	RG
6	C	RN	34	Se	XA	62	Sm	S
7	N	RN	35	Br	RI	63	Eu	RH
8	O	RN	36	Kr	RG	64	Gd	RI
9	F	RH	37	Rb	XA	65	Tb	RH
10	Ne	RG	38	Sr	RA	66	Dy	S
11	Na	C	39	Y	RA	67	Ho	RH
12	Mg	RI	40	Zr	XA	68	Er	RI
13	Al	RI	41	Nb	XA	69	Tm	RH
14	Si	RAH	42	Mo	XAI	70	Yb	RI
15	P	RA	43	Tc	RG	71	Lu	RA
16	S	RA	44	Ru	XA	72	Hf	RI
17	Cl	XA	45	Rh	XH	73	Ta	XH
18	Ar	RG	46	Pd	S	74	W	XI
19	K	RH	47	Ag	XH	75	Re	XA
20	Ca	RA	48	Cd	XA	76	Os	RI
21	Sc	RIH	49	In	C	77	Ir	XH
22	Ti	S	50	Sn	RH	78	Pt	RI
23	V	XA	51	Sb	XH	79	Au	C
24	Cr	XA	52	Te	RIH	80	Hg	XA
25	Mn	C	53	I	XA	81	Tl	RH
26	Fe	XA	54	Xe	RG	82	Pb	RN
27	Co	RI	55	Cs	XH	83	Bi	RN
28	Ni	XAH	56	Ba	S	$\geq$ 84	Various	RGI

Key:

R = rejected without irradiation

X = rejected after irradiation screening

S = selected for further screening tests

G = inert gas, or does not occur in nature

N = no useful activation product for present purposes

I = unwanted radionuclides activated for present purposes

A = insufficient activation or gamma yield

T = still to be evaluated

H = undesirable half life

C = selected for use -- passes all tests

3.5 References

(1) Zijp, W.L., "Review of Activation Methods for the Determination of Fast Neutron Spectra," RCN-37 (May 1965).

(2) Zijp, W.L., "Review of Activation Methods for the Determination of Intermediate Neutron Spectra," RCN-40 (October 1965).

(3) Muller, M., "Measurement of Neutron Spectra Within the 1-eV to 10-keV Energy Range by Means of the Sandwich Technique," EUR FNR-842 (July 1970).

(4) Ho, S.L., "Measurement of Fast and Epithermal Neutron Spectra Using Foil Activation Technique," S.M. Thesis, M.I.T. Nuclear Engineering Department (January 1970).

(5) Passman, N.A., "An Improved Foil Activation Method for Determination of Fast Neutron Spectra," S.M. Thesis, M.I.T. Nuclear Engineering Department (January 1971).

(6) Leung, T.C. et al., "Neutronics of an LMFBR Blanket Mock-Up," COO-3060-1, MITNE-127 (January 1972).

(7) Newman, D.F., "Determination of the Absolute Neutron Flux Spectrum in the PCTR Fast Neutron Cavity from Multiple Foil Activation Measurements," S.M. Thesis, University of Washington (1970).

(8) Greer, C.L. et al., "A Technique for Unfolding Neutron Spectra from Activation Measurements," SC-RR-67-746 (November 1967).

(9) Fischer, A. and Turi, L., "The RFSP Programme for Unfolding Neutron Spectra from Activation Data," INDC (HUN)-8/U, IAEA (May 1972).

4. BLANKET MOCK-UP NUMBER 3

4.1 Introduction

One of the major objectives of the blanket research program has been the acquisition of experimental data against which the adequacy of multigroup calculations can be tested. Methods and cross section sets previously proven adequate for core calculations will not necessarily suffice for blanket calculations owing to the severe spatial attenuation and spectral degradation of the flux. This uncertainty is accentuated where high-albedo blanket reflectors such as graphite or beryllium are employed, since they are also good moderators. In such cases, self-shielding effects in U^{238} are of particular concern.

The material activation traverses reported in this chapter were measured on Blanket Mock-Up No. 3 – a graphite-reflected assembly – and, therefore, constitute a useful benchmark against which the methods used to calculate blanket performance using advanced reflector designs can be tested.

A detailed description of the design and construction of the Blanket Test Facility (BTF) used to drive the blanket mock-ups irradiated under this program is presented in reference (1). For present purposes, the only point requiring reiteration is that the BTF converter provides neutrons closely simulating the leakage spectrum from an LMFBR core.

To date, three blankets have been irradiated: the first contained no uranium and was only used to evaluate facility performance. Blanket No. 2, however, was an accurate mock-up of a typical LMFBR blanket, consisting of three rows of fuel-containing subassemblies and a steel reflector. The results of the test program using this blanket have been documented in a series of reports (2, 3, 4, 5, 6). Blanket No. 3, the present subject, was designed to incorporate a graphite reflector region in place of the third row of fuel in Blanket No. 2: otherwise, all important characteristics were

kept the same. Section 4.2 reviews the design and construction of Blanket No. 3; section 4.3 discusses the experimental program, whose results are presented and analyzed in section 4.4. Conclusions and comments are outlined in section 4.5.

4.2 Description of Blanket Mock-Up No. 3

4.2.1 General Description

Figure 4.1 shows a schematic view of the BTF Blanket Mock-Up No. 3 assembly on its cart, including the uranium subassemblies, and the graphite and steel reflectors. The support structure for the assembly consists of two pieces of 1 inch by 60 inches by 39 inches and one piece of 1 inch by 62-7/16 inches by 58-1/4 inches hot-rolled, mild steel plates, welded to make an H-frame. The H-frame support structure and cart for this mock-up are identical to those used for Blanket Mock-Up No. 2 except for an additional steel plate, 0.5 inch by 23 inches by 61 inches, welded to the bottom of the cart, providing the necessary overhang to support the uranium subassemblies and graphite reflector on the front half of the H-frame.

There are 19 full subassemblies (5-13/16 inches by 5-13/16 inches by 60 inches) arranged in two rows. The full-size subassemblies are filled with steel-clad uranium rods and sodium chromate. The two half-size peripheral subassemblies, used to provide a staggered array, are filled with a mixture of iron and borax, shown to be a good representation of a fueled assembly in the work on Blanket No. 1 (1).

Forty-three foil tubes are provided for the irradiation of various foils in the blanket and reflector in the axial and transverse directions, as depicted in Fig. 4.2. The foil tubes are mild steel tubing of 7/16-inch outside diameter, 0.028 inch thick and 58 inches long, and are held in place by the top and bottom grid plates in each subassembly.

4.2.2 Blanket Subassembly Description

The subassemblies for Blanket Mock-Up No. 3 are identical to those used in Blanket Mock-Up No. 2. A detailed description of these subassemblies is given in reference (5) and is included here for completeness.

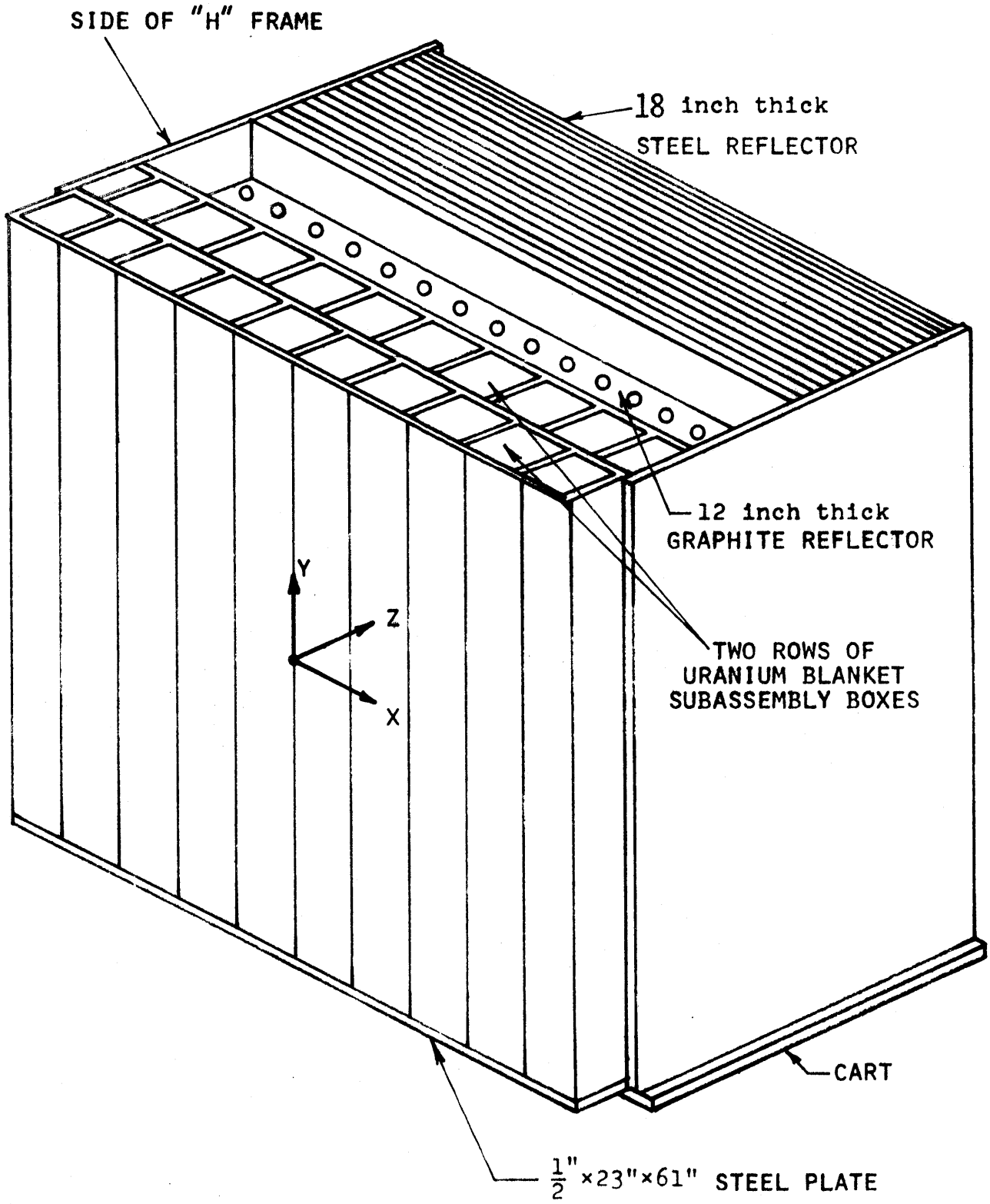

FIG 4.1 SCHEMATIC VIEW OF BLANKET MOCK-UP NO. 3
WITH GRAPHITE REFLECTOR

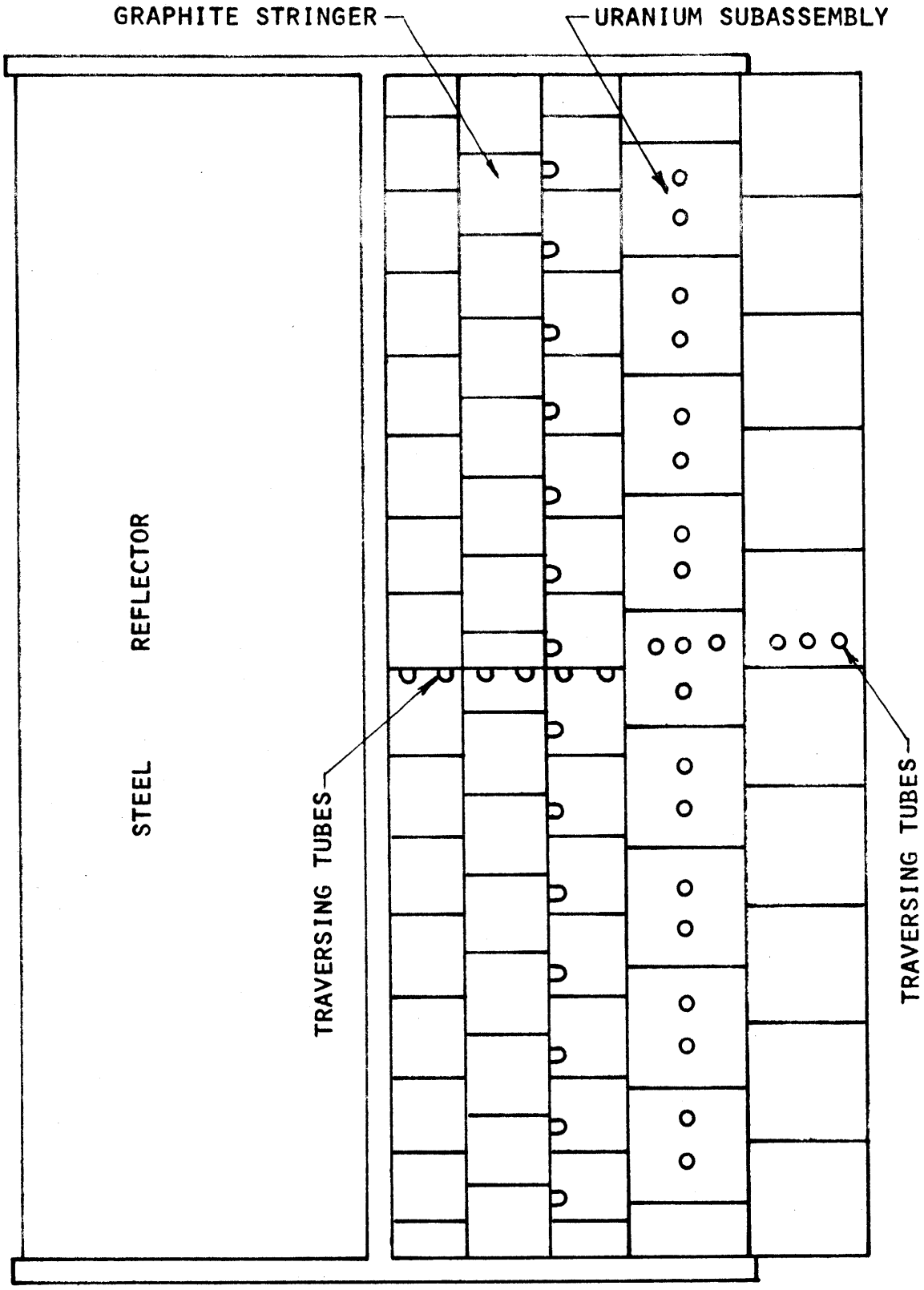

FIG. 4.2 OVERHEAD VIEW OF BLANKET MOCK-UP NO. 3

Each subassembly box has a wall thickness of approximately 3/32 inch and a seal-welded bottom closure plate. It contains 121 fuel rods arranged in an 11 by 11 square lattice whose pitch is 0.511 inch (Figs. 4.3 and 4.4). The uranium metal rods are 0.250 inch in diameter and 48 inches in length. Sixty of the rods have a U^{235} enrichment of 1.016%, and sixty-one have a U^{235} enrichment of 1.134%; the two enrichments are loaded in a checkerboard pattern within the subassembly box. The uranium metal rods are clad in low-carbon, mild steel tubing. The clad tubing dimensions are 5/16-inch O.D., 0.018-inch wall thickness and 50 inches in length. Each end of the tube is closed by a press-fitted steel plug, 1/2 inch long by 9/32 inch O.D. This arrangement leaves a one-inch free space in the tube to allow for dimensional variations and fuel expansion. The fuel rods are held in place by aluminum bottom and top grid plates, 1/4 inch in thickness.

Technical grade anhydrous sodium powder, Na_2CrO_4, baked at 400° F to decrease the water content to less than 0.1%, and ground into a uniform powder, occupies the inter-rod volume. Each subassembly is sealed by a 0.035-inch-thick steel top plate, epoxied in place to make the subassembly air- and water-tight. Figure 4.5 shows the cross-sectional view of the blanket subassembly.

A breakdown of the average subassembly weight is given in Table 4.1 (as reported in reference (5)).

TABLE 4.1

Subassembly Component Weights

Uranium metal	89.30 Kg
Na_2CrO_4	31.11 Kg
Cladding	13.00 Kg
Subassembly box	26.55 Kg
Grid plate support tubes	0.91 Kg
Grid plates	0.36 Kg
Total	161.23 Kg

FIG. 4.3 GRID PLATE FOR BLANKET NO. 3 SUBASSEMBLIES

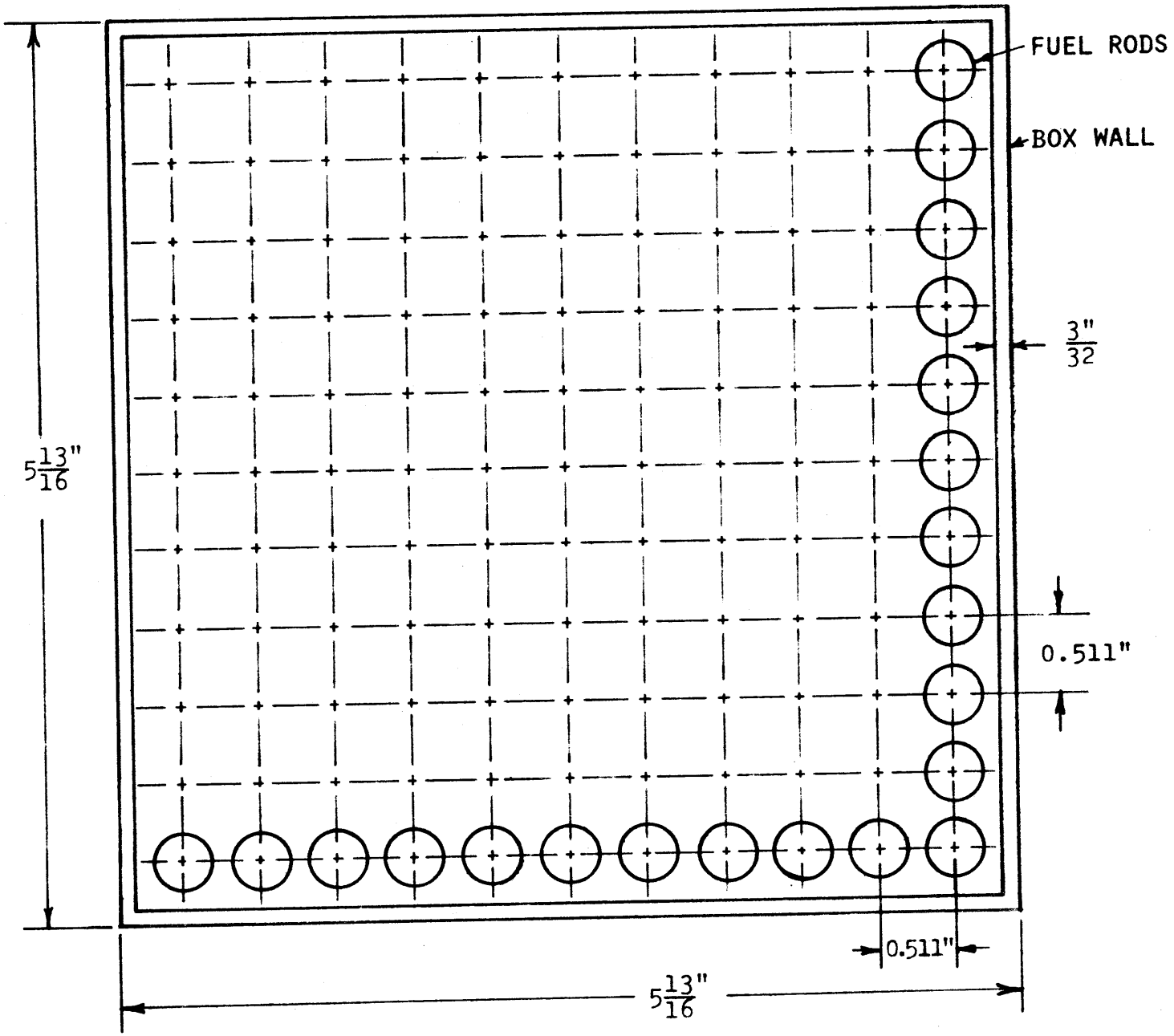

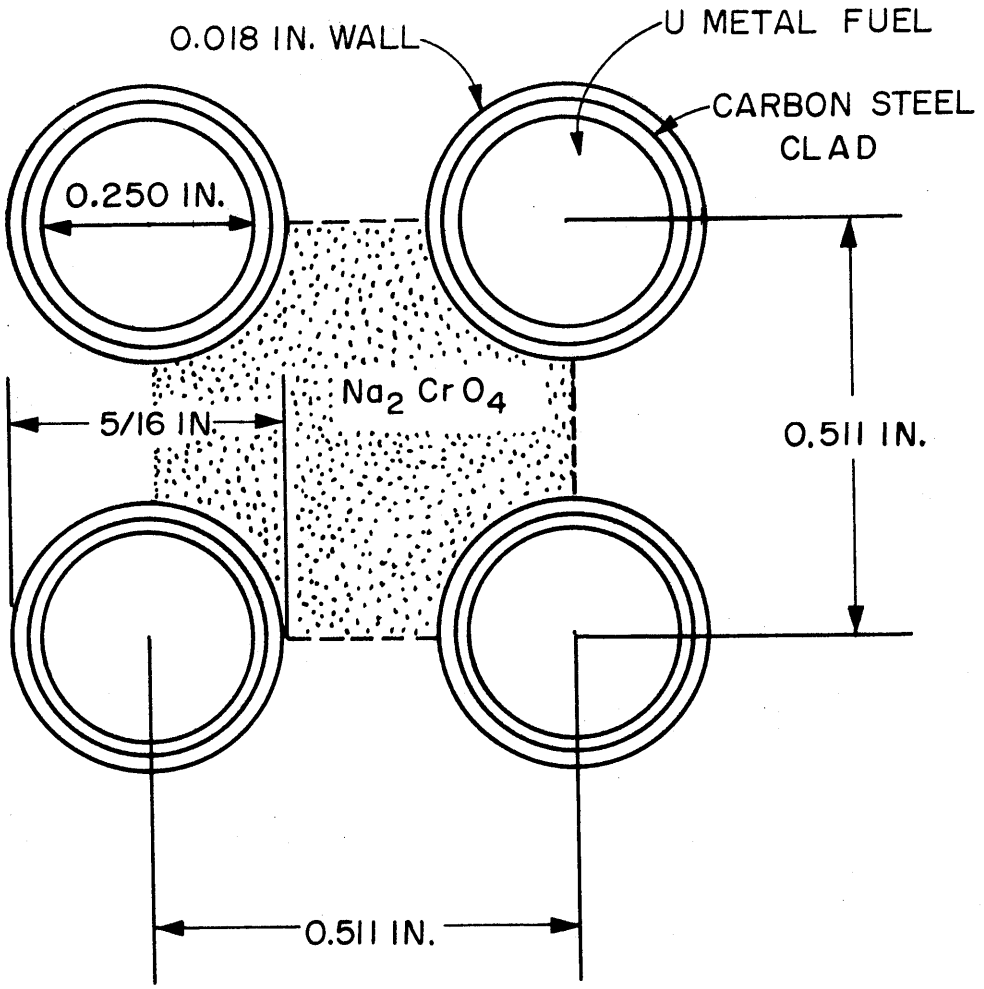

FIG. 4.4 BLANKET NO. 3 UNIT CELL

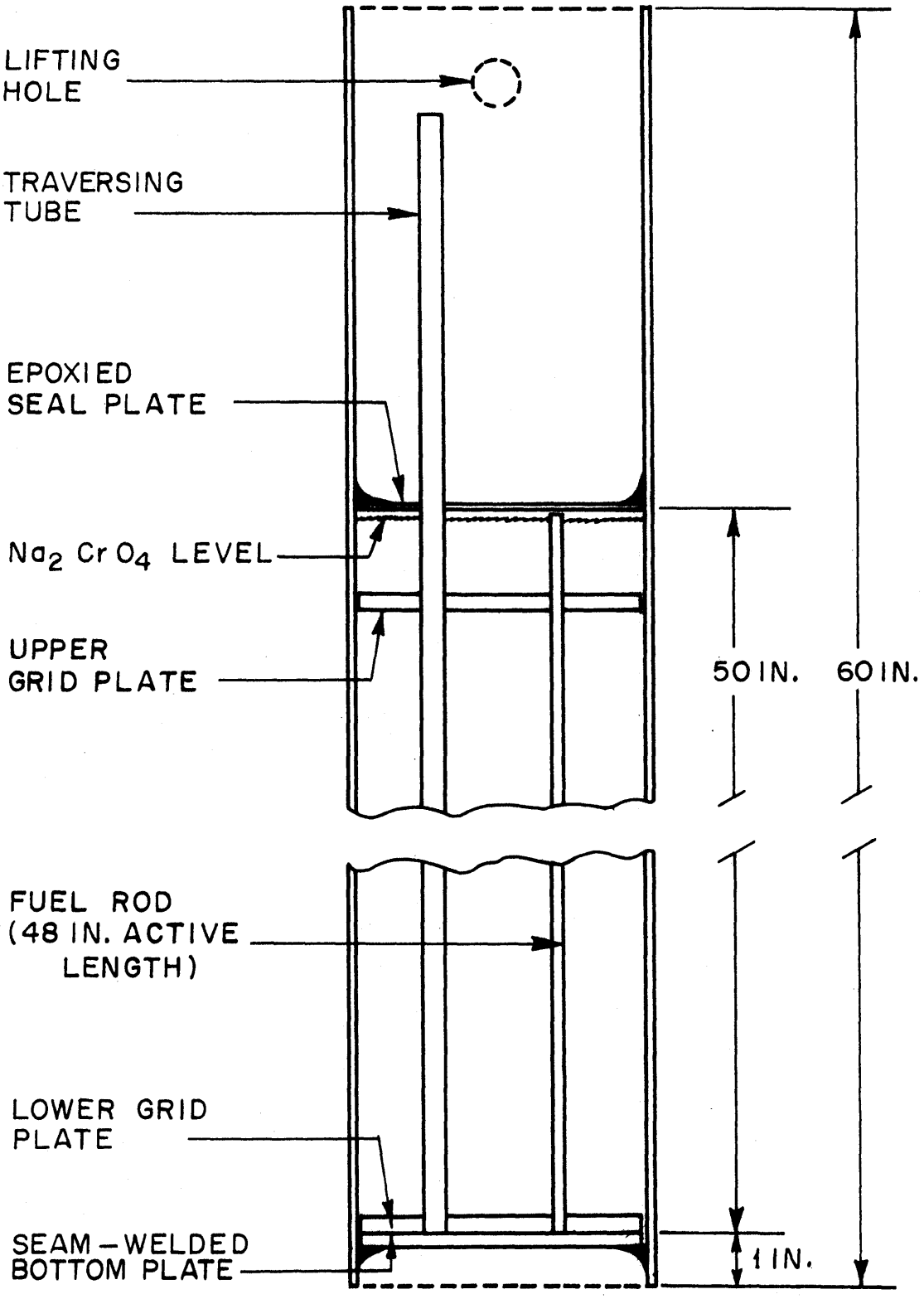

FIG. 4.5 SCHEMATIC CROSS SECTION VIEW OF BLANKET NO. 3 SUBASSEMBLY

The homogenized subassembly atom densities in Blanket No. 3 are given in Table 4.2. They represent the nuclide densities in the central portions of the assembly. Table 4.2 also includes the atom densities for an "equivalent realistic blanket" composed of 37 v/o depleted UO_2 (at 90% t. d.), 20.7 v/o Type 316 stainless steel (71.2 w/o Fe, 20.0 w/o Cr, 8.8 w/o Ni), 32 v/o sodium and 10.3 v/o void. Nuclide densities for the graphite and steel reflectors are also listed in Table 4.2. It is evident that Blanket No. 3 provides a realistic blanket composition.

TABLE 4.2

Homogenized Atom Densities in Blanket No. 3

(Atoms/barn-cm)

Nuclide	Blanket No. 3		Equivalent Realistic Blanket*	
U^{235}	0.000088		0.000016	
U^{238}	0.008108		0.008131	
O	0.016293		0.016293	
Na	0.008128		0.008128	
Cr	0.004064		0.003728	
Fe	0.013750	0.017814	0.012611	0.017814
Ni	0.000000		0.001475	
H	0.000073		0.000000	
C	0.000096		0.000082	
Nuclide	**Graphite Reflector**			
C	0.083245			
H	0.000298			
Nuclide	**Steel Reflector**			
C	0.000590			
Fe	0.084570			

* Composed of 37.0 v/o depleted UO_2 (at 90% of the theoretical density), 20.7 v/o Type 316 stainless steel, 32.0 v/o sodium and 10.3 v/o void.

4.2.3 Description of the Graphite Reflector

Figure 4.6 shows a schematic view of the graphite reflector assembly. It consists of a bottom graphite layer acting as the lower grid plate, the graphite reflector, and an aluminum top grid plate, forming a parallelepiped 52-1/4 inches high, 12 inches thick (i.e., two fuel subassemblies) and 60 inches wide. From a neutronic standpoint, 12 inches of graphite are effectively infinite in the present application.

The bottom grid plate was made from three 60-inch pieces of 4-inch-square graphite stringers placed side by side, forming a slab 4 inches by 12 inches by 60 inches.

These three stringers are held together by two aluminum rods which fit into 1/2-inch-diameter holes drilled through the stringers 15 inches from each end. The rods are threaded at each end and recess-bolted to clamp the grid plate together. Holes were then drilled into the top face of the plate to align the vertical stringers which make up the reflector. These holes are 1/4 inch in diameter and 3/4 inch deep and seat aluminum pins 1-1/2 inches long. The reflector consists of 48 graphite stringers 48 inches high. Four of the outside stringers are half pieces, 4 inches by 2 inches instead of 4 inches by 4 inches to permit formation of a staggered array. Also, the two stringers in the center of the assembly are half pieces, making 6 half stringers in all.

In each of these 48 stringers, 1/4-inch-diameter holes, 3/4-inch deep, were drilled in the top and bottom ends to fit over the aluminum pins set in the bottom grid plate, and to house pins which in turn align with the positioning holes in the top 1/4-inch-thick aluminum grid plate.

In order to permit foil activation traverses in the reflector assembly, twenty 3/8-inch-square vertical slots were milled into the faces of selected graphite stringers comprising the reflector. These slots house the holder rods for foil samples, as can be seen in Fig. 4.7. There are 6 slots which can be used to determine axial traverses and 14 slots for the transverse measurements.

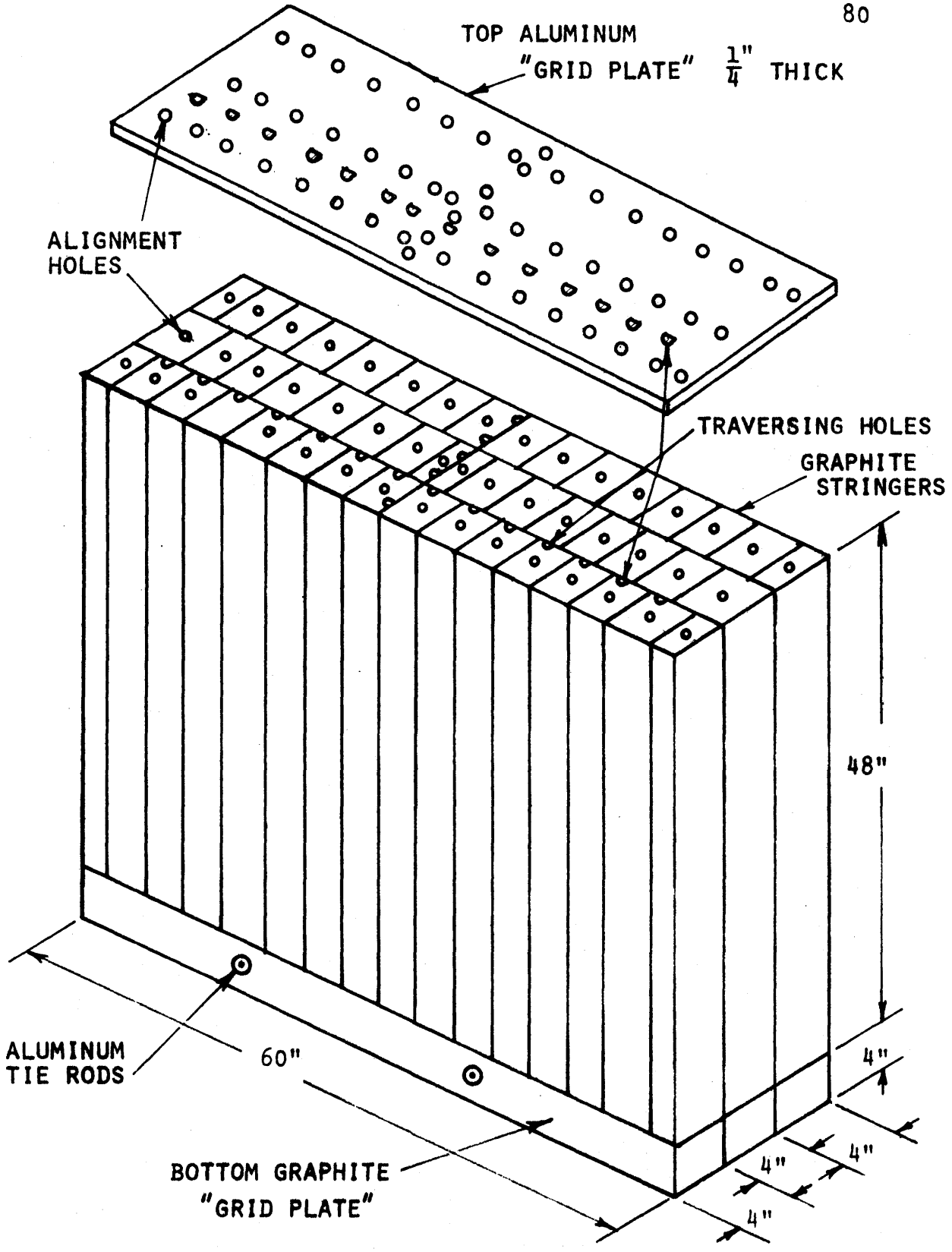

FIG. 4.6 SCHEMATIC VIEW OF GRAPHITE REFLECTOR ASSEMBLY

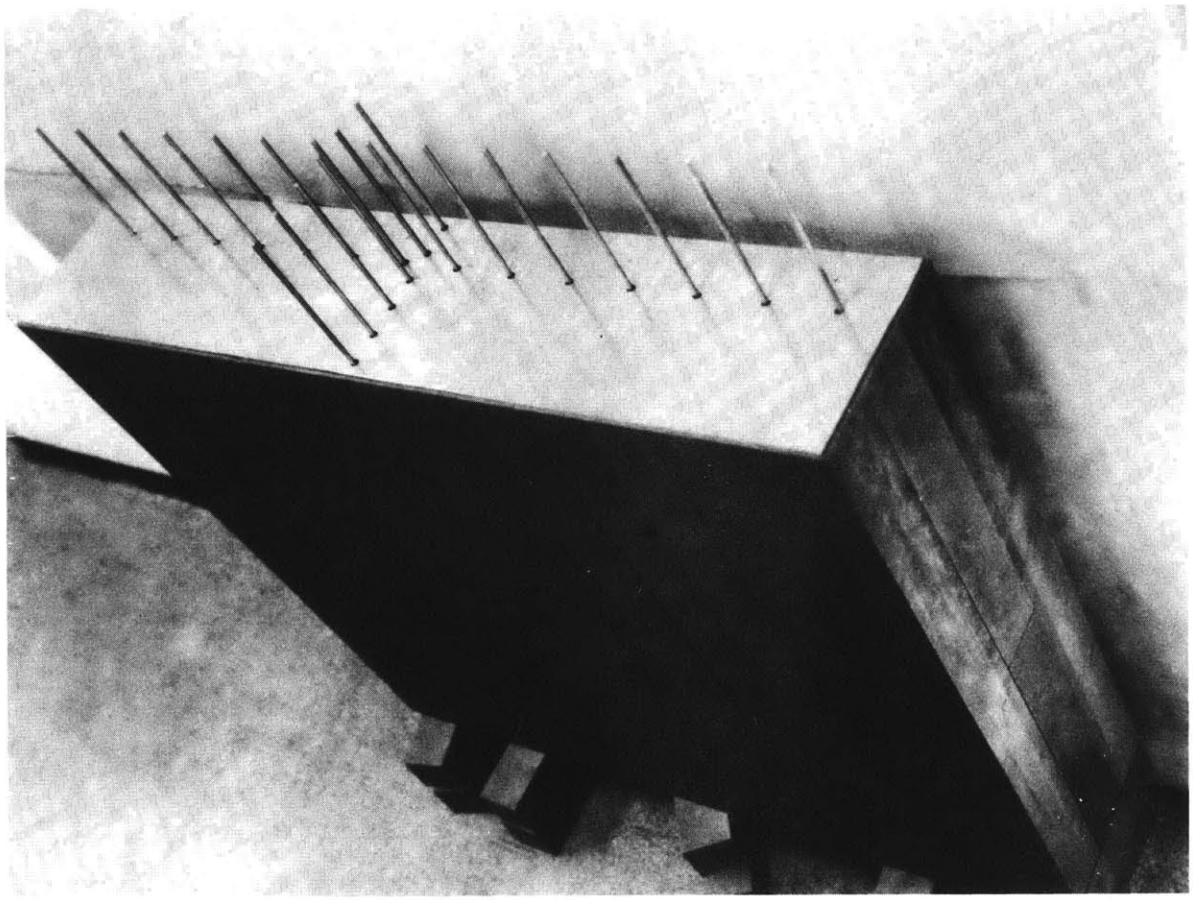

FIG. 4.7 GRAPHITE REFLECTOR WITH AXIAL AND TRANSVERSE HOLDER RODS INSERTED

In the experiments which follow, positions within the blanket and reflector are described in terms of a Cartesian coordinate system whose origin is at the center of the front face of the blanket (i.e., the converter-blanket interface): the ±X and ±Y axes delineate the horizontal and vertical directions, respectively, while the +Z axis (corresponding to the radial direction in a cylindrical core and blanket) designates the depth into the blanket (see Fig. 4.2).

4.3 Experimental Aspects

4.3.1 Introduction – Objectives

The objective of the present experiments was to obtain the necessary data to evaluate the transverse buckling and axial reaction rates for various foil materials in Blanket No. 3. The foil materials employed are listed in Table 4.3 along with the reactions of interest.

Buckling measurements in the X and Y directions are important because, in order to validate the one-dimensional calculational model, the leakage must be characterized by a buckling formulation. If this is the case, the neutron flux can be separated in space according to the relation:

$$\phi(X,Y,Z,E) = \cos\left(\frac{\pi X}{W}\right) \cos\left(\frac{\pi Y}{H}\right) \phi(Z,E) \qquad (4.1)$$

where the buckling is given by

$$B^2 = BX^2 + BY^2 = \left(\frac{\pi}{W}\right)^2 + \left(\frac{\pi}{H}\right)^2 \qquad (4.2)$$

and where W and H are experimentally determined values of the extrapolated width and height, respectively. The system was designed to achieve this result and the experiments on Blanket No. 2 have confirmed that this desired cosine dependence is attained (5). In the present work, therefore, less emphasis was placed on transverse buckling determinations than previously, and measurements were made just to confirm that the values of W and H in the graphite reflector are consistent with those previously determined in the blanket region of Blanket No. 2. The necessity for high precision in these measurements

has been further reduced by the observation that calculated Z traverses are not sensitive to the transverse buckling: even setting $B^2 = 0$ results in negligible changes in the calculated results.

4.3.2 Experimental Procedure

The experimental technique is rather conventional and practically identical to that used in the analysis of BTF No. 2 (5). Thus, only a brief description, primarily noting changes in the experimental procedure, will be presented.

4.3.2.1 Buckling Experiment

Transverse buckling measurements were made in the graphite reflector utilizing various foil materials. Gold, molybdenum and thorium foils were utilized for horizontal measurements. Gold and thorium foils were utilized in the vertical measurements. The thorium foils were used to detect fast neutrons by counting fission products produced in the threshold fission reaction. The experimental techniques were similar to those used in Blanket No. 2.

Aluminum rods containing milled axial depressions were used to position the foils vertically and, when inserted in the respective transverse traversing slots, provided the desired lateral positioning (see Fig. 4.7). Aluminum holders were used in the graphite instead of the standard steel holders employed for the blanket to avoid absorption of low-energy neutrons moderated by the graphite.

For vertical measurements, one rod holding 10 equispaced foils (3-inch spacing) was inserted in the central transverse slot. The horizontal measurements utilized all 14 slots (4-inch spacing) with foils held in place at locations along the midline (Y-axis) of the graphite.

The counting procedure used to obtain the raw data was identical to that used with BTF No. 2, as were foil weight, background and decay time corrections (where necessary) (5). The only procedural innovation involved the thorium foils, which were not used previously. In order to achieve useful counting statistics, a sandwich arrangement

of three aluminum fission product catcher foils and two thorium foils held together with Mylar tape was used (Fig. 4.8). By counting the fission products recoiled into the catcher foils, instead of those in the thorium metal itself, the high thorium background activity did not compromise the fission product counting.

4.3.2.2 Axial Traverses

Axial traverses were made in the blanket and graphite reflector assemblies. Simulating traverses in the radial direction in cylindrical geometry, twelve axial traversing slots are provided, six each in the blanket and graphite. Steel foil-holder rods were used in the blanket region and aluminum rods were used in the graphite region. The foils irradiated in this phase of the experiment are listed in Table 4.3. Along with thorium, which was discussed in section 4.3.2.1, neptunium and manganese represent the only foil materials not irradiated previously in Blanket No. 2.

The manganese, in powder form, was encapsulated in poly vials in a manner similar to that used for the sodium foils. The neptunium compound, a nitrate of undetermined composition, was loaded in 1/4-inch-diameter by 1-inch-long aluminum capsules and taped to the foil-holder rods. The relative neptunium content of the individual capsules was determined by background activity measurements.

The counting procedure used to obtain the raw data was identical to that used in Blanket No. 2, as were corrections for foil weights, background and decay time. The only additional modification involved determination of the relative weights of the plutonium samples, where background activity was used to determine the relative plutonium content instead of direct weighing or thermal activation calibration.

Table 4.4. summarizes the counting characteristics of the thorium, neptunium and manganese foils used in the reaction rate measurements. Similar data for the other foil materials are found in reference (5).

FIG. 4.8 THORIUM FOIL PACKET

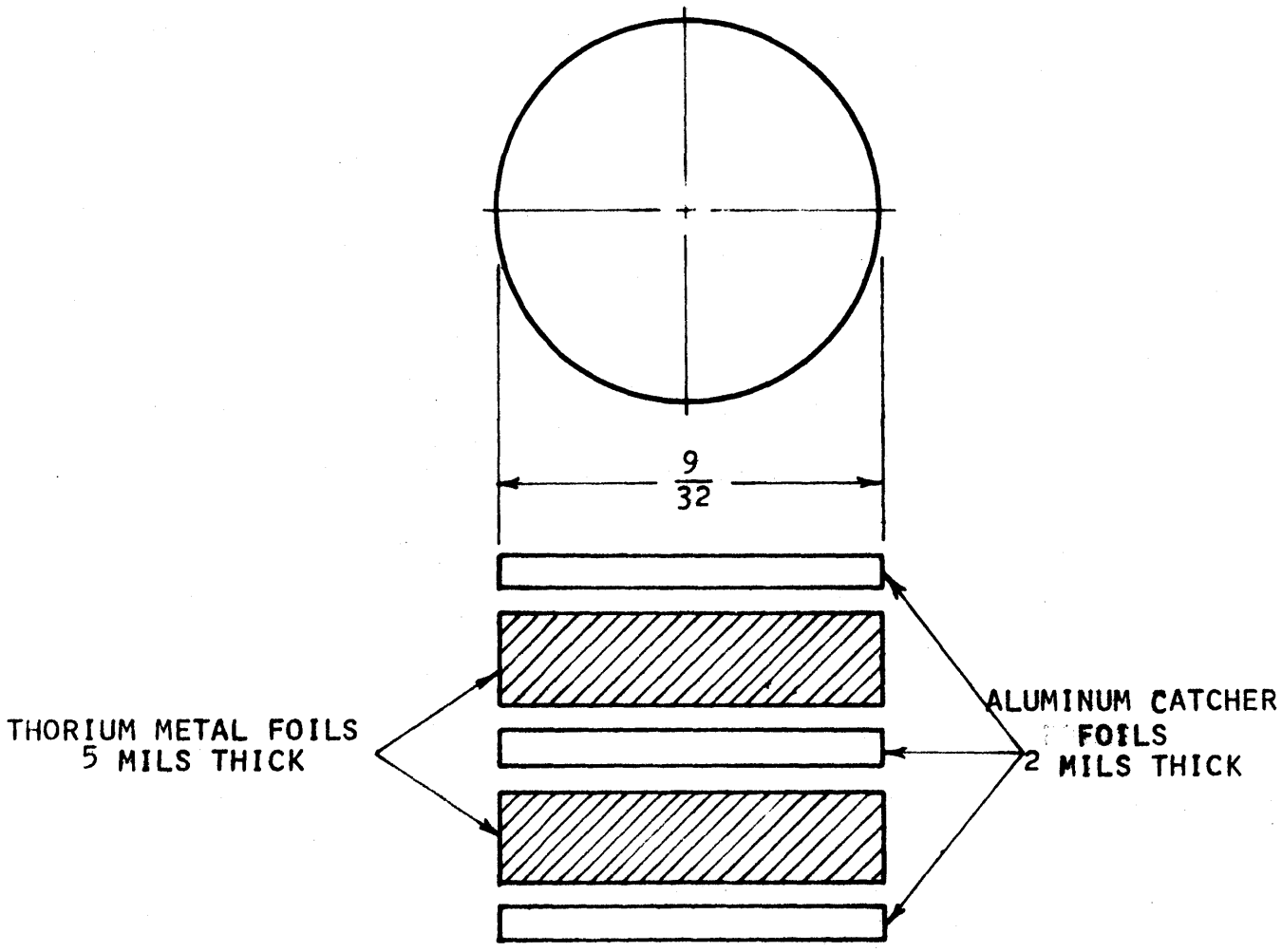

TABLE 4.3

Activation Foils Used in BTF No. 3

Foil	Reaction	Remarks
Gold	$Au^{197}(n,\gamma)Au^{198}$	Measures entire energy spectrum (A,B)*
Molybdenum	$Mo^{98}(n,\gamma)Mo^{99}$	Emphasizes keV range (A,B)
Indium	$In^{115}(n,n')\,In^{115m}$	Threshold reaction E > 0.2 MeV (A,B)
Manganese†	$Mn^{55}(n,\gamma)Mn^{56}$	Emphasizes keV range (A)
Sodium	$Na^{23}(n,\gamma)Na^{24}$	Typical LMFBR material (A)
Chromium	$Cr^{50}(n,\gamma)Cr^{51}$	Typical LMFBR material (A)
Uranium	—	Typical LMFBR material
-238 in-rod	$U^{238}(n,\gamma)$	(A)
-238 ex-rod	$U^{238}(n,\gamma)$	(A,B)
-238 in-rod	$U^{238}(n,f)$	Threshold reaction E > 1.0 MeV (A)
-238 ex-rod	$U^{238}(n,f)$	(A,B)
-235	$U^{235}(n,f)$	(A)
Plutonium-239	$Pu^{239}(n,f)$	Typical LMFBR material (A)
Thorium†	$Th^{232}(n,f)$	Threshold reaction E > 1.75 MeV (A,B)
Neptunium†	$Np^{237}(n,f)$	Threshold reaction E > 0.75 MeV (A)

* A indicates foil used for axial activation traverse.
B indicates foil used for transverse activation traverse (i.e., buckling determination).

† New materials, not used in BTF No. 2.

TABLE 4.4

Typical Data Pertinent to Foil Counting

Parameter	Thorium Foil	Neptunium Foil	Manganese Foil
Reaction	$Th^{232}(n,f)$	$Np^{237}(n,f)$	$Mn^{55}(n,\gamma)$
Product nuclide	Fission products	Fission products	Mn^{56}
Half life	~2.5 hours	~2.5 hours	2.58 hours
Eγ (MeV)	⩾ 0.5	⩾ 0.5	0.84
Eγ detected (MeV)	0.72-∞	1.28-∞	0.72-∞
Discriminator setting			
E_{min} (volts)	1.54*	2.80*	1.90†
E_{max} (volts)	∞	∞	∞
Typical counts (less bkg.)	500	2,000	30,000
Counting time (minutes)	10	5	2
Irradiation time (hours)	12	12	16

* Calibration approximately 0.46 MeV per volt

† Calibration approximately 0.38 MeV per volt

4.4 The Results

4.4.1 Analytical Predictions

4.4.1.1 Buckling

As previously mentioned, the transverse fluxes in Blanket No. 2 were found to follow the anticipated cosine shape. Hence, the buckling in Blanket No. 3 should also conform to this result:

$$A(X) = A(o)\cos\left(\frac{\pi X}{W}\right)$$

and (4.3)

$$A(Y) = A(o)\cos\left(\frac{\pi Y}{H}\right)$$

where the extrapolated width and height, W and H, are best determined by curve-fitting the experimental data, and A(o) is the maximum amplitude. The values of W and H obtained in Blanket No. 2 were 74 inches and 60 inches, respectively; the corresponding assembly width and active fuel height are 58 inches and 48 inches. No significant change is to be expected for Blanket No. 3, since the graphite was sized to have approximately the same theoretical extrapolated peripheral dimensions as the rest of the assembly, which is otherwise identical to Blanket No. 2 in the X and Y directions.

4.4.1.2 Axial Traverses

Axial reaction rates were computed by means of the one-dimensional transport theory code, ANISN (7) in the S_8 option, using the 26-group Russian ABBN cross-section set (9) for all but four materials. The effect of U^{238} self-shielding in the converter plate and blanket fuel rods has been taken into account. Broad group cross sections for U^{238}, which account for resonance self-shielding, have been generated with the MIDI code (3). These cross sections were then incorporated into the 26-group ABBN set.

Au^{197} capture, $In^{115}(n,n')$ and Np^{237} fission cross-section data were developed from the SAND-II Library (9) by collapsing over the ABBN weighting spectrum. It should be noted that the cross-section data used to evaluate the foil activities were not self-shielded, except

for in-rod U^{238} capture; i.e., the calculated ex-rod U^{238} reaction rate is for infinite dilution cross sections.

Plots of these data are found in the figures referred to in the next section, where they are compared to the experimental results.

4.4.2 Experimental Results

The data reported in this section are normalized activities corrected for counter dead time, background activity, foil weight, and sample decay time. To facilitate comparison, the experimental data were normalized to coincide with the calculated results at a convenient point. Thus, for example, the experimental axial results were made to coincide with the calculated results at approximately 12.7 centimeters from the converter-blanket interface which is a little less than half way into the blanket. The only exception occurs in Fig. 4.16, where the correct experimental ratio between in-rod and ex-rod U^{238} captures is maintained.

Error brackets are shown on the graphs when the experimental point itself is not large enough to cover the experimental error. Typically, over 10,000 counts were accumulated to ensure statistical precision of better than ± 1%. At deep penetrations and where background activity was a substantial portion of the counts, ± 1%, statistical error in the relative activity was sometimes exceeded. The errors shown in Tables 4.5 and 4.6 and 4.7 show either the uncertainty in counting statistics or the experimental standard deviation corrected for small sample statistics, whichever is applicable. A more detailed discussion of experimental error is included in section 4.4.3.

4.4.2.1 Buckling

Tables 4.5 and 4.6 show the normalized vertical and horizontal buckling traverse data as a function of distance from the origin of coordinates. Figures 4.9 and 4.10 show representative plots of these data for the Au, Mo and Th horizontal and Au and Th vertical data, respectively. The cosine distributions conform to Eq. 4.1 with W = 74 inches and H = 60 inches, the Blanket No. 2 values.

TABLE 4.5

Activation Traverses for Vertical Buckling Determination

Foil Position	Distance from ℄ (inches)	Normalized Data Au (n,γ)	Normalized Data Th (n,f)
1	-21	0.419 ± 0.001*	0.466 ± 0.087*
2	-18	0.546 ± 0.001	0.556 ± 0.081
3	-15		0.671 ± 0.083
4	-12	0.787 ± 0.001	0.765 ± 0.086
5	-9	0.881 ± 0.001	0.901 ± 0.084
6	-6	0.950 ± 0.001	0.830 ± 0.082
7	-3	0.988 ± 0.001	0.792 ± 0.089
8	0	1.000 ± 0.001	1.000 ± 0.087
9	3	0.994 ± 0.001	0.971 ± 0.089
10	6	0.952 ± 0.001	0.405 ± 0.087
11	9	0.896 ± 0.001	0.970 ± 0.085
12	12	0.839 ± 0.001	0.887 ± 0.087
13	15	0.740 ± 0.001	0.752 ± 0.086
14	18	0.621 ± 0.001	0.647 ± 0.087
15	21	0.472 ± 0.001	0.515 ± 0.086

* Statistical error.
See section 4.4.3 for discussion of errors.

TABLE 4.6

Activation Traverses for Horizontal Buckling Determination

Foil Position	Distance from ℄ (inches)	Normalized Data Au (n,γ)	Normalized Data Mo (n,γ)	Normalized Data Th (n,γ)
1	-26	0.400 ± 0.001*	0.403 ± 0.028*	
2	-22	0.574 ± 0.001	0.554 ± 0.028	0.711 ± 0.109*
3	-18	0.730 ± 0.001	0.706 ± 0.035	1.132 ± 0.113
4	-14	0.838 ± 0.001	0.855 ± 0.034	1.209 ± 0.118
5	-10	0.934 ± 0.001	0.908 ± 0.036	1.468 ± 0.113
6	-6	0.991 ± 0.001	0.912 ± 0.036	1.294 ± 0.112
7	-2	0.999 ± 0.001	1.000 ± 0.040	1.450 ± 0.121
8	2	1.000 ± 0.001	0.925 ± 0.037	1.500 ± 0.118
9	6	0.986 ± 0.001	1.139 ± 0.044	1.337 ± 0.121
10	10	0.938 ± 0.001	0.917 ± 0.037	1.290 ± 0.120
11	14	0.856 ± 0.001	0.779 ± 0.031	1.115 ± 0.115
12	18	0.718 ± 0.001	0.744 ± 0.031	1.183 ± 0.117
13	22	0.559 ± 0.001	0.612 ± 0.035	0.910 ± 0.115
14	26	0.364 ± 0.001	0.436 ± 0.026	

* Statistical error.
See section 4.4.3 for discussion of errors.

FIG. 4.9 HORIZONTAL ACTIVATION TRAVERSES IN BLANKET NO. 3

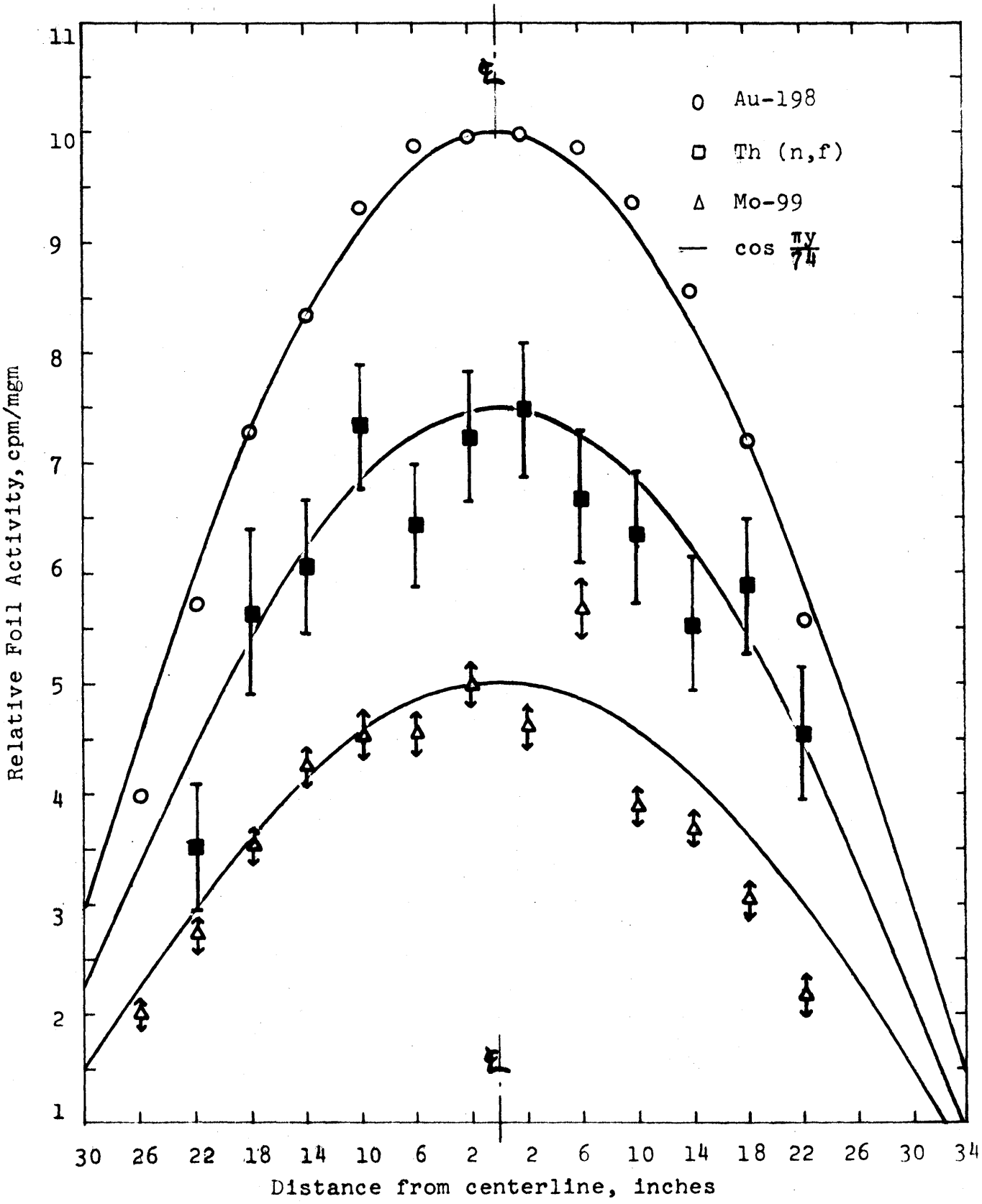

FIG. 4.10 VERTICAL ACTIVATION TRAVERSES IN BLANKET NO. 3

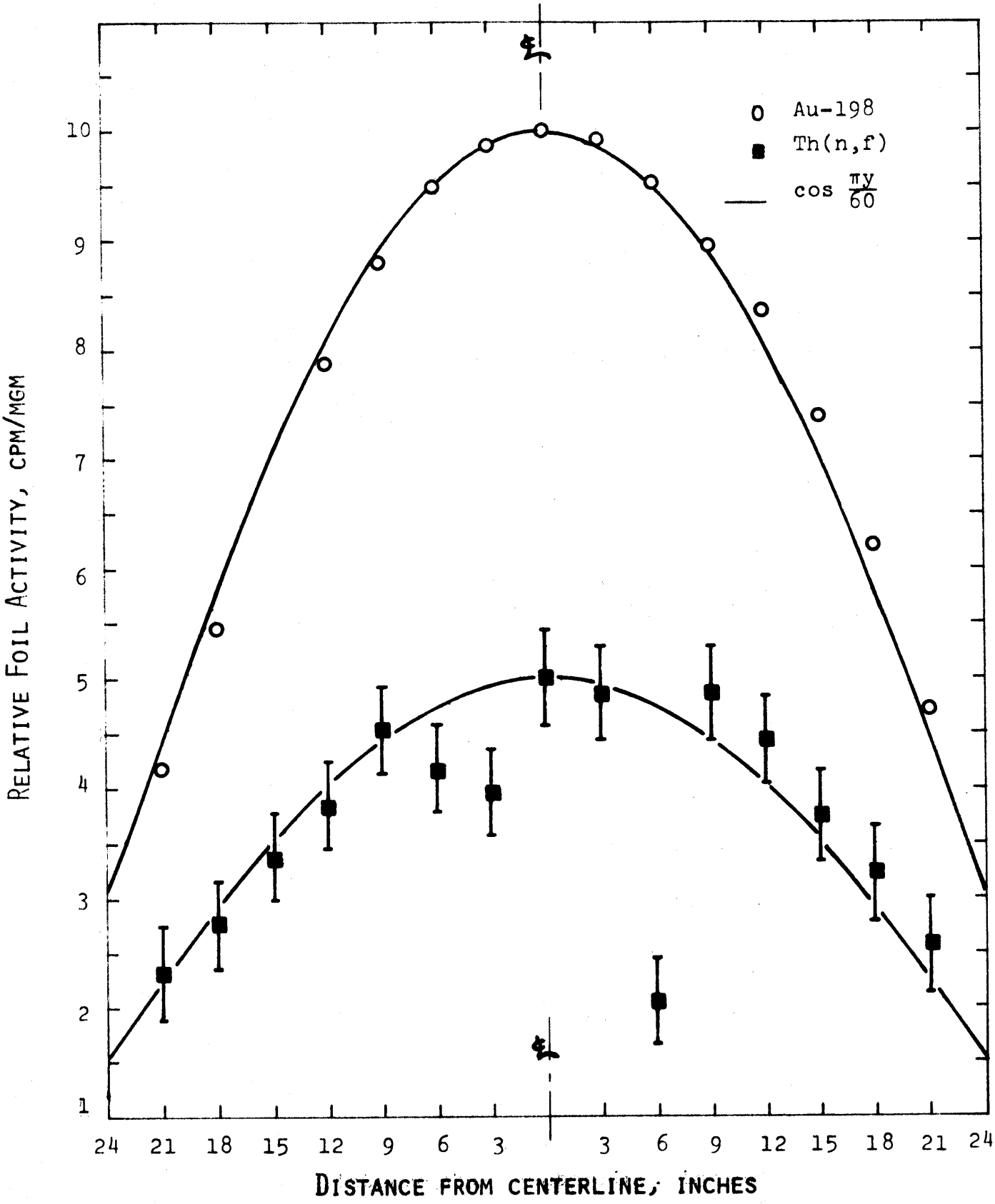

To ensure that spectral equilibrium is achieved in the central region of the graphite, the ratio of U^{238} to gold captures was plotted in Fig. 4.11. The flat region, approximately 16 inches wide, confirms the result found in Blanket No. 2 and ensures that the central reflector region has achieved spectral equilibrium.

4.4.2.2 Axial Activation Traverses

Table 4.7 lists the normalized data for the axial traverses of the various foils as a function of the distance from the converter-blanket interface. Figures 4.12 through 4.25 show these data plotted on the same graph as the numerical predictions. For the sake of comparison, it is found convenient to normalize both the experimental and calculated results to the same value at approximately the midpoint of the blanket, i.e., at 12.7 cm from the converter.

These results are discussed further in section 4.4.4.

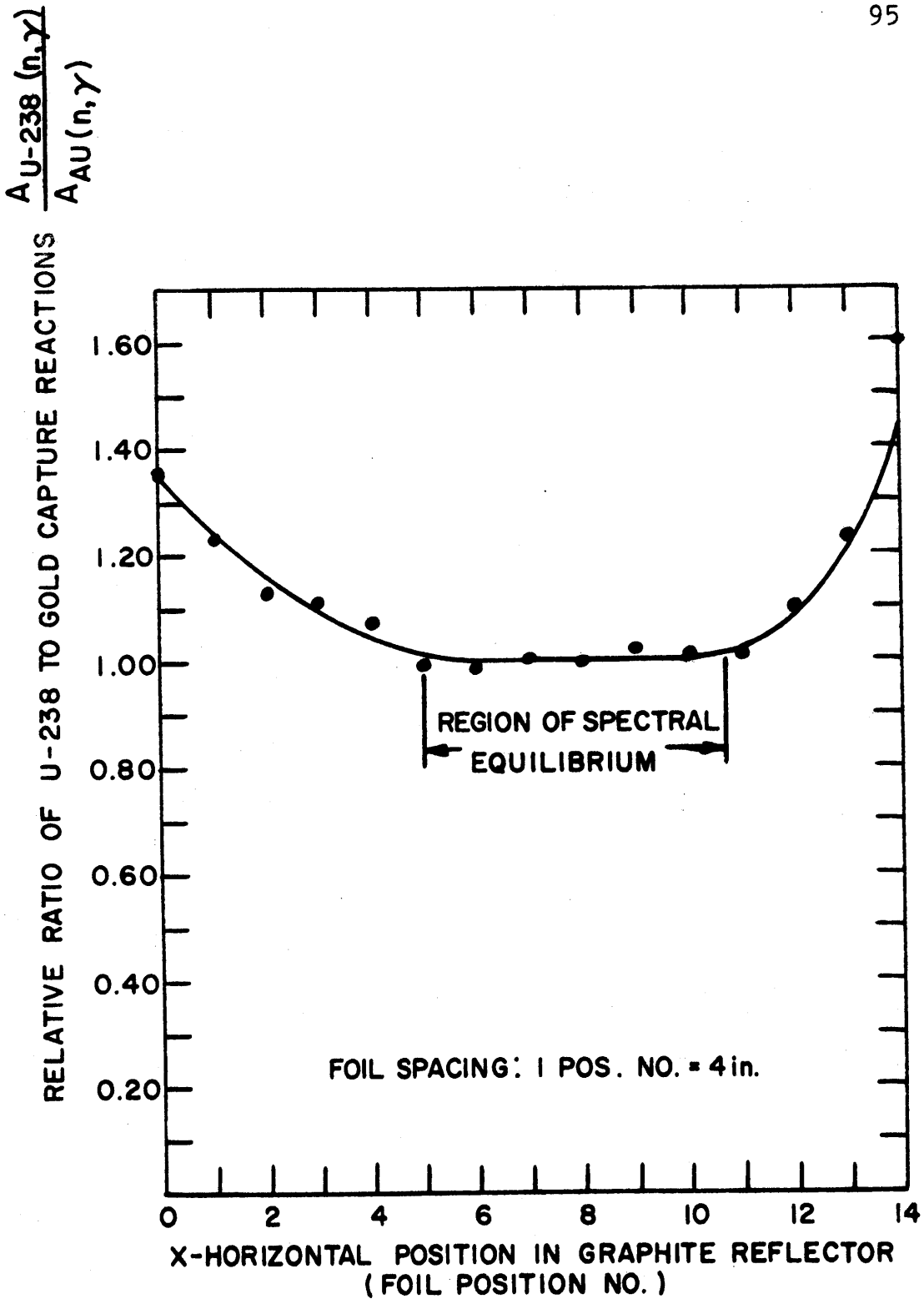

FIG. 4.11 SPECTRAL INDEX TRAVERSE IN GRAPHITE REFLECTOR OF MOCKUP NO. 3

TABLE 4.7. Normalized Axial Reaction Rate Data

Distance Into Blanket (cm)	Au (n,γ)	Au (n,γ), Dilute	In (n,n')	Mo (n,γ)
2.34	0.1798 ± 0.0105*	0.1617 ± 0.0062*	13.10 ± 0.300*	3.088 ± 0.025*
2.50	0.1624 ± 0.0079	0.1515 ± 0.0130	9.254 ± 0.015	2.764 ± 0.033
12.70	0.1475 ± 0.0000	0.1475 ± 0.0000	6.748 ± 0.004	2.500 ± 0.047
17.40	0.1439 ± 0.0021	0.1634 ± 0.0212	5.280 ± 0.360	2.118 ± 0.010
22.60	0.1663 ± 0.0102	0.2364 ± 0.0045	4.487 ± 0.227	1.856 ± 0.014
27.80	0.2501 ± 0.0076	0.4359 ± 0.0130	4.073 ± 0.210	1.755 ± 0.018
32.87	0.6423 ± 0.0443	1.1786 ± 0.1397	3.096 ± 0.273	1.917 ± 0.000
37.95	0.8941 ± 0.0512	1.4690 ± 0.0590	2.391 ± 0.358	1.707 ± 0.038
43.03	0.9692 ± 0.0588	1.5777 ± 0.0961	2.089 ± 0.208	1.367 ± 0.031
48.11	0.8993 ± 0.0427	1.2353 ± 0.0630	1.674 ± 0.283	1.004 ± 0.016
53.19	0.7278 ± 0.0455	1.0117 ± 0.2322	1.432 ± 0.255	0.6871 ± 0.0051
58.27	0.4923 ± 0.0324	0.7577 ± 0.0893	1.201 ± 0.330	0.4365 ± 0.0027

(Continued)

TABLE 4.7. Normalized Axial Reaction Rate Data (continued)

Distance Into Blanket (cm)	Mn (n,γ)	Na (n,γ)	Cr (n,γ)	U^{238} (n,f)
2.34	2.255 ± < 0.01*	2.968 ± 0.034*	1.115 ± 0.079*	16.12 ± 0.73*
2.50	2.123 ± < 0.01	2.475 ± 0.103	0.977 ± 0.048	11.83 ± 0.55
12.70	1.950 ± < 0.01	2.205 ± 0.000	0.894 ± 0.053	9.350 ± 0.000
17.40	2.528 ± < 0.01	2.190 ± 0.085	0.938 ± 0.037	7.511 ± 0.410
22.60	2.065 ± < 0.01	2.789 ± 0.139	1.262 ± 0.017	6.969 ± 0.794
27.80	3.334 ± < 0.01	5.249 ± 0.159	2.504 ± 0.137	6.295 ± 0.051
32.87	8.467 ± < 0.01	15.98 ± 0.63	7.937 ± 0.000	5.112 ± 0.967
37.95	12.302 ± < 0.01	23.96 ± 1.27	11.89 ± 0.565	4.576 ± 0.382
43.03	13.847 ± < 0.01	27.36 ± 0.89	13.63 ± 0.731	4.349 ± 1.069
48.11	13.250 ± < 0.01	26.58 ± 1.20	13.25 ± 0.741	4.112 ± 1.215
53.19	10.574 ± < 0.01	21.60 ± 0.82	10.93 ± 0.584	3.875 ± 1.078
58.27	6.859 ± < 0.01	13.57 ± 0.34	6.889 ± 0.479	3.606 ± 0.930

(Continued)

TABLE 4.7. Normalized Axial Reaction Rate Data (Continued)

Distance Into Blanket (cm)	U^{238} (n,γ) Ex-Rod	U^{235} (n,f)	Th (n,f)	Np (n,f)
2.34	10.10 ± 0.48*	2.719 ± 0.029*	10.41 ± 0.10†	9.138 ± 0.147†
2.50	8.71 ± 0.35	2.477 ± 0.056	6.417 ± 0.094	7.420 ± 0.142
12.70	8.10 ± 0.00	2.208 ± 0.000	4.544 ± 0.092	5.500 ± 0.145
17.40	7.50 ± 0.39	2.194 ± 0.069	3.624 ± 0.093	4.367 ± 0.114
22.60	7.26 ± 0.73	2.533 ± 0.223	2.931 ± 0.092	4.383 ± 0.116
27.80	8.46 ± 0.44	4.676 ± 0.146	2.687 ± 0.092	4.746 ± 0.114
32.87	18.83 ± 0.35	15.90 ± 0.45	1.671 ± 0.091	7.134 ± 0.146
37.95	20.74 ± 0.17	25.47 ± 1.10	0.864 ± 0.090	11.985 ± 0.157
43.03	19.40 ± 1.72	29.62 ± 0.54	0.579 ± 0.090	11.501 ± 0.164
48.11	15.59 ± 0.88	28.71 ± 0.83	0.128 ± 0.090	10.675 ± 0.152
53.19	11.38 ± 0.96	23.81 ± 0.66	0.246 ± 0.090	7.772 ± 0.136
58.27	7.85 ± 0.70	14.70 ± 0.55	0.149 ± 0.090	4.417 ± 0.111

(Continued)

TABLE 4.7. Normalized Axial Reaction Rate Data (Concluded)

Distance Into Blanket (cm)	U^{238} (n,γ) In-Rod	U^{238} (n,γ) Ex-Rod‡	U^{238} (n,f) In-Rod	Pu (n,f)
2.34	3.052 ± 0.034*	3.30 ± 0.16*	16.02 ± 0.50	2.81 ± 0.42*
2.50	2.618 ± 0.010	2.85 ± 0.11	11.45 ± 0.81	2.34 ± 0.19
12.70	2.230 ± 0.020	2.65 ± 0.00	9.25 ± 0.00	2.10 ± 0.00
17.40	1.920 ± 0.069	2.45 ± 0.13	8.02 ± 0.09	1.93 ± 0.12
22.60	1.690 ± 0.010	2.37 ± 0.24	7.11 ± 0.53	2.22 ± 0.12
27.80	1.818 ± 0.056	2.77 ± 0.14	6.88 ± 1.49	3.36 ± 0.11
32.87				10.00 ± 1.29
37.95				13.78 ± 1.73
43.03				15.24 ± 4.56
48.11				16.12 ± 1.01
53.19				12.13 ± 1.74
58.27				7.34 ± 0.24

* This standard deviation includes Student's t-Factor. See section 4.4.3.

† Statistical error only. See section 4.4.3.

‡ Normalized to U^{238} (n,γ) in-rod experimental data.

FIG. 4.12 GOLD (n,γ) AXIAL TRAVERSE

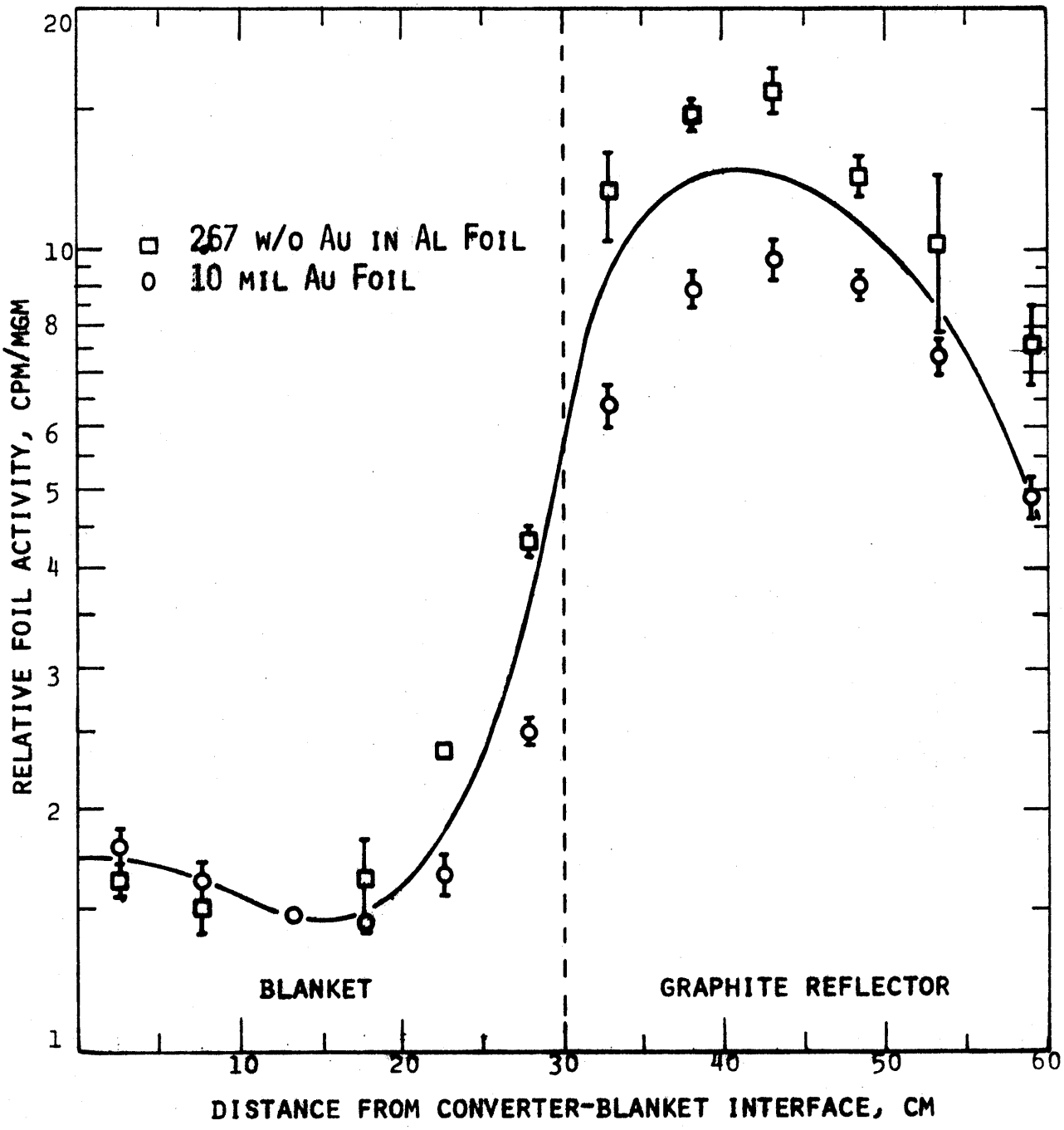

FIG. 4.13 SODIUM (n,γ) AXIAL TRAVERSE

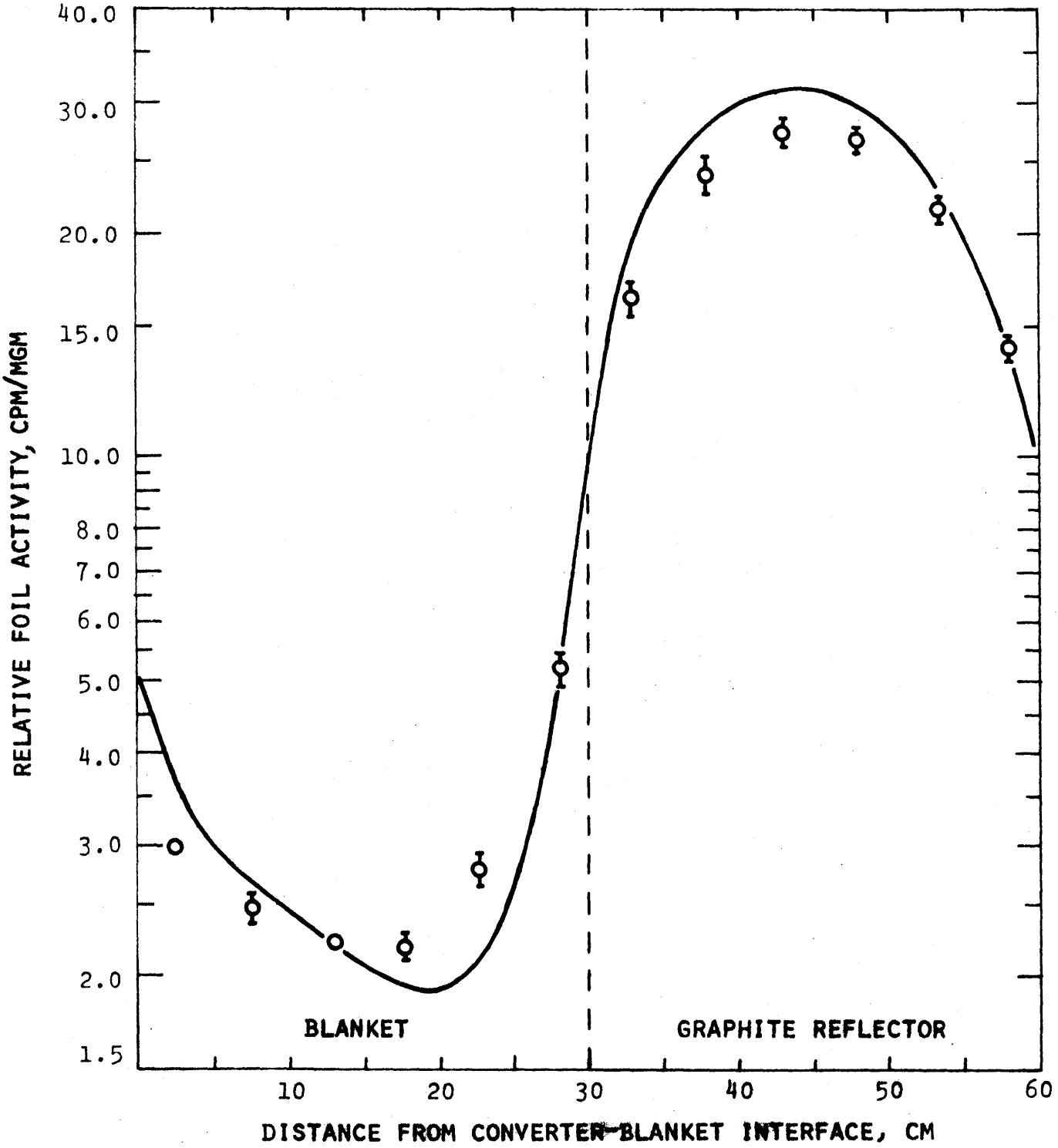

FIG. 4.14 CHROMIUM (n,γ) AXIAL TRAVERSE

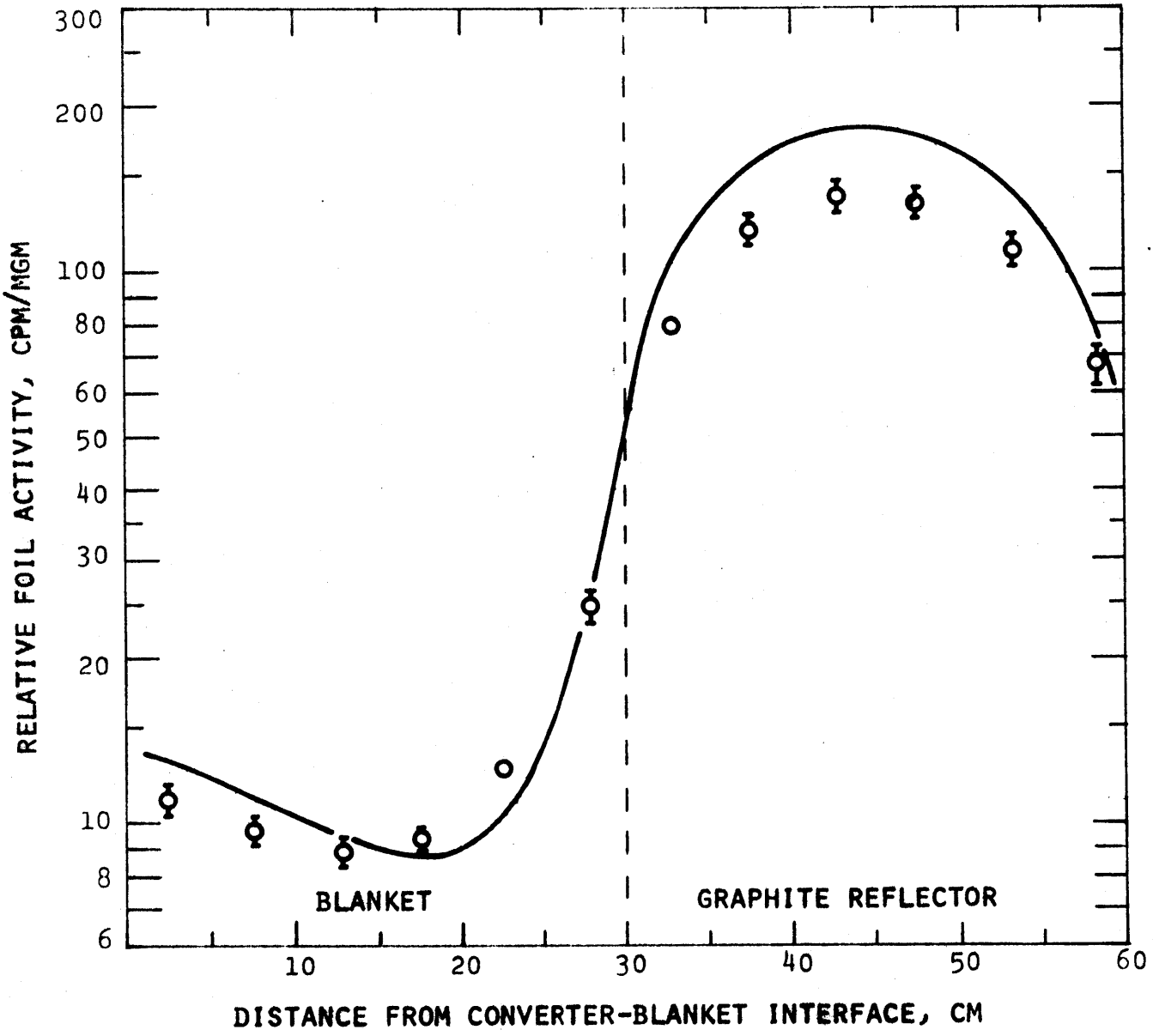

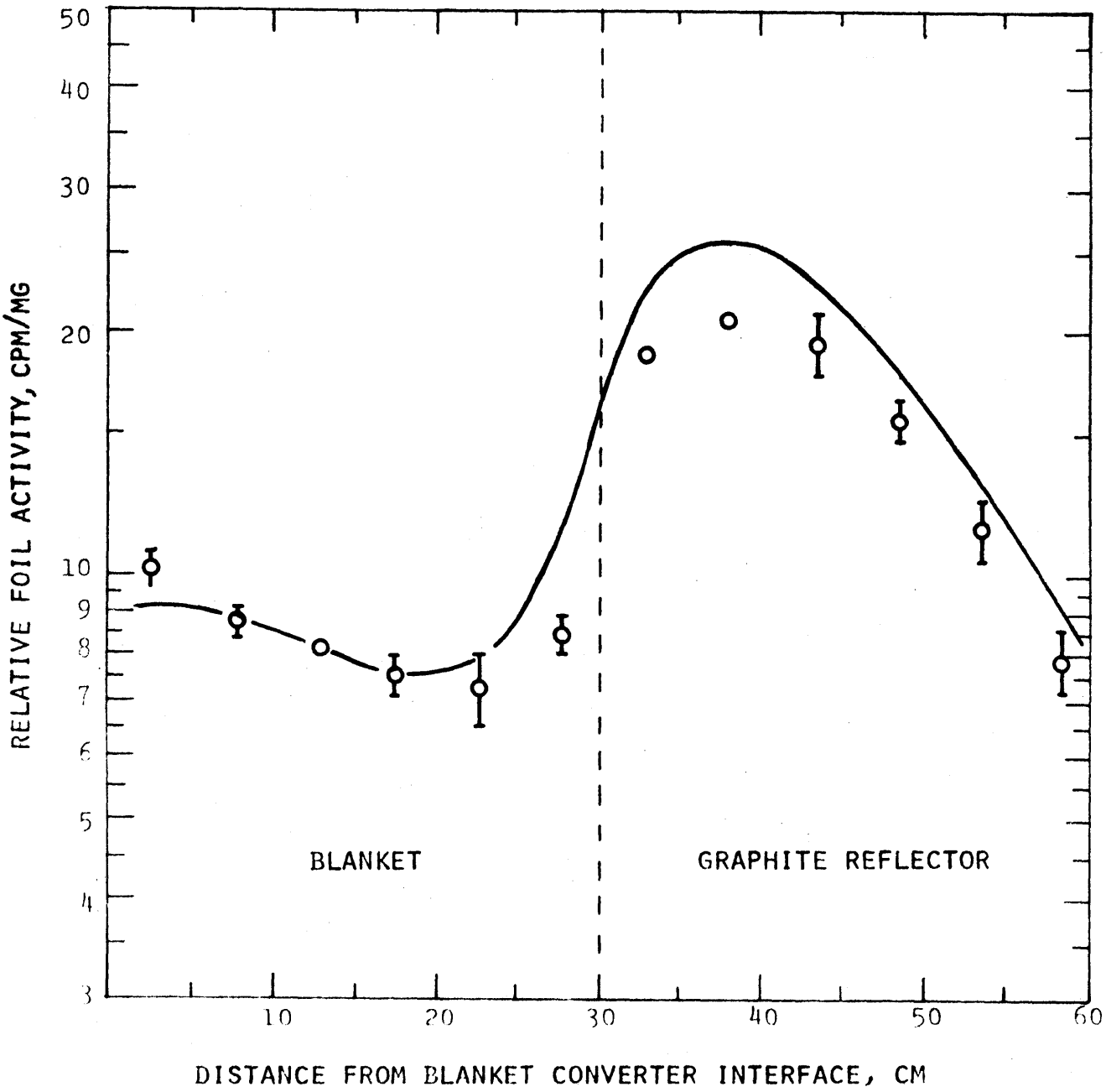

FIG. 4.15 EX-ROD U-238 (n,γ) AXIAL TRAVERSE

FIG. 4.16 U-238 (n,γ) AXIAL TRAVERSE IN BLANKET

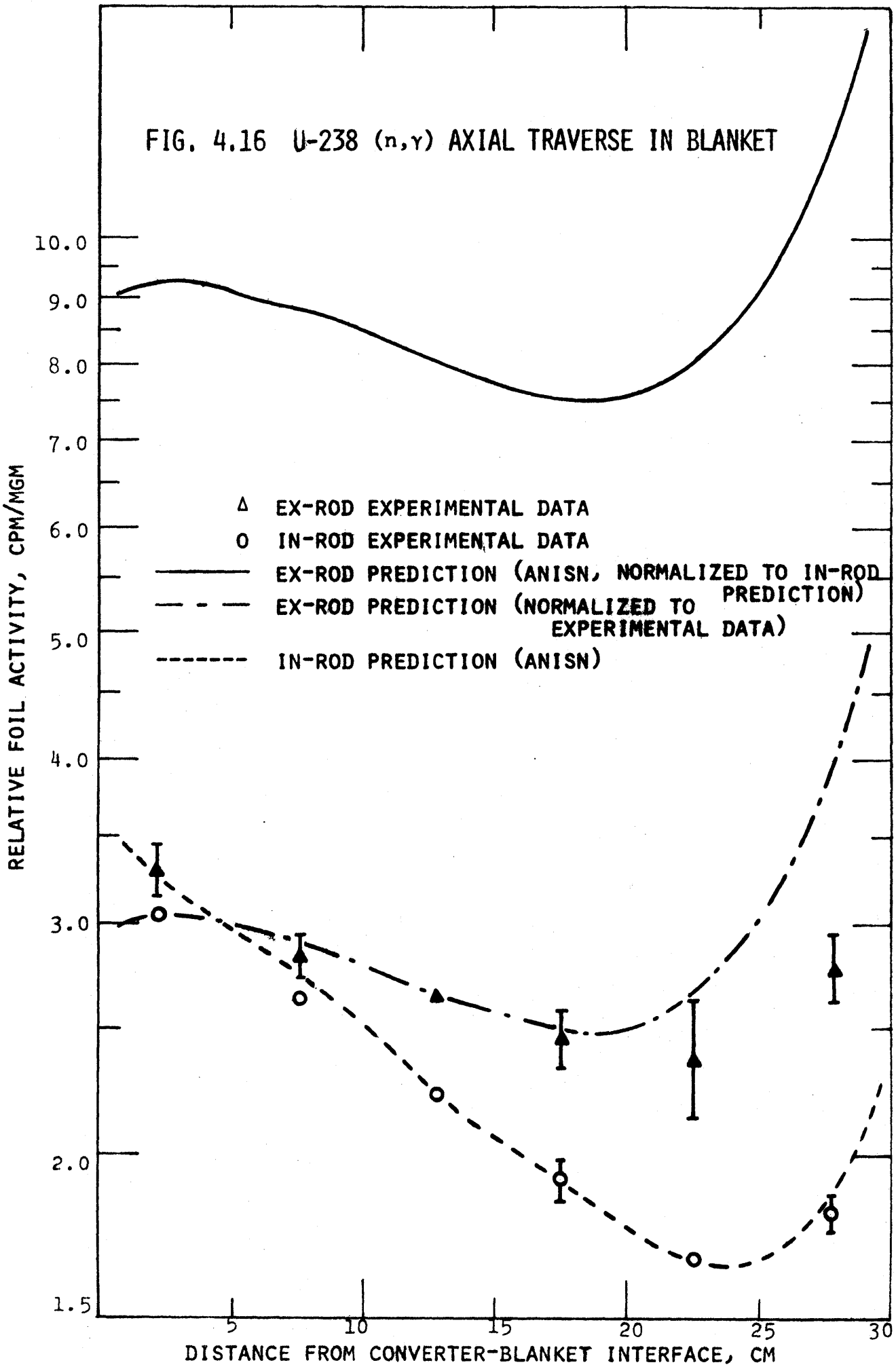

FIG. 4.17 U-235 (n,f) AXIAL TRAVERSE

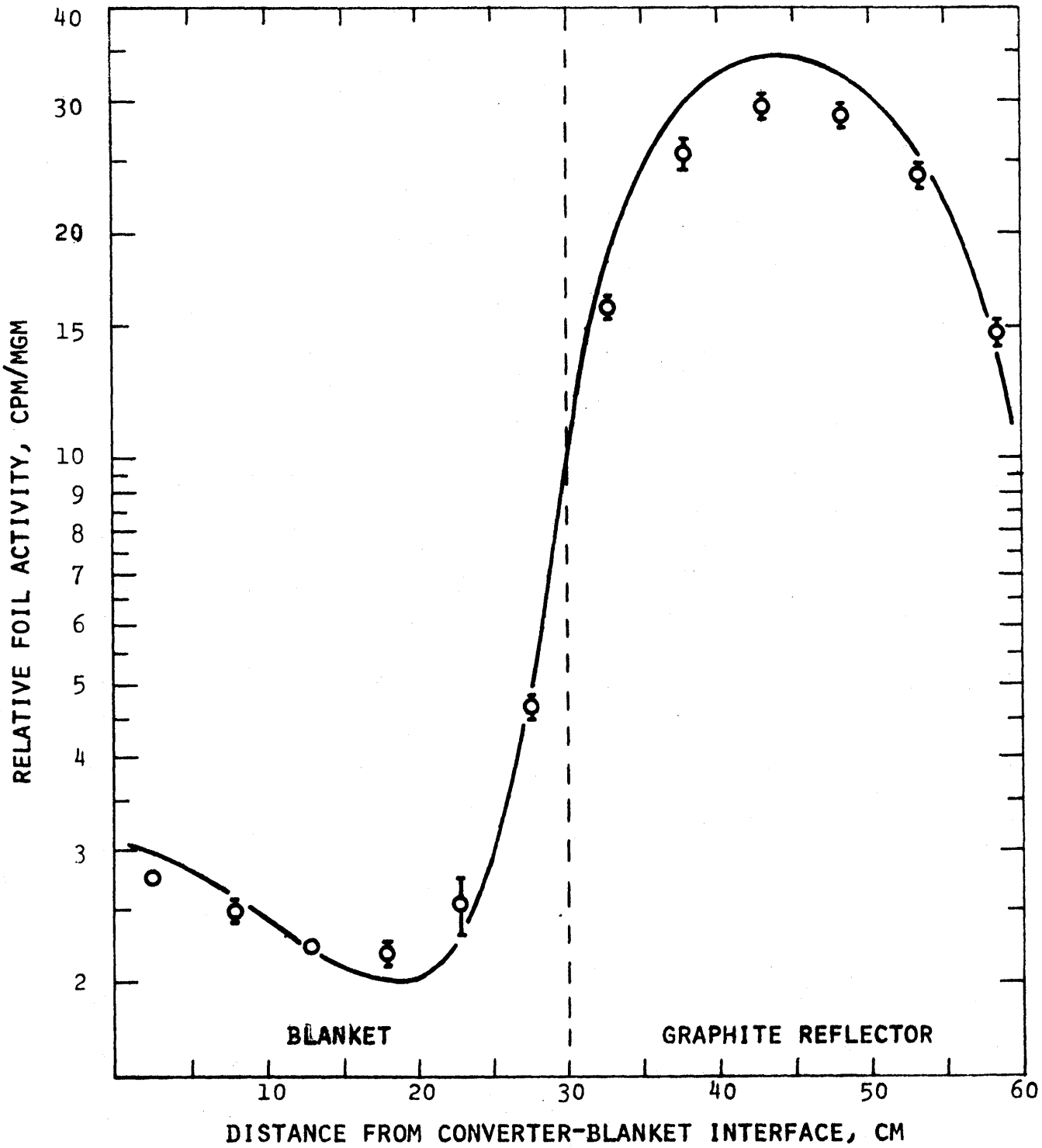

FIG. 4.18 PLUTONIUM-239 (n,f) AXIAL TRAVERSE

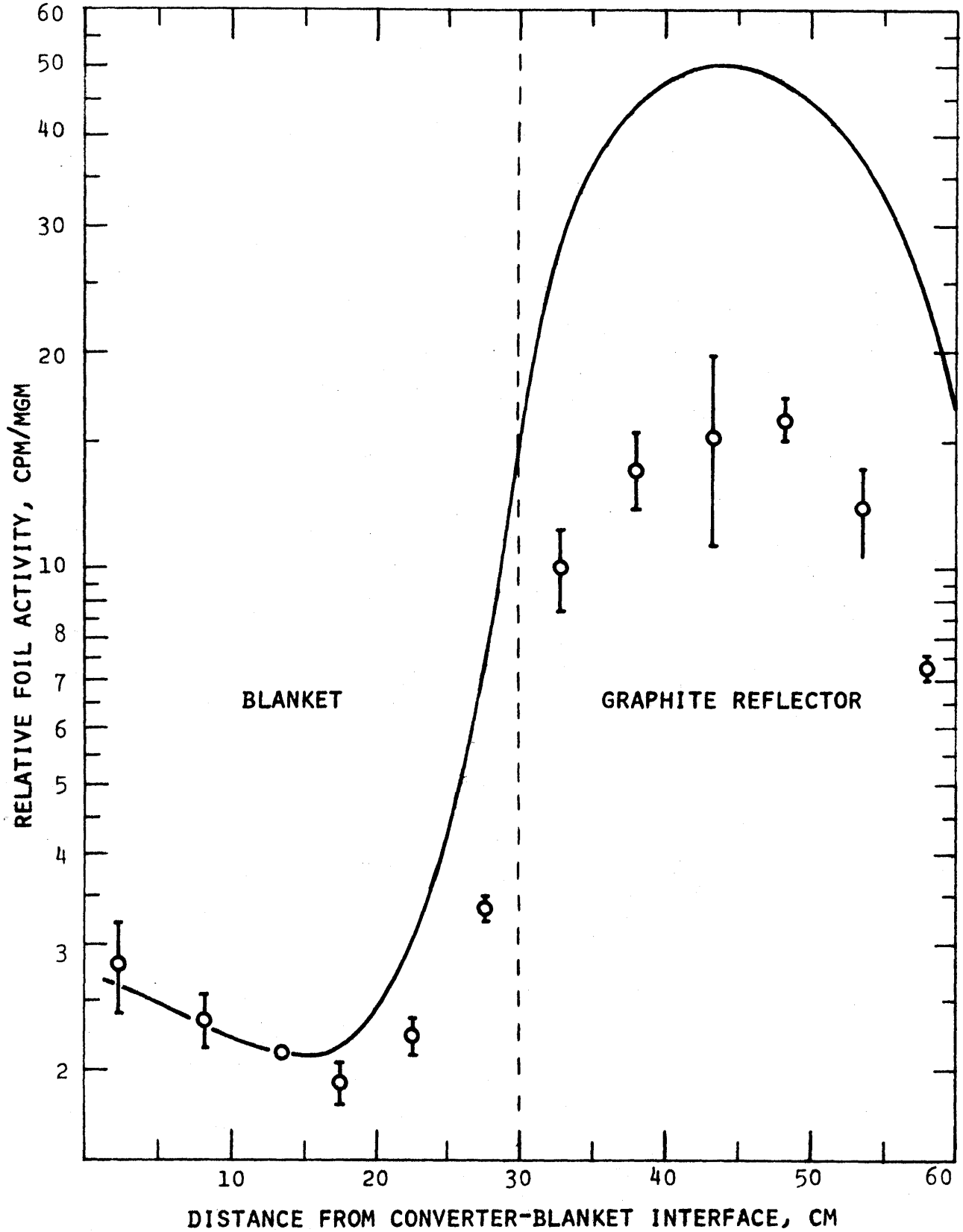

FIG. 4.19 MANGANESE (n,γ) AXIAL TRAVERSE

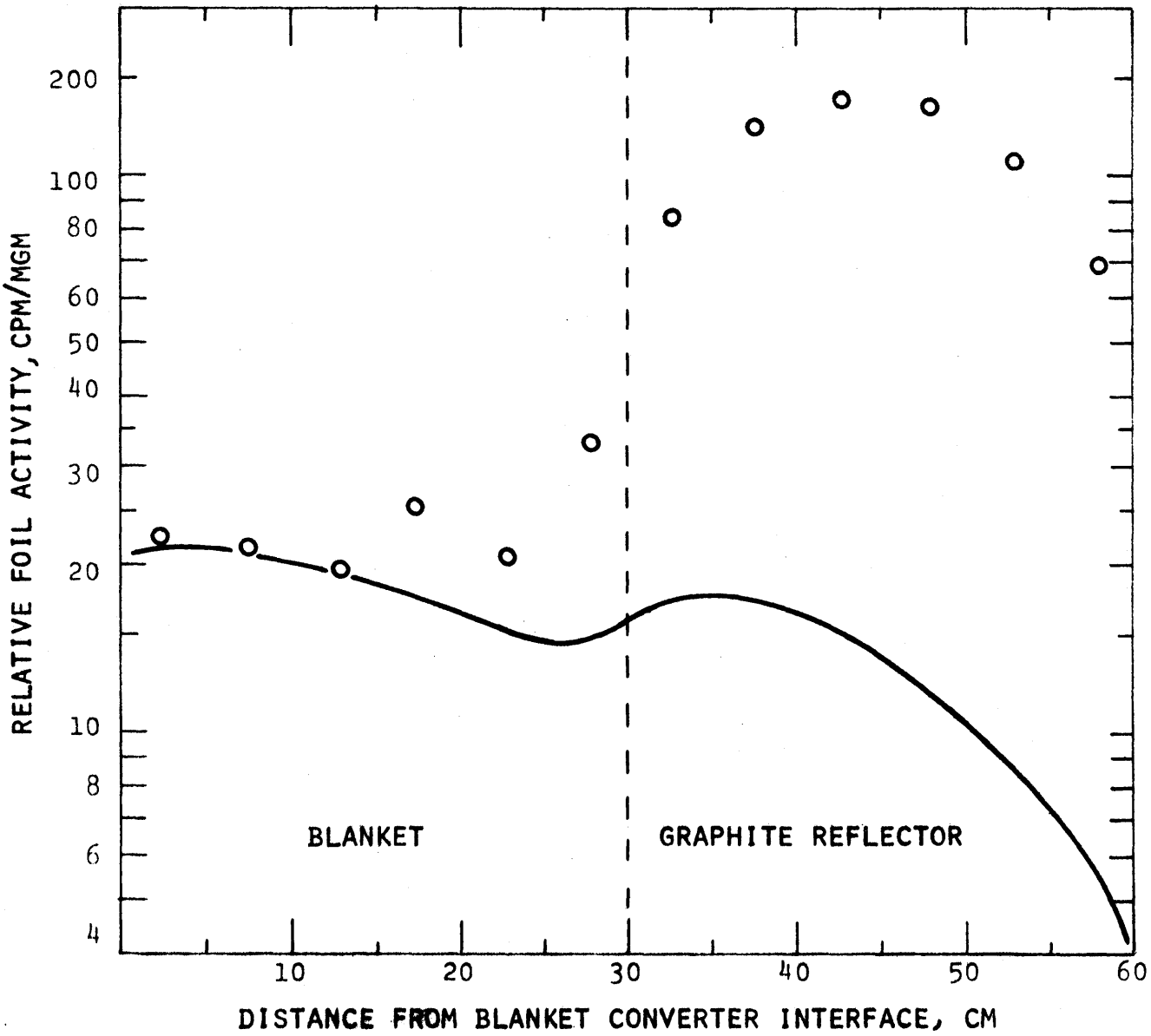

FIG. 4.20 MOLYBDENUM (n,γ) AXIAL TRAVERSE

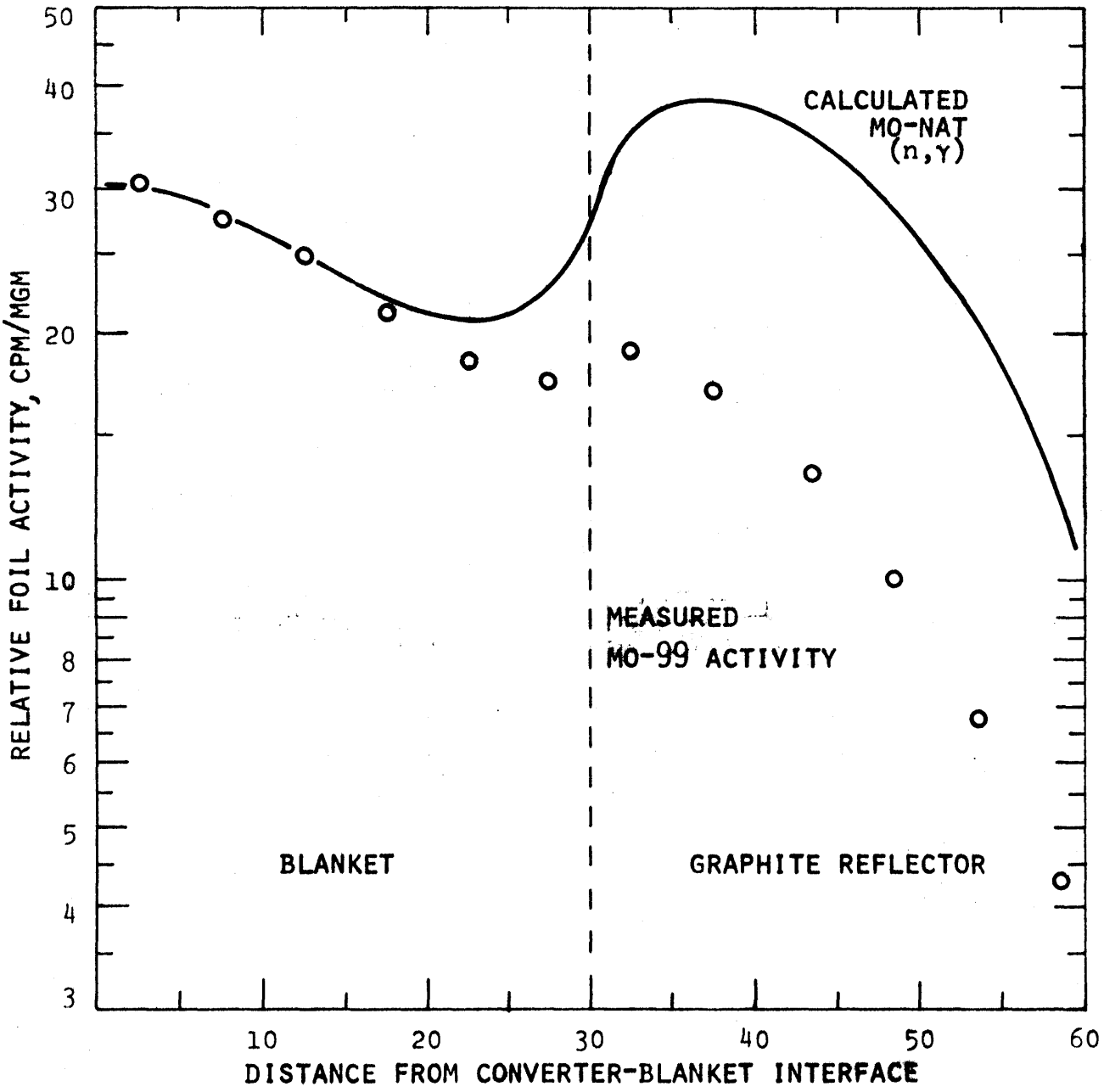

FIG. 4.21 INDIUM (n,n') AXIAL TRAVERSE

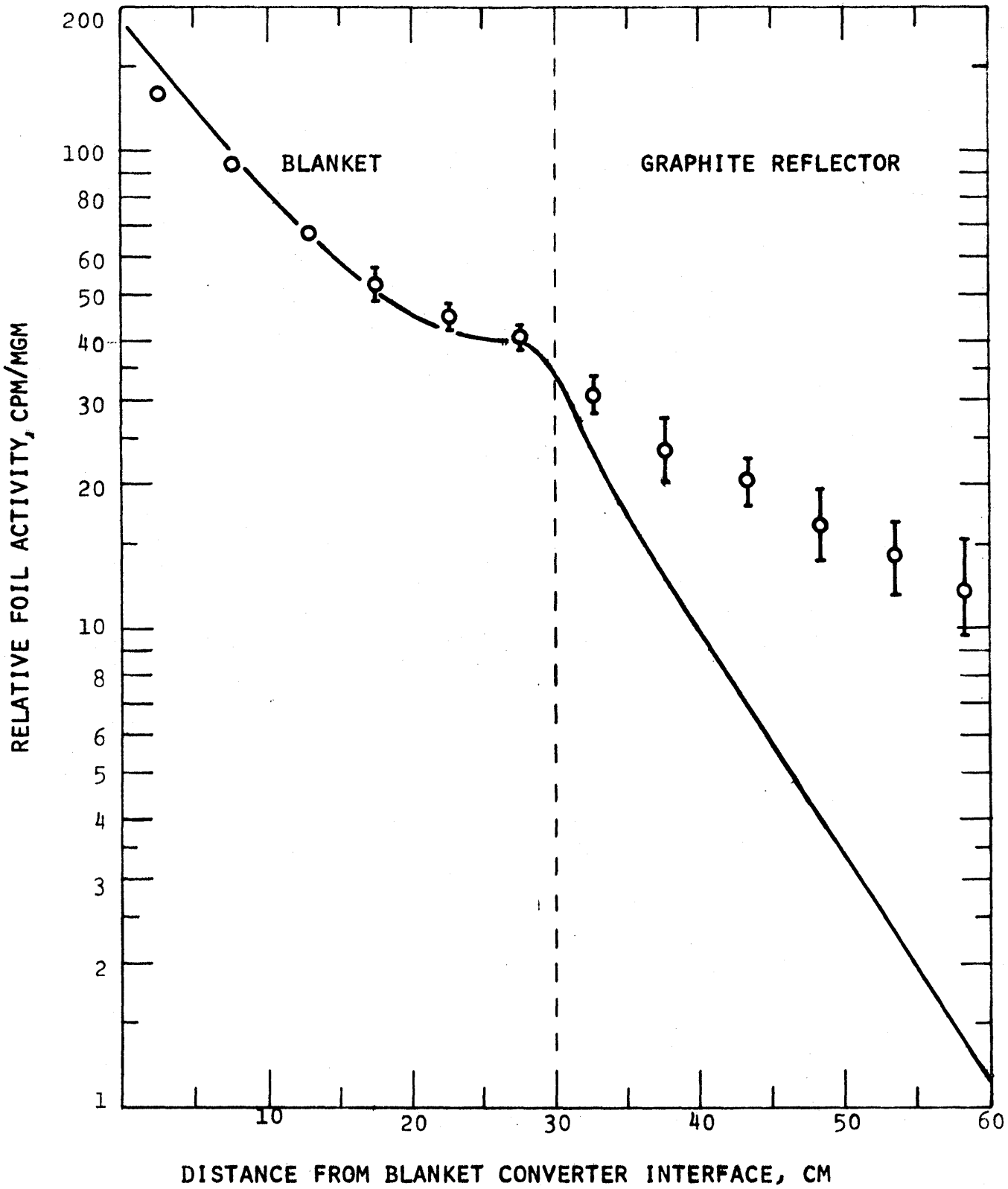

FIG. 4.22 U-238 (n,f) AXIAL TRAVERSE

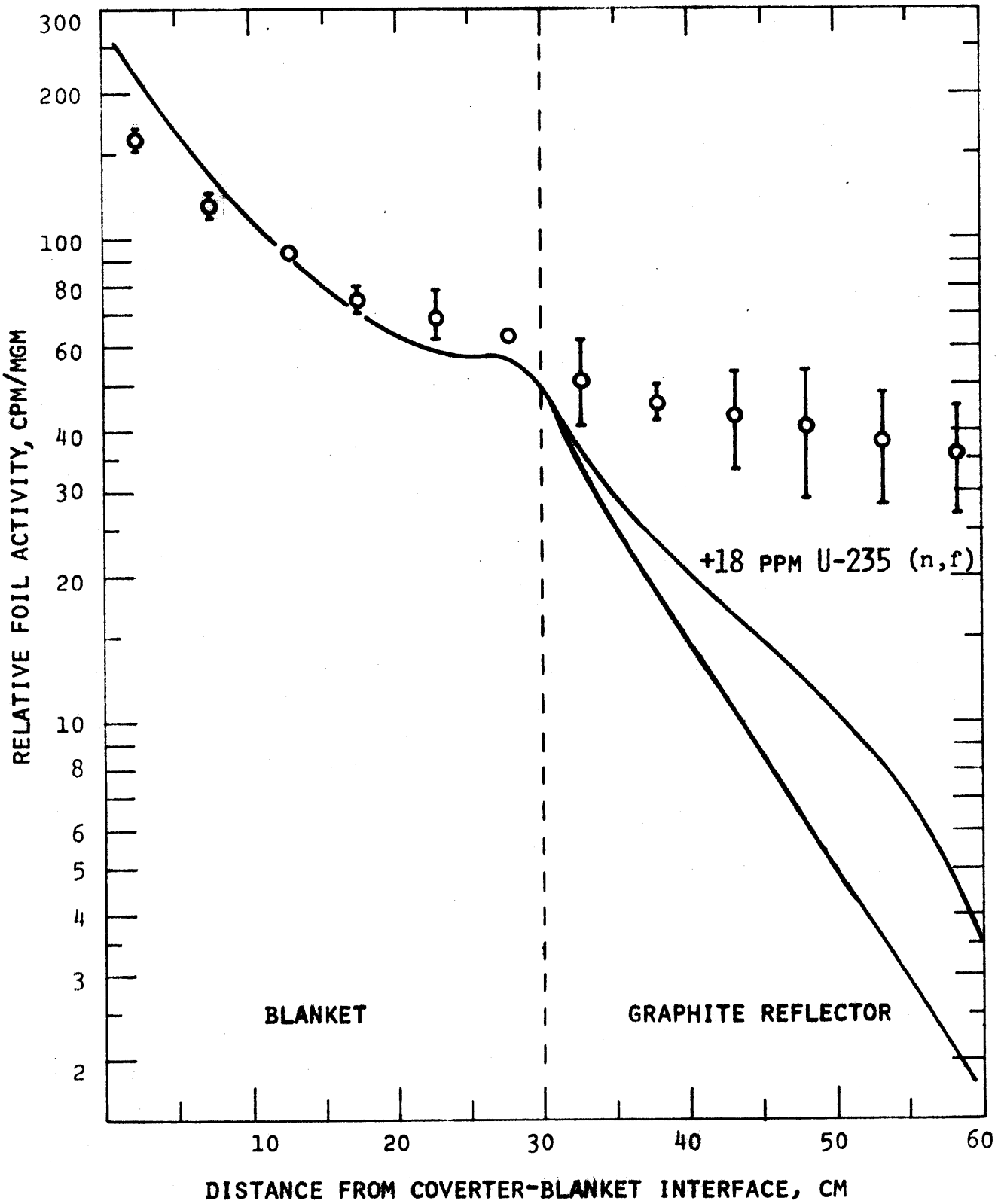

FIG. 4.23 IN AND EX ROD U-238 (n,f) AXIAL TRAVERSE

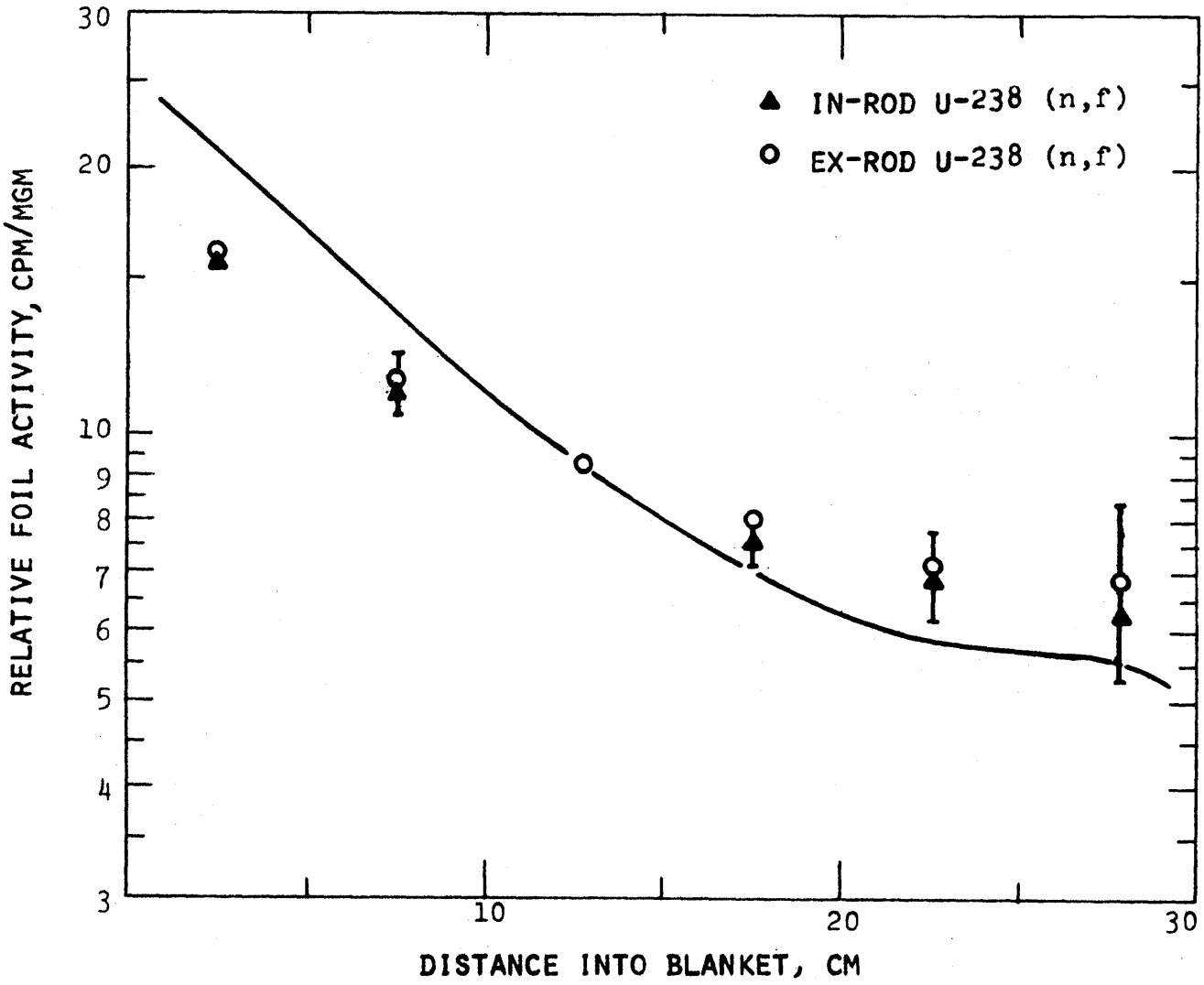

FIG. 4.24 Th^{232} (n,f) AXIAL TRAVERSE

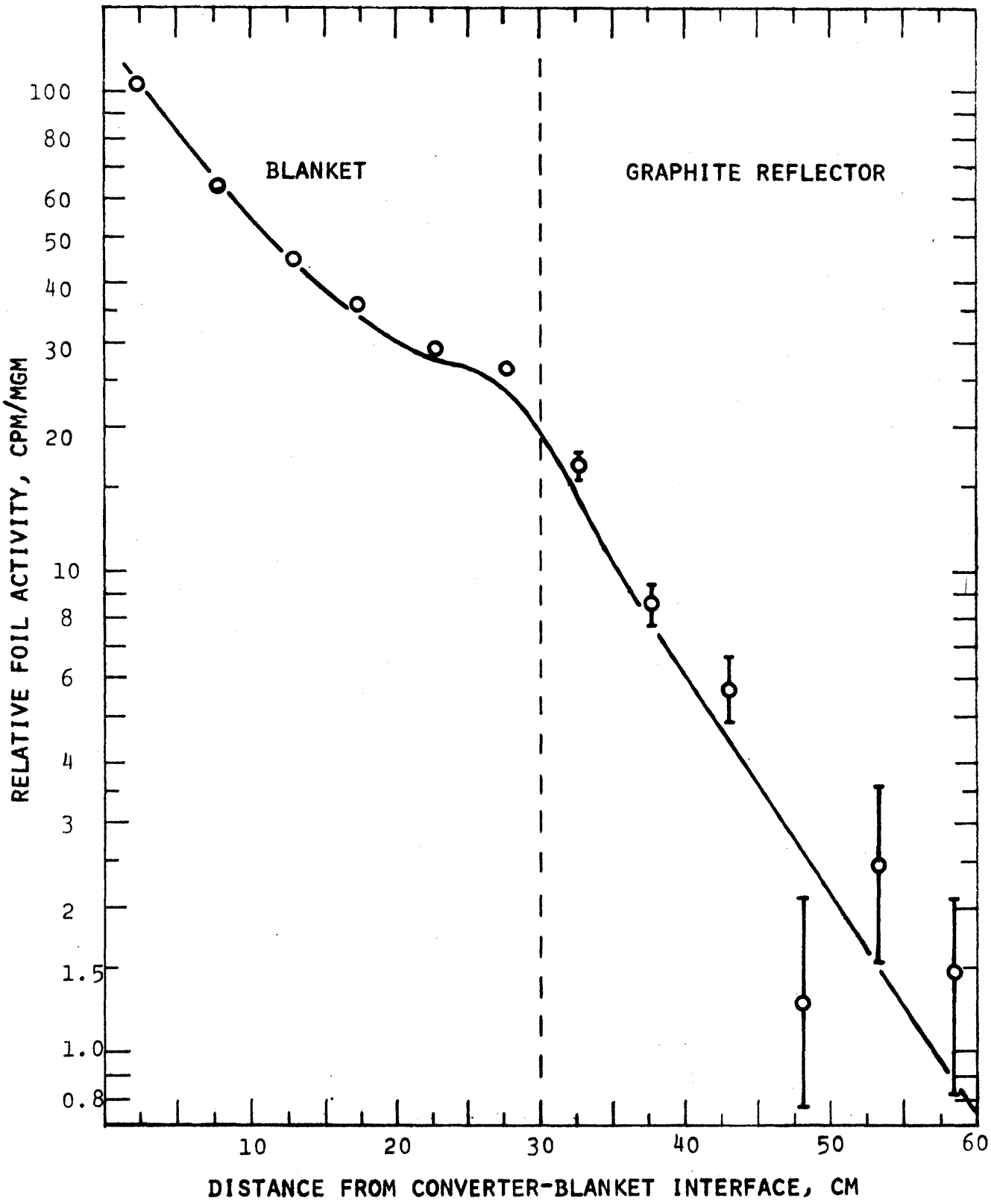

FIG. 4.25 NEPTUNIUM (n,f) AXIAL TRAVERSE

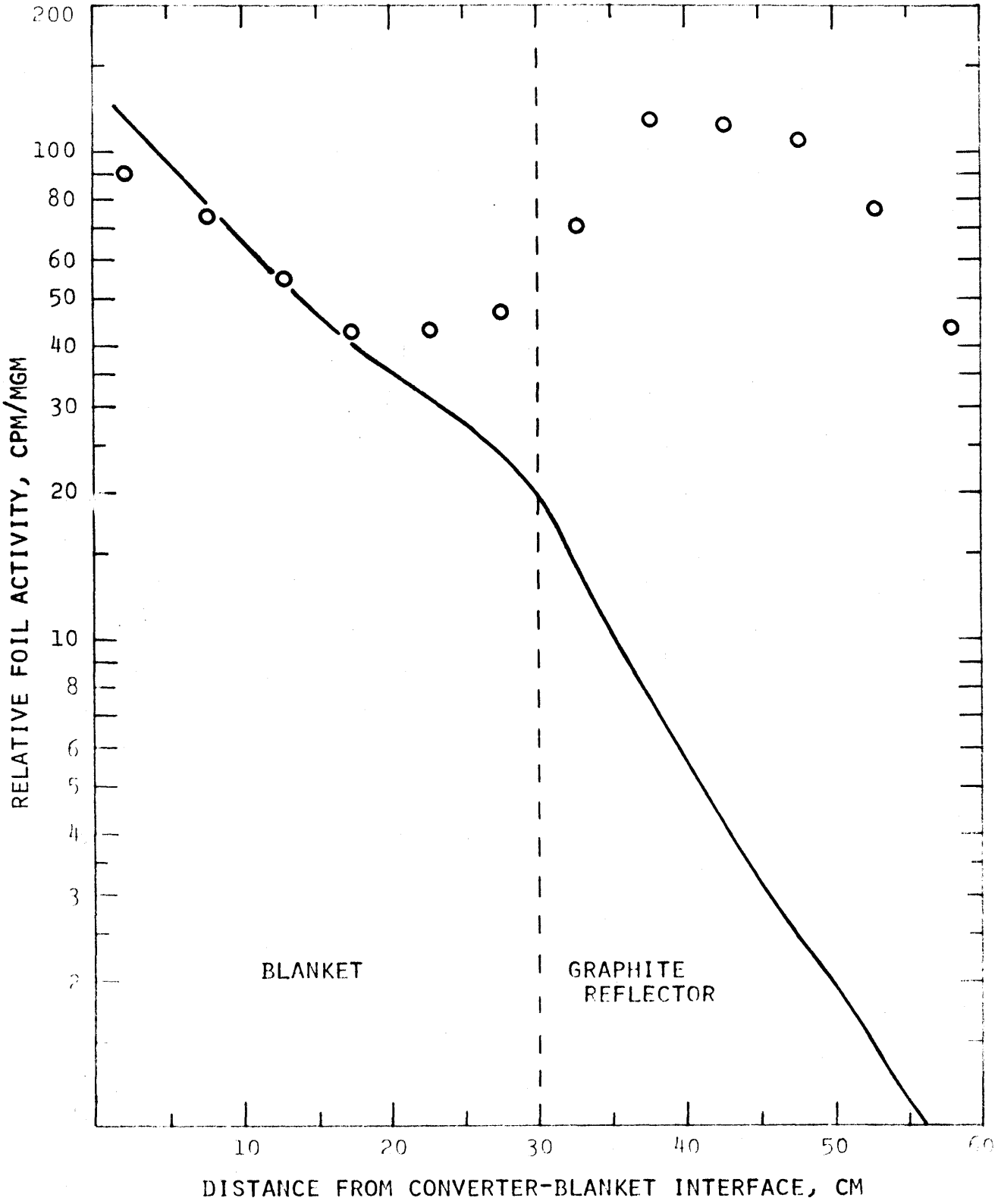

4.4.3 Error Analysis

In general, the experimental error associated with the data reported here is the standard deviation from the mean (SDM) computed from duplicate runs, with allowance made for the small sample size by incorporation of Student's t-factor (10). It is a measure of the overall reproductibility of the data. The governing relations are:

$$SDM = \left[\sum_{i=1}^{N} (Am-Ai)^2/(N-1) \right]^{1/2} \tag{4.4}$$

where

Am = arithmetic mean value of the N different individual repetitions, Ai.

The reported error, $\pm\sigma$ (the "one-sigma" value – namely, the range about the reported value into which 68% of further repetitions would be expected to fall), is then obtained from:

$$\sigma = t \cdot SDM \tag{4.5}$$

where t is Student's t-factor which accounts for the fact that a small sample does not constitute a normal population. For example, $t = 1.84$ for a two-sample population and approaches 1.0 for a large number of samples.

Leung (5) has discussed the various identifiable contributions to the error, including counting statistics, foil weights, time interval determination and the like, and concludes that counting statistics represent the most important factor. In the present work, thorium runs being the main exception, a minimum of 10,000 counts was usually collected on each foil, implying an uncertainty of less than $\pm 1\%$ from this source.

In those few runs, noted in Tables 4.5 through 4.7, where only one set of data was obtained, the error reported is the counting statistic uncertainty:

$$\sigma_C = \sqrt{C} \tag{4.6}$$

where C is the total number of counts accumulated. Experience would

suggest a SDM of ± 1 or 2% for this type of measurement, if repeated.

In all cases, errors have been combined in the usual fashion: for example, in correcting data by background subtraction.

4.4.4 Discussion of Results

4.4.4.1 Buckling Verification

As shown in Fig. 4.9, the buckling in the graphite reflector has the desired cosine distribution. Superposition of the cosine distributions determined for Blanket No. 2 on the experimental data for the graphite reflector of Blanket No. 3 indicates that the horizontal and vertical extrapolated dimensions are again approximately 74 and 60 inches, respectively. It has been shown that the calculated axial reaction rates in the blanket are insensitive to changes in buckling since the transverse leakage is small (5); thus, the transverse buckling value for Blanket No. 3 was set at the value identical to that for Blanket No. 2, and Eq. 4.2 becomes $B^2 = BX^2 + BY^2 = 0.000704\ cm^{-2}$.

The major problem encountered in measuring the buckling in the graphite reflector involved the determination of the spatial shape of the high-energy region of the neutron energy spectrum. The threshold reactions $In^{115}(n,n')$ and $U^{238}(n,f)$ proved unsuitable, owing to poor counting statistics, interference from capture products and – in the case of U^{238} – fission due to fission in the small amount of U^{235} present, which was enhanced by the highly-moderated spectrum. However, it was possible to acquire usable data using the $Th^{232}(n,f)$ reaction, albeit with large relative counting errors.

4.4.4.2 Axial Traverses

The general features of each reaction rate axial traverse will first be discussed, followed by discussion of the discrepancies between the experimental and theoretical results.

Data from two types of gold foils are plotted along with the predicted traverse in Fig. 4.12. In general, and especially in the blanket region, the shape of each is consistent with the prediction. The upper set of experimental points is from the infinitely dilute 2.67 w/o gold

dispersed in aluminum foil. The lower set of data points is from the standard 10-mil-thick foil. The difference between the two, evident in the graphite reflector, is what one would expect – the "infinitely dilute" foil showing higher activation rates than the standard foil. The predicted activation rate, falling between the two experimentally determined rates, indicates that the gold cross sections used in the ANISN calculations may not correspond to a truly infinitely dilute value. The lack of allowance for self-shielding is also characteristic of the other foil traverses and is a major contribution to the discrepancies noted in the graphite region. In general, however, the behavior in the blanket region is of greater concern, since it is there that the important reactions take place.

Figures 4.12 through 4.18 depict axial traverses for reactions having similarly shaped profiles. In each case – gold, sodium, chromium, U^{238} captures, U^{235} and Pu^{239} fissions – the cross section increases, and also displays more prominent resonances with decreasing neutron energy, which accounts for the large peak in the graphite where the flux is much softer than in the blanket, and also for the observation that the unshielded predicted traverse lies above the experimental traverse.

It should be emphasized that in the present work, agreement in the blanket region between experiment and prediction was of primary interest. However, should it become a matter of some practical importance to match the reflector traverses more closely, then the effort must be invested to develop multigroup self-shielding corrections for all of the candidate foil materials. This objective was assigned a low priority for this study.

On the other hand, self-shielding of U^{238} in the blanket region is clearly of considerable interest.

Figure 4.16 displays plots of the measured in-rod and ex-rod U^{238} capture data. As expected, the ex-rod foils are more active, being shielded only by neighboring fuel and not by the host fuel rod. Also shown are the calculated in-rod traverse (normalized to the experimental data) and a comparable traverse calculated using infinitely-dilute U^{238} cross sections (solid line at top of graph)

correctly normalized relative to the in-rod traverse. The same traverse is also shown renormalized to the ex-rod data (dotted line). While it is clear that the ex-rod activities are less shielded than those in-rod, they are far from being in an infinitely dilute environment. Even so, the shape of the infinitely dilute calculated traverse is in fair agreement with that of the ex-rod measured traverse. It should also be noted that Leung (5) shows a comparable plot for Blanket No. 2 in which only the infinitely-dilute U^{238} calculations normalized to the ex-rod data are shown, and which may therefore give the false impression that the ex-rod foils can be correctly represented as infinitely dilute.

The results shown in Fig. 4.16 display the expected effects of spectral softening near the graphite reflector: the in-rod flux depression is enhanced and the spread between the in-rod and ex-rod traverses widens.

The manganese data of Fig. 4.19 show extremely poor agreement with the predicted traverse, leaving in doubt the validity of the manganese cross section, or the experiment, or both. No plausible explanation can be offered at the present time.

Molybdenum (Fig. 4.20) shows only slightly better agreement between experiment and prediction. In the first row of blanket, adequate agreement is found (due, in part, to the normalization); however, deeper in the blanket and in the graphite reflector, the prediction is too high by a factor of almost 2.5. As before, this is probably due in part to the spectral shift in the blanket and the inability of the cross sections used by this "keV range" absorber to properly reflect the self-shielding. A further obvious source of discrepancy is that natural molybdenum cross sections were employed, whereas the measured Mo^{99} activity is produced from isotope Mo^{98}, which is only 24% abundant.

The last set of graphs, Figs. 4.21 through 4.25, depict threshold reactions: inelastic scattering by indium ($E_t = 0.3$ MeV) and fast fission in uranium-238 ($E_t = 1.0$ MeV), thorium-232 ($E_t = 1.75$ MeV), and neptunium ($E_t = 0.75$ MeV). The predicted axial traverses have practically identical shapes for all of these reactions, implying that

the fast reactions (above 300-keV indium threshold) behave similarly.

The experimental data agree quite well with the predictions in the blanket region. However, in the graphite, the situation is different. Within the experimental error, the thorium data and prediction agree; the other three sets of data do not. The neptunium data exhibit a peak in the reflector region, similar in shape to the nonthreshold reactions discussed previously. This would indicate that Np^{237} capture products (Np^{238}, T 1/2 = 2.1 d) and not fission products were actually being counted in the experiment. This was undoubtedly the case, since it was found necessary in the counting procedure to use a baseline setting above the Np^{238} 1.03-MeV gamma peak to count the fission products. However, the observed Np^{238} contribution was so strong that this effect was probably not entirely eliminated.

The uranium and indium data deep in the reflector are an order of magnitude higher than calculated. It is important to note that this is the same problem observed in the steel reflector of Blanket No. 2. Correcting U^{238} fissions for contamination by fission in the 18-ppm U^{235} does not solve the problem. To date, no completely satisfactory answer has been derived for either case. Since the thorium data do not exhibit this discrepancy, the effect could be explained by a neutron "window" in the 0.3-1.0-MeV range. Another explanation could be that there are competing neutron reactions that are contaminating the measurements of the desired (n,n′) and (n,f) reactions. For example, Swedish researchers have attributed similar discrepancies for the In(n,n′) reaction in water shielding studies to gamma excitation of the appropriate indium level (11). Further experiments to resolve this discrepancy are planned for Blankets Nos. 4 and 5.

4.5 Summary

Blanket No. 3, incorporating a moderating, high-albedo graphite reflector has been designed, built, and studied. Previous analytical studies (2, 3) indicating possible economic advantages for this blanket-reflector combination motivated this study in order to reinforce the confidence placed in the analytical results, particularly in view of the

severe spectral changes in the blanket-reflector region which made it questionable whether or not the codes and cross sections available could adequately describe this type of configuration. The general conclusion that can be drawn from this effort is that the analytical methods adequately describe the neutronic behavior of the blanket.

However, the fast flux in the reflector is not being predicted well, and serious questions with respect to fast neutron damage and shielding can thereby arise. To investigate this problem further, detailed measurements in the steel reflector region are proposed in Blanket No. 5.

4.6 References

(1) Forbes, I.A., et al., "Design Construction and Evaluation of a Facility for the Simulation of Fast Reactor Blanket," MITNE-110, MIT-4105-2 (February 1970).

(2) Forbes, I.A., et al., (editors), "LMFBR Blanket Physics Project Progress Report No. 1," MITNE-116, MIT-4105-3 (June 30, 1970).

(3) Forbes, I.A., et al., (editors), "LMFBR Blanket Physics Project Progress Report No. 2," COO-3060-5, MITNE-131 (June 30, 1971).

(4) Kang, C.S., et al., "Use of Gamma Spectroscopy for Neutronic Analysis of LMFBR Blanket," COO-3060-2, MITNE-130 (Nov. 1971).

(5) Leung, T.C., et al., "Neutronics of an LMFBR Blanket Mock-Up," COO-3060-1, MITNE-127 (January 1972).

(6) Ortiz, N.R., et al., "Instrumental Methods for Neutron Spectroscopy in the MIT Blanket Test Facility," COO-3060-3, MITNE-129 (May 1972).

(7) Engle, W. W., "A User's Manual for ANISN," K-1693 (March 1967).

(8) Abagyan, L.P., et al., Group Constants for Nuclear Reactor Calculations, I.I. Bondarenko (ed.), Consultants Bureau (1964).

(9) McElroy, W.N., "A Computer-Automated Iterative Method for Neutron Flux Spectra Determination by Foil Activation," AFWL-TR-67-41 (August 1967).

(10) Mickley, H.S., et al., Applied Mathematics in Chemical Engineering, McGraw-Hill Book Company (1957).

(11) Aalto, E., et al., "Measured and Predicted Variations in Fast Neutron Spectrum in Massive Shields of Water and Concrete," AE-197 (1965).

5. THE EFFECTS OF HETEROGENEITY

5.1 Introduction

Experimental and analytical work on the effects of heterogeneity on blanket neutronics has been carried out in a number of areas. Two-piece annular foil irradiations have been made to characterize the in-rod U^{238} capture profile; six-piece annular foil experiments have been performed to confirm the validity of relying upon two-piece foil data; and numerical and analytical studies are being carried out to relate calculation to experiment and also to assess all important contributions of heterogeneity to LMFBR neutron balances.

5.2 Two-Piece Foil Irradiations

The work whose initiation was described in reference (1) has been completed, in which two-piece annular foils were irradiated in both the U-metal fuel rods used in the blanket mock-up and in the sodium-"cooled" UO_2 fuel rods of a special subassembly (1) inserted into Blanket Mock-Up No. 2. The work was also extended to encompass similar measurements in U-metal fuel in Blanket Mock-Up No. 3. The results are summarized in Table 5.1 in terms of F, the ratio of the average activation within the rod to the activation at the rod surface.

A number of interesting qualitative conclusions can be drawn from the results: the uranium metal and uranium dioxide fuel have essentially the same self-shielding characteristics; the reduction in self-shielding upon voiding of sodium is evident; and the progressive softening of the spectrum as one moves deeper into the blanket is evidenced by an increase in self-shielding, especially in Mock-Up No. 3, the two-row, graphite-reflected blanket.

TABLE 5.1

Results of Annular U^{238} Foil Irradiation

Blanket Number	Subassembly Row	F	Comment
2	Front	0.91	In U-metal
	Front	0.91	In UO_2
	Middle	0.90	In U-metal
	Middle	0.91	In UO_2
	Middle	0.94	In UO_2, sodium voided
	Middle	0.89	In UO_2, 6-piece foils
	Outer	0.87	In U-metal
	Outer	0.84	In UO_2
3	Front	0.91	In U-metal
	Rear	0.84	In U-metal

Notes:

(a) F = average $U^{238}(n,\gamma) \div$ surface $U^{238}(n,\gamma)$ measured using Np^{239} activity.

(b) Typical standard deviation: ± 3%.

(c) U-metal fuel is 0.250 in O.D.; UO_2 fuel is 0.430 in O.D.

5.3 Six-Piece Foil Irradiations

Six-piece annular foils were irradiated in the UO_2-sodium subassembly of Blanket Mock-Up No. 2 in order to confirm the theoretical assertions used to justify employing two-piece foils for self-shielding measurements.

By treating a fuel rod as a nearly transparent medium containing a spatially uniform source or sink of neutrons, a particularly simple low-order approximation to the in-rod flux (hence material activation) profile results (2):

$$A(r) = C_0 + C_1 E\left[\left(\frac{r}{a}\right)^2\right], \tag{5.1}$$

where C_0 and C_1 are constants, a is the rod radius and E is the complete elliptic integral of the second kind. Equation 5.1 is of intriguing simplicity in that it implies all in-rod fluxes have the same shape, differing only in the relative amplitude of enhancement or depression.

The six-piece foils were irradiated and counted in exactly the same manner as the two-piece foils and the results least-squares curve-fitted to Eq. 5.1. It was found that Eq. 5.1 reproduced the measured U^{238} capture rate profile to within ± 2%, which was also the estimated precision of the measurements. Many other tests of this relation were also conducted, including comparisons with multiple-piece foil irradiation in thermal reactor fuel elements and to ANISN S-8 calculations, with equally good and, in most instances, even better results. It was therefore concluded that for present purposes, Eq. 5.1 is adequate for interpretation of the experimental data; and since Eq. 5.1 involves only two unknowns, a two-piece foil will suffice.

Given the validity of Eq. 5.1, the self-shielding ratio, F, average-to-surface activity, can be determined in several ways. For multiple-piece foils, the constants C_0 and C_1 were determined by least-squares analysis, following which:

$$F = \frac{C_0 + \frac{4}{3} C_1}{C_0 + C_1} \tag{5.2}$$

For the two-piece foils, on the other hand, it is more appropriate to employ the specific activities of the inner and outer foil pieces directly:

$$F = \frac{\left(\frac{1}{y}\right) \int_0^y E(x)\, dx - \frac{4}{3}}{\left(\frac{1}{y}\right) \int_0^y E(x)\, dx - \frac{1}{3} Z - 1} \qquad (5.3)$$

where

y = ratio of inner foil weight to that of both pieces,

Z = ratio of specific activity of inner foil (CPM/MG) to that of both pieces.

Equations 5.2 and 5.3 were employed to generate all results quoted in Table 5.1. Note that the two-piece U-metal and six-piece UO_2 traverses in a comparable environment (middle row, Blanket No. 2, sodium-in) agree well within the experimental accuracy.

5.4 Analytical Investigations

Calculations of U^{238} resonance self-shielding effects were continued, using the MIDI program (3). The two most pertinent results were the discovery that: (a) Rod size was not an important effect; apparently, the Dancoff correction term compensates for the in-rod effect. (b) As shown in Table 5.2, the U-metal unit cell of the blanket mock-ups affords a good representation of the heterogeneity of real blankets. The BTF is intermediate between a typical radial and a typical axial blanket, being somewhat closer to the latter.

Work is also under way to determine the simultaneous influence on core and blanket neutronics of all of the major heterogeneous effects, including anisotropic diffusion, coarse-group flux shape within the cell, and resonance self-shielding. Preliminary results indicate that U^{238} self-shielding is the only heterogeneous effect having a major impact on the neutron balance in the blanket region; and that anisotropic diffusion has a rather important effect on core reactivity, especially in

the sodium voiding accident where it tends to make the reactivity addition less positive by on the order of one dollar.

TABLE 5.2

BTF Resonance Self-Shielding Comparison

	BTF (barns)		(Typical Blanket σ) ÷ (BTF σ)			
			Axial		Radial	
Group	σ_a	σ_s	abs	scat	abs	scat
11	0.4843	10.99	1.0010	1.0009	0.9738	0.9864
12	0.7641	11.65	1.0059	1.0034	0.9627	0.9777
13	0.5480	11.56	1.0361	1.0112	0.9407	0.9818
14	0.6142	10.27	1.0451	1.0078	0.9324	0.9883
15	0.8075	10.55	1.0578	1.0104	0.9226	0.9858
16	0.7276	9.574	1.0686	1.0049	0.9089	0.9939
17	1.200	11.91	1.0642	1.0160	0.9208	0.9815
18	3.281	12.53	1.0585	1.0144	0.9137	0.9785
19	2.676	11.47	1.0486	1.0096	0.9152	0.9826
20	7.265	10.60	1.0406	1.0066	0.9310	0.9896
21	7.730	9.446	1.0445	1.0021	0.9352	0.9969

5.5 Discussion

All of the analytical and experimental effort to date supports the contention that U^{238} self-shielding is an extremely important effect which must be correctly accounted for if one is to describe accurately the various elements of the neutron balance. Unlike the situation with plate-type critical experiments, the rod-lattices used in the BTF appear to be very similar to actual LMFBR designs in terms of their heterogeneous reactor physics description. Further, it has been shown that simple two-piece foil irradiation can provide useful information on resonance self-shielding of U^{238}. The major remaining task, which is the subject of work currently under way, is to derive

a quantitative connection between the results of these experiments and the results of MIDI code computations.

5.6 References

(1) "Heterogeneous Effects in LMFBR Blanket Fuel Elements," Ch. 7 in "LMFBR Blanket Physics Project Progress Report No. 2," COO-3060-5, MITNE-131, June 30, 1971.

(2) Thompson, A.M., "Activation Profiles in Reactor Fuel Elements," B.S. Thesis, M.I.T. Physics Department, June 1972.

(3) Rogers, V.C., and I. A. Forbes, "Calculation of U-238 Cross Sections," Ch. 8 in "LMFBR Blanket Physics Project Progress Report No. 2," COO-3060-5, MITNE-131, June 30, 1971.

6. ECONOMIC EVALUATION OF BLANKET PERFORMANCE

The work summarized in the present chapter is primarily concerned with the formulation of a consistent economic model which can be used to evaluate the comparative performance of LMFBR blanket designs and thereby help guide the selection of blanket mock-up experiments for the MIT Blanket Test Facility (1, 2). The complete results are presented in the topical report:

> S.T. Brewer, E.A. Mason and M.J. Driscoll, "The Economics of Fuel Depletion in Fast Breeder Reactor Blankets," COO-3060-4, MITNE-123 (est. Nov. 1972).

6.1 Introduction

A Fast Breeder Reactor blanket performs several functions: it acts as a fertile-to-fissile material converter, as a reflector, and as a shield. In addition, it produces some power, thereby relieving, slightly, the power burden on the core. Of these functions, the fissile breeding objective is considered paramount. For current 1000-MWe designs, a fast reactor without blankets is not a breeder; although most of the conversion is accomplished in the core (internal breeding ratio ~ 0.8), a fertile blanket is required to achieve overall breeding ratios greater than unity.

Objectives of the work reported here were twofold: (1) to develop a simple depletion-economics calculational tool for survey evaluations of LMFBR blanket configurations; and (2) to perform several comparative studies around a 1000-MWe reference LMFBR configuration. The 1000-MWe case studies involve choice of radial reflector material (Be-metal vs. sodium), radial blanket thickness, advantages of local fuel management in the radial blanket, and the sensitivity of LMFBR fuel energy costs to changes in the economic environment.

6.2 Qualitative Discussion of FBR Blanket Design Considerations and Literature Survey

The major economic objective of FBR blanket design is to maximize the net blanket fissile revenue, that is, to maximize the fissile credit less fabrication, reprocessing, and carrying charges. At the same time, thermal-hydraulic engineering design seeks to minimize the effects of the blanket power swing over a refueling cycle interval and to minimize the power gradient across the blanket. Other engineering considerations are the shielding role of the blanket, and possible material constraints on blanket exposure.

The blanket designer has several design variables and options to work with in meeting these objectives while satisfying the constraints. Some of the major variables and options are discussed qualitatively below. Studies which have addressed these considerations are listed in the references.

6.2.1 Blanket Thickness

Selection of blanket thickness involves a tradeoff between the fissile plutonium production rate and fuel cycle costs – fabrication, reprocessing, and associated carrying charges. An incremental increase in blanket thickness imposes additional fabrication and reprocessing costs while providing some additional fissile production. The incremental increase in fissile production decreases with blanket thickness because of flux attenuation. An incremental increase in thickness beyond some point is unprofitable; the added fissile revenue is not sufficient to offset the added fabrication and reprocessing costs.

The "optimum" thickness depends on the economic environment – fissile value ($/kg Pu_f), fabrication cost ($/kg HM), and reprocessing cost ($/kg HM). Thick blankets are indicated when fissile value is high and/or fabrication and reprocessing costs are low. Thicker blankets may also be in order when leakage flux to the blanket is increased due to changes in core design.

The Westinghouse LMFBR Follow-On Studies (3), Task I, have shown that the optimum radial blanket thickness is not sharp; that is,

the blanket profit is a weak function of blanket thickness. This conclusion is borne out in the present study. The Westinghouse optimum thickness is between 25 cm and 30 cm, again consistent with the present study.

6.2.2 Blanket Irradiation Time

Below some irradiation time, T_1, the bred fissile inventory in the blanket is not sufficient to offset the blanket fabrication, reprocessing, and carrying charges. At T_1, the "break-even point," the revenue from bred fissile is just equal to fabrication, reprocessing, and carrying charges. Beyond T_1, the blanket produces a net profit. As irradiation time T is further increased, Pu^{239} is produced at a decreasing rate because of the burnup of both fertile U^{238} and fissile Pu^{239}, and the fissile credit averaged over irradiation time T decreases. Also, as irradiation time T increases, carrying charges increase, and direct fabrication and reprocessing charges decrease. Taken together, these opposing effects result in an optimum irradiation time, Topt, at which the net revenue in $/kg HM/year (or in mills/KWHe) is a maximum.

Local optimum irradiation time decreases, and local net revenue at the optimum increases, with increased local flux. Thus regions near the blanket-core interface reach their optima sooner and produce more revenue than regions deeper in the blanket. For pancaked cores, the axial blanket optimum irradiation time is less than that of the radial blanket. Thinner blankets enjoy shorter optimum irradiation times.

Several studies have assessed optimum blanket irradiation times for particular designs (4, 5, 6, 7). Typical local optima range from about two to about eight years across the radial blanket.

Engineering considerations such as burnup, power swing, corrosion, and irradiation damage of cladding may tend to limit feasible irradiation time.

6.2.3 Blanket Fuel Management Scheme

Axial blanket fuel management is constrained to that of the core, since axial blanket fuel assemblies are merely extensions of core assemblies in present LMFBR designs. The core-axial blanket fuel management scheme adopted in the 1000-MWe LMFBR Follow-On Studies (3, 7, 8, 9, 10) can be described as a region-scatter scheme. In this scheme, the core-axial blanket is divided into annular regions. At each refueling event, fractions $g_1, g_2, \ldots$ of regions $1, 2, \ldots$ are discharged and replaced with fresh fuel. Fuel sees only one position in the reactor. The discharge fractions $g_1, g_2, \ldots$ decrease with distance from the core centerline, implying that irradiation times increase with distance from the core centerline. This procedure enhances flux flattening and discharge burnup uniformity.

Radial blanket fuel management is independent of that of the core-axial blanket, with the restriction, of course, that blanket refueling dates coincide with those of the core-axial blanket, to minimize reactor shutdowns for refueling. With the exception of Westinghouse (3), the scheme selected in the 1000-MWe Follow-On Studies is region-scatter. Again, irradiation time increases and discharge fraction decreases with distance of the region from the core-blanket interface, thus implementing flux flattening across the blanket. Batch management is the special case of scatter management in which the discharge fractions are set equal to unity; i.e., at each refueling event for a given region, 100% of the fuel is discharged and replaced with fresh fuel.

Other schemes proposed for the radial blanket are out-in, in-out, and fuel assembly rotation. The Westinghouse Follow-On design (3) specifies in-out. In this scheme, fresh fuel is loaded in the innermost blanket region and is moved outward in subsequent refuelings, remaining in each annular region for one or more cycles. Fuel is discharged, finally, from the outermost region. Advantages (11) of the in-out management are power flattening, reduction of local power swing, and burnup uniformity. An earlier study (5) argued qualitatively that in-out management would be uneconomic due to the prolonged holdup of bred fissile. This was not demonstrated quantitatively.

In the out-in scheme, fresh fuel is loaded in the outermost region, moved inward, and discharged from the innermost region. The scheme has the advantage of achieving uniform burnup and would tend to reduce the power swing over an irradiation cycle. However, out-in would tend to aggravate the power tilt across the blanket. Out-in management was compared (5) to fixed element management (batch or scatter) and was found to have only a few percent profit advantage.

A recent study (12) has investigated the optimum out-in throughput for a 1000-MWe LMFBR radial blanket. The study determined the effect of throughput on 10-year fuel cycle costs. Halving of the radial blanket out-in throughput increased fuel cycle costs (from optimal) by less than 5%. Increasing the throughput by a factor of about 1.5 increased the 10-year fuel cycle cost by about 1%.

The optimum throughput analysis reported in this (12) study was used as an illustration of a computational method for selecting optimal FBR fuel management strategies in a changing economic environment. The method permits changing fuel management during plant life (in response to changes in the economic environment) in order to minimize fuel costs during the remainder of plant life. In the radial blanket illustration cited, remaining plant life is 10 years.

Fuel element rotation has been studied by Westinghouse (11). Rotation may be considered a sub-fuel management scheme in that it may be used in conjunction with the other schemes. During a refueling, fuel assemblies are simply rotated in place, thus moving fuel with high fissile content deeper into the blanket. Advantages of rotation are power-flattening and reduction of local power swing over an irradiation cycle. Westinghouse has shown that the maximum (with time) rod peaking factor for a radial blanket rod adjacent to the core can be reduced by about 20% by rotation. The reduction in power peaking across the blanket was not reported. Also, the effect of rotation on breeding economics was not reported.

6.2.4 Inner Radial Moderator

Insertion of a layer of moderating material between core and blanket would offer the advantage of softening the leakage flux entering the blanket, improving the fertile capture rate per incident neutron. On the other hand, the incident flux (entering the blanket) would be diminished due to absorption and reflection by the moderating layer. Thus the net effect of inner radial moderator configuration on blanket breeding is not qualitatively clear. Furthermore, one might expect the moderating layer to return more neutrons to the core and to degrade the returning spectrum. The net effect (on critical mass and internal breeding ratio) of the improved reflection plus degraded core spectrum is also not intuitively evident.

Perks and Lord (13) have performed survey calculations on the inner radial moderator concept, using a variety of moderating materials and thicknesses. Candidate materials were graphite (82% graphite), graphite-steel (41% graphite, 51% stainless steel), and sodium (100% sodium). The inner radial moderator configuration consistently resulted in a small reduction in critical mass, an increase in internal breeding ratio, a reduction in blanket breeding ratio, and a net reduction in total breeding ratio. Their cost results (13) show that the core fissile inventory reduction does not offset the breeding revenue reduction; thus, the inner radial moderator concept does not appear economically attractive.

6.2.5 Moderated Blankets

Replacing some blanket fuel with moderator material would tend to soften the blanket spectrum, enhancing the conversion rate per unit of fuel. Opposing this effect is the lessened gross breeding occasioned by the diminished fuel content. Some candidate moderating materials are graphite, ZrH_2, and BeO.

Two studies (5, 6) have investigated the breeding economics of moderated blankets. Hasnain (5) considered graphite in an LMFBR radial blanket, while Mayer (6) considered graphite, ZrH_2, and BeO in a steam-cooled fast reactor (SCFR) radial blanket. In all cases,

the inclusion of moderating materials (at the expense of fuel volume) led to a reduction in breeding ratio. Core parameters (k_{eff}, critical mass) were only slightly affected. Both studies concluded that moderated blankets offered no significant economic advantages.

Another study (12) has shown that seeding a typical LMFBR radial blanket with carbon leads to a slight improvement in the breeding performance of the inner radial blanket: about 10% increase in inner radial blanket fissile concentration. The outer radial blanket was found to be practically unaffected.

6.2.6 Radial Reflector

Functions of the radial reflector are: (1) to enhance radial blanket performance by flattening blanket flux and, possibly, by softening the return spectrum; and (2) to provide a neutron shield for structural materials outside the reactor. Two major design decisions are choice of radial reflector composition and choice of radial reflector thickness.

In the Westinghouse LMFBR Follow-On work (3), Fe, C, Ni, and Na (reference case) reflectors were compared for a 10.5-inch-thick radial blanket. Maximum improvement (over the Na-reflected case) in radial blanket fuel economic performance was only 0.008 mill/KWHe (the 12-inch graphite reflector). A 3-inch Fe reflector provided minimum improvement (0.002 mill/KWHe). A 3-inch Ni reflector resulted in 0.007 mill/KWHe savings. Choice of radial reflector material and thickness was found to have little effect on power ratios across the blanket. Nickel provided a significant improvement in flux attenuation and was selected as the preferred reflector material.

Using the BR-1 reactor, Russian experimenters (14) have studied the effect of reflector composition on radial blanket breeding. Be, C, Ni, Fe, Cu, 1 Kh 18N9T steel, water, and extended blanket material were compared. The thicknesses of these reflectors were chosen such that any further increase in thickness resulted in negligible increase in blanket $U^{238}(n,\gamma)$ captures. "Reflector efficiency" was defined as:

$$B_i = A_i / A_{xB}$$

where

A_i = additional $U^{238}(n,\gamma)$ captures resulting from addition of reflector of material i,

A_{xB} = additional $U^{238}(n,\gamma)$ captures resulting from extending the blanket.

The base radial blanket thickness was not given, nor could it be inferred. Two types of blankets – uranium carbide and metallic uranium – were used.

Table 6.1 summarizes the results. The reflector efficiency for the extended blanket case was unity, by definition. All other efficiencies were less than unity, indicating that an extended blanket is preferable if fabrication and reprocessing costs are ignored. The results show that moderating reflectors (Be, water) are significantly more effective for metallic blankets than for carbide blankets, owing to the harder spectrum in metallic blankets and the potential for improved $U^{238}(n,\gamma)$ capture. For both carbide and metallic blankets, Be is the preferred reflector.

TABLE 6.1

Effect of Radial Reflector on Radial Blanket Breeding, Russian Experimental Results (14)

Reflector Material	Reflector Thickness (cm)	Bi	
		Uranium Carbide Blanket	Metallic Uranium Blanket
Be	140	0.54	0.86
C	600	0.50	–
Ni	192	0.47	0.51
Fe	184	0.42	0.28
Steel	160	0.33	0.40
Cu	184	0.24	0.41
Water	144	0.23	0.49
UC		1.00	–
U-metal		–	1.00

The study included no analysis of the fissile revenue-fuel cycle cost tradeoff in extending the blanket. Thus, from their results, Table 6.1, it is not possible to reach a firm economic judgment vis-à-vis replacement of blanket material with reflector.

In an analytical study at M.I.T. (2), it was found that for an 18-inch blanket, no improvement in blanket breeding was accomplished by increasing the reflector (Fe) thickness beyond 18 inches. Similarly, no improvement was noted in extending an unreflected 18-inch blanket by more than an additional 18 inches, i.e., beyond a total unreflected thickness of 36 inches. Thus an 18-inch iron reflector and a 36-inch radial blanket are effectively infinite.

A German study (6) has evaluated radial reflector materials for steam-cooled FBRs. Candidate materials were steam, water, ZrH_2, BeO, graphite, steel, UO_2 (extended blanket), and U-metal. The radial blanket in all cases was 35 cm thick and composed of 56 v/o UO_2 and 18 v/o structural material. Reflectors in all cases were 80 v/o reflector material, 10 v/o steel, and 10 v/o coolant.

The reflector materials were first ranked by their effect on "breeding rate" (undefined). Optimum reflector thickness was selected such that further increase in thickness increased the breeding rate by less than 1%. Table 6.2 summarizes the results of the breeding rate ranking.

The moderating reflectors are ZrH_2, BeO, and graphite. Of these, ZrH_2 has the strongest moderating effect, but it is also the strongest absorber and thus the weakest net reflector. It has the least beneficial effect on blanket breeding. The less-thermalizing and less-absorbing BeO and graphite return more neutrons, albeit at higher energies, and result in higher blanket breeding.

The shielding effectiveness of the materials was also considered. In these studies, reflector thickness was held constant at 8 cm. Flux values (in arbitrary units) at the outer edge of the reflectors are shown in Table 6.3. If the objective is to minimize high energy flux, ZrH_2 would be the preferred reflector. The other moderating reflectors, BeO and graphite, are somewhat poorer attentuators.

TABLE 6.2

Effect of Radial Reflector on Radial Blanket Breeding, German Study (6)

Reflector Material	Optimum Reflector Thickness (cm)	B*
BeO	12-16	0.023
Graphite	12-16	0.021
Steel	6-8	0.015
UO_2	6-8	0.013
U-metal	6-8	0.013
ZrH_2	4	0.011

* B = radial breeding rate - radial breeding rate with no reflector.

TABLE 6.3

Shielding Performance of Reflectors, German Studies (6)

	Flux at Outer Edge of an 8-cm Reflector	
Reflector Material	Fast Flux 0.8-10.5 MeV (Arbitrary Units)	Total Flux 0-10.5 MeV (Arbitrary Units)
BeO	1.63	49.66
Graphite	2.68	53.30
Steel	2.77	39.14
UO_2	2.41	33.28
U-metal	2.00	25.46
ZrH_2	1.09	33.24

The breeding rate and shielding effectiveness surveys described above were based on "snapshot" multigroup physics computations. In a further study, the same author (6) evaluated the blanket revenues, with the various reflectors, at optimum irradiation times. Fabrication costs of the blanket were ignored entirely. Also, portions of the blanket which would not yield a net profit (after reprocessing) were not counted. That is, these unprofitable regions did not burden the blanket with any cost whatever; they were simply not considered to be reprocessed. Table 6.4 summarizes the percent revenue improvements (over the case with no reflector) resulting from the addition of the various reflectors. The oversimplified economic assumptions apparently account for the inconsistency in reflector rankings between Tables 6.2 and 6.4.

TABLE 6.4

Effect of Radial Reflector on Blanket Revenue, German Studies (6)

Reflector Material	Blanket Revenue Improvement with Respect to Reference*
BeO	11.6%
Graphite	12.9%
Steel	6.8%
UO_2	4.0%
U-metal	3.2%
ZrH_2	9.8%

* Reference = no reflector.

6.2.7 Metallic vs. Oxide Blankets

The economics of metallic and oxide blankets have been compared by Klickman (4). Core design was held fixed. Optimum thickness for the metallic blanket (~ 20 cm) was about one half that of the oxide blanket (~ 40 cm). For these thicknesses, the two blankets had

approximately the same breeding ratio, uranium content, and flux attenuation characteristics. Burnup limitations were assumed to be 5,000 MWD/MT for the metallic blanket and 25,000 MWD/MT for the oxide blanket. The study showed that the low burnup limitation severely disadvantages the metallic blanket – its regional optimum irradiation times cannot be achieved. The oxide blanket's irradiation time was not so-limited. Even without the burnup limitations, the oxide blanket was found to be economically preferable.

6.3 Summary

6.3.1 Objectives

As stated in the Introduction, the objectives of this work were twofold:

[1] to develop a simple depletion-economics calculational tool for survey evaluations of LMFBR blanket configurations, and

[2] to perform several comparative studies around a 1000-MWe reference LMFBR configuration.

The 1000-MWe case studies [2], to which model [1] was applied, dealt with (a) the effect of choice of radial reflector material (Be-metal vs. Na) and radial blanket thickness on radial blanket fuel economics, (b) the advantage of operating each radial blanket region on its own local optimum irradiation schedule, and (c) the sensitivity of LMFBR fuel energy costs to the economic environment.

A preliminary study examined the economic viability of FBR blankets as reactor size is increased. The reactor size-blanket economics study used only the economics equations developed in task [1] above. Depletion information was obtained from simple, one energy group, spherical geometry breeding ratio expressions. Three cases were compared over a range of core sizes: (a) a spherical core surrounded by a breeding blanket, with no fissile burnup in the blanket; (b) a spherical core surrounded by a sodium reflector (no blanket); and (c) a spherical core surrounded by a breeding blanket, with blanket burnup (power) accounted for.

6.3.2 The Depletion-Economics Model

The depletion-economics model has two parts: (a) the cost analysis model which yields the fuel components of energy cost, given unit fabrication and reprocessing costs ($/kgHM), plutonium market values ($/kg Pu_f), money costs (discount and tax rates), and the nuclide balance data; and (b) the physics-depletion model, which yields the nuclide balance data – load and discharge masses of fertile and fissile materials – used in the cost analysis model. The depletion economics model is programmed in the computer code SPPIA, described in MITNE-123. Given local physics data (local flux and flux-averaged cross sections) from a single multigroup physics computation, and given the economic parameters, the code yields fuel costs locally (or for an annular region) in $/kgHM/year, and energy costs by major region (core, axial blanket, radial blanket) in mills/KWHe.

6.3.2.1 Cost Analysis Model

Despite attempts to standardize nuclear fuel cost accounting methodology (15, 16, 17, 18), a casual review of methods actually used in design evaluations and tradeoff studies reveals substantial inconsistencies. Furthermore, FBR blankets impose several unique accounting problems: blanket fuel appreciates with irradiation, raising certain tax questions; and the long irradiation times in the radial blanket make the treatment of blanket carrying charges important. For these reasons, a cash flow method (CFM) was adopted in the present work.

A general CFM expression for the levelized cost of electricity (mills/KWHe) was derived and applied to FBR fuel costs. When applied to a region (core, axial blanket, or radial blanket) or subregion under fixed-element (batch or scatter) management, the equations reduce to forms giving local fuel economic performance, e.g., in an annular zone, or at a "point," in mills/KWHe or $/kgHM/year:

$$\bar{e} = \frac{1000}{E} M^0_{HM} \left[\frac{C_{fiss}\, \epsilon_0\, F^{mp}(T)}{T} \right. \quad \text{material purchase}$$

$$+ \frac{C_{fab}\, F^{fab}(T)}{T} \quad \text{fabrication}$$

$$+ \frac{C_{repr}\, F^{repr}(T)}{T} \quad \text{reprocessing}$$

$$\left. - \frac{C_{fiss}\, \epsilon(T)\, F^{mc}(T)}{T} \right] \quad \text{material credit} \qquad (6.1)$$

where $\bar{e}$ is the local levelized fuel component of the energy cost (mills/KWHe), E is the electrical energy produced by the reactor in one year (KWHe/yr), T is the local irradiation time (year), C_{fab} and C_{repr} are the unit fabrication and reprocessing costs ($/kgHM), C_{fiss} is the fissile plutonium price ($/kg), ϵ_0 is the initial enrichment, $\epsilon(T)$ is the discharge enrichment (kg fissile discharged per kg of heavy metal loaded), $F^q(T)$ is the carrying charge factor for cost component q, and M^0_{HM} is the mass of heavy metal loaded. The term in brackets [ ] may be regarded as a figure of merit representing local fuel economic performance, having units of dollars per year per local kilogram of heavy metal loaded.

The carrying charge factors, $F^q(T)$, are given by

$$F^q(T) = \frac{1}{1-\tau} \left[\frac{1}{(1+x)^{Tq}} - \tau \right] \quad \text{for capitalized costs or revenues}$$

$$= \frac{1}{(1+x)^{Tq}} \quad \text{for non-capitalized costs or revenues (expensed cost or taxed revenue)} \qquad (6.2)$$

where

$$x = (1-\tau) r_b f_b + r_s f_s = \text{"discount rate"} \qquad (6.3)$$

and where τ is the income tax rate, f_b and f_s are the debt and equity fractions, r_b and r_s are the debt and equity rates of return, and T^q

is the time between the cash flow transaction q and the irradiation midpoint.

The "front end" components, fabrication and material purchase, are normally capitalized. The "back end" components, reprocessing and material credit, may be capitalized or not, according to tax interpretation. If they are not capitalized, then revenue from the sale of plutonium is taxed as ordinary income, along with electricity revenue, and reprocessing charges are treated as tax deductible expenses in the year in which they occur. The two methods, capitalizing and not capitalizing back-end transactions, were compared and were found to have a significant effect on absolute values of energy costs. However, choice of method does not distort comparative or incremental results, e.g., design rankings, optimum blanket irradiation time, sensitivity studies. In the case studies to which the depletion-economics model was applied, material credit was consistently taxed and reprocessing charges were consistently expensed.

The CFM treatment of carrying charges is embodied in Equations 6.1 and 6.2 above. Two approximate methods, here labeled "Simple Interest Method" (SIM) and "Compound Interest Method" (CIM), were identified in the literature:

$$F^q = 1 + y_q T^q \tag{6.4}$$

and

$$F^q = (1+y_q)^{T^q} \tag{6.5}$$

where

$$\begin{aligned} y_q &= x/1-\tau && \text{for capitalized costs or revenues} \\ &= x && \text{for non-capitalized costs or revenues (expensed costs or taxed revenues)} \end{aligned} \tag{6.6}$$

The CFM expressions were shown, through series expansions, to reduce to SIM and CIM for small $T^q y_q$. SIM underpredicts, while CIM overpredicts, the carrying charge factor. Because radial blanket irradiation times are typically long, the CFM method was selected for use in the case studies of this report.

6.3.2.2 Physics-Depletion Model

The function of the physics-depletion model is to furnish discharge fuel composition, $\epsilon(T)$, to the cost analysis model for use in computing material credit.

In the method developed for this work, the "Semi-Analytic Method" (SAM), local physics data (fluxes and spectrum-weighted cross sections) from a single multigroup calculation are used in the analytical solutions of the reaction rate equations to obtain discharge fissile content:

$$\epsilon = \frac{M_{49} + M_{41}}{M^0_{HM}} \tag{6.7}$$

$$M_{49} = N_{49} V \frac{\tilde{M}_{49}}{N_{av}}, \quad M_{41} = N_{41} V \frac{\tilde{M}_{41}}{N_{av}} \tag{6.8}$$

$$N_{49} = N^0_{28} A \exp(-\sigma_a^{28}\theta)[1 - \exp(-(\sigma_a^{49} - \sigma_a^{28})\theta)] + N^0_{49} \exp(-\sigma_a^{49}\theta) \tag{6.9}$$

$$N_{41} = N^0_{28} A B_1 C_1 \exp(-\sigma_a^{28}\theta) - N^0_{28} A B_2 C_2 \exp(-\sigma_a^{49}\theta) + N^0_{49} B_2 C_2 \exp(-\sigma_a^{49}\theta) + \beta_1 C_3 \exp(-\sigma_a^{40}\theta) + \beta_2 \exp(-\sigma_a^{41}\theta) \tag{6.10}$$

$$A = \sigma_c^{28}/(\sigma_a^{49} - \sigma_a^{28})$$

$$B_1 = \sigma_c^{49}/(\sigma_a^{40} - \sigma_a^{28}) \qquad B_2 = \sigma_c^{49}/(\sigma_a^{40} - \sigma_a^{49})$$

$$C_1 = \sigma_a^{40}/(\sigma_a^{41} - \sigma_a^{28}) \qquad C_2 = \sigma_c^{40}/(\sigma_a^{41} - \sigma_a^{49}) \qquad C_3 = \sigma_c^{40}/(\sigma_a^{41} - \sigma_a^{40})$$

$$\beta_1 = N^0_{40} - (N^0_{28} A B_1 - N^0_{28} A B_2 + N^0_{49} B_2)$$

$$\beta_2 = N^0_{41} - (N^0_{28} A B_1 C_1 - N^0_{28} A B_2 C_2 + N^0_{49} B_2 C_2 + \beta_1 C_3) \tag{6.11}$$

$$\theta = \int^{T} \phi(T')\, dT' = \text{local flux time} \qquad (6.12)$$

M_{49}, M_{41} = discharge masses of Pu^{239}, Pu^{241}, respectively

N_{49}, N_{41} = discharge atom density of Pu^{239}, Pu^{241}, respectively

$\tilde{M}_{49}$, $\tilde{M}_{41}$ = atomic masses of Pu^{239}, Pu^{241}, respectively

N_{av} = Avogadro's number

V = volume of the zone (6.13)

Local flux and local spectrum-weighted cross sections are taken from a single multigroup physics computation and are assumed constant over a fueling cycle.

Several effects complicate the physics-depletion characteristics of FBR blankets: (1) spectrum softening with distance from the core-blanket interface; (2) spectrum hardening with irradiation time, due to the relatively large buildup of fissile plutonium in the blanket; (3) flux shift, i.e., increase in blanket flux with irradiation time, due to build-up of fissile plutonium in the blanket; and (4) heterogeneity effects occasioned by the soft blanket spectrum and aggravated, in the case of radial blankets, by larger pin diameters.

Effect (1) requires that cross sections be input to the depletion calculation with sufficient spatial detail, i.e., a separate cross section set, properly flux-weighted, for each of many blanket regions. Since the accurate spatial description of blanket physics is a prime concern in the Blanket Test Facility work, no attempt was made to determine potential savings in computational effort through reduced spatial detail. Instead, attention was concentrated on effects (2) and (3).

Effects (2) and (3) suggest that static physics calculations be performed sufficiently often, during a depletion calculation, to correct the local fluxes and cross sections. Since most of the computational effort is absorbed by the multigroup calculations, computer expense can be significantly reduced by minimizing their frequency – that is, by maximizing the irradiation time intervals over which flux shape and local

spectra are assumed constant. For this reason, studies were performed to assess the effects of item (2), spectrum hardening, and item (3), flux shift, on depletion calculation results. Qualitatively, the two effects operate in opposite directions, spectrum hardening tending to decrease blanket discharge fissile inventory, flux shift tending to increase blanket discharge fissile inventory.

Three parallel depletion calculations were performed for a reference 1000-MWe LMFBR:

(a) a 26-energy-group time step depletion calculation (26G-TSD), which accounted for both spectrum changes and flux shift;

(b) a 1-energy-group time step depletion calculation (1G-TSD), which accounted only for flux shift; and

(c) a "semi-analytic method" (SAM) calculation, which accounts for neither spectrum change nor flux shift with irradiation.

The two approximate methods, (b) and (c), used local spectrum-weighted cross sections from the initial (time zero) method (a) solution. In addition, method (c) used local fluxes from the initial method (a) solution. The computer program 2DB (19) was used for calculations (a) and (b). Method (a) used the Bondarenko 26-group cross section set (20), heterogeneity-corrected by the program 1DX (21).

The calculations assumed batch management of both core (plus axial blanket) and radial blanket. Core and axial blanket fuel was assumed replaced after two years' irradiation, corresponding to an average burnup of 100,000 MWD/MT. Radial blanket fuel was assumed irradiated to four years. The use of batch management in these calculations imposes a severe test of the constant flux, constant spectrum assumptions. For the same irradiation time, the variations of composition, flux shape, and spectra over a cycle interval are greater for batch management than for scatter management.

Principal findings of the methods study described above are listed below.

(1) For the core, the discharge fissile inventories from the three calculations were practically in exact agreement (errors less than 0.1%).

(2) For the axial blanket, 1G-TSD overpredicted discharge fissile inventory by less than 4%, while SAM underpredicted by less than 4%.

(3) For the radial blanket, 1G-TSD overpredicted discharge fissile inventory by about 10%, due to its soft cross sections. SAM underpredicted discharge fissile inventory by around 10%, in spite of its soft cross sections, because of its low flux values.

(4) Of the two effects examined in this exercise, spectrum hardening and flux shift, the latter was found to be dominant.

The SAM calculation, performed by the program SPPIA, resulted in computer time savings (over the 26G-TSD performed by 2DB) of on the order of 90%, while the 1G-TSD (2DB) led to about 60% time savings. In addition to depletion results, the SPPIA computation obtained fuel costs by region, as functions of irradiation time.

The effect of heterogeneity corrections (i.e., U^{238} resonance, spatial self-shielding) on radial blanket depletion results was examined. Heterogeneity influences blanket fissile production in two opposing ways: (a) the lower effective U^{238} microscopic capture cross section, σ_c^{28}, depresses the conversion rate, tending to decrease bred fissile inventory; (b) viewing blanket neutronics as an attenuation process, the lower σ_c^{28} results in higher blanket fluxes, tending to increase the conversion rate and bred fissile inventory. Of these two opposing effects, (a) dominates and heterogeneity leads to a net adverse effect on blanket breeding.

Two multigroup physics computations were performed using, respectively, 26-group, infinitely dilute cross sections and 26-group, heterogeneity-corrected cross sections in the blanket. Local fluxes and one-group cross sections from these two computations were then input to SAM to obtain depletion results with and without heterogeneity corrections. Comparison of the two SAM results showed that blanket heterogeneity reduced fissile discharge inventory by about 10% for irradiation times of interest (2 to 7 years). A similar study (22) showed that heterogeneity corrections for a typical LMFBR axial blanket diminished calculated axial blanket Pu^{239} discharge mass by as much as 3%.

6.3.3 1000-MWe LMFBR Case Studies

The depletion-economics model established above was applied to case studies involving radial blanket thickness, choice of radial reflector material, radial blanket fuel management, and the sensitivity of LMFBR fuel energy costs to the economic environment.

6.3.3.1 Radial Blanket Thickness and Radial Reflector Material

Combinations of three radial blanket thicknesses (15 cm, 30 cm, and 45 cm) and two radial reflector materials (sodium, beryllium-metal) were evaluated. The total radial dimension (blanket plus reflector) was held fixed at 95 cm, since even the thinnest (50 cm) reflector is effectively infinite (2, 14). The core and axial blanket configuration was also held fixed. Core volume was 4908 liters, core height-to-diameter ratio was 0.4 and the axial blanket was 40 cm thick. Core and axial blanket fuel economics were found to be insensitive to radial blanket/reflector design changes. A solid beryllium-metal reflector (no coolant, no structural material) was selected as a limiting case, i.e., as the reflector apt to provide maximum improvement in radial blanket fuel economics.

Figure 6.1 and Table 6.5 summarize the results of the blanket thickness-reflector material survey. "Reference" and "more favorable" economic environments, for radial blankets, are defined in Table 6.6. Principal findings are listed below.

1. The relative advantage of the moderating reflector, Be-metal, increases as the reflector is moved nearer the high flux zones of the blanket, that is, as the blanket thickness decreases. For a thick (45 cm) blanket, the effect of radial reflector material choice is only slight.

2. For either reflector, reducing the blanket thickness always reduces the bred plutonium inventory of the blanket; that is, the plutonium forfeited in the region eliminated is greater than the additional plutonium bred in the remaining region as a result of improvement of its breeding performance ($\overline{\sigma_c^{28}\phi}$).

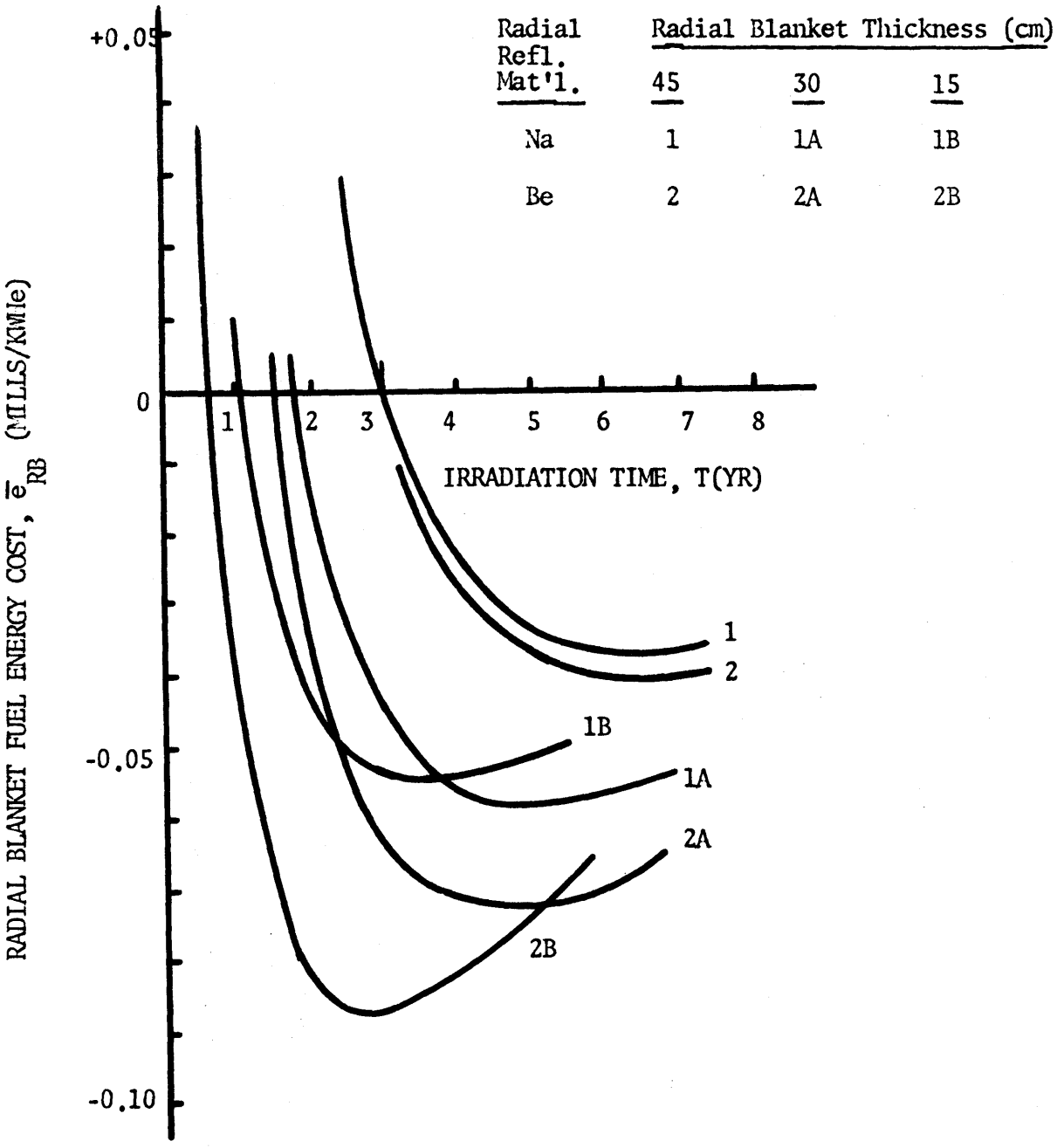

FIG. 6.1 EFFECT OF RADIAL BLANKET THICKNESS AND RADIAL REFLECTOR MATERIAL ON RADIAL BLANKET FUEL ECONOMICS

TABLE 6.5. Effect of Radial Blanket Thickness and Radial Reflector Material on Radial Blanket Fuel Economics

Configuration No.	Radial Blanket Thickness (cm)	Radial Reflector Material	M_{49}/T @T=2 yr (kg/yr)	Reference Economic Environment			More Favorable Economic Environment		
				Topt (yr)	$\bar{e}_{RB}$ @Topt (mills/KWHe)	M_{49} @Topt (kg)	Topt (yr)	$\bar{e}_{RB}$ @Topt (mills/KWHe)	M_{49} @Topt (kg)
1	45	Na	158	6-1/2	-0.037	825	3-1/2	-0.237	512
2	45	Be-metal	160	6-1/2	-0.040	845	3-1/2	-0.243	521
1A	30	Na	141	4-3/4	-0.058	596	2-1/2	-0.242	342
2A	30	Be-metal	157	4-1/2	-0.072	610	2-1/2	-0.279	380
1B	15	Na	97	3-1/2	-0.055	304	2	-0.188	194
2B	15	Be-metal	130	2-3/4	-0.087	308	1-1/2	-0.276	205

TABLE 6.6

Radial Blanket Economic Environment

	Reference Economic Environment	More Favorable Economic Environment
Fabrication, $/kgHM	69	40
Reprocessing, $/kgHM	31	31
Fissile Market Value, $/kg	10,000	20,000
Discount Rate, %	8	8

3. Optimum irradiation time decreases as the radial blanket thickness decreases and as the economic environment improves. The effect of the choice of radial reflector material on optimum irradiation time is more pronounced, the thinner the blanket.

4. Radial blanket thickness optimization is weak; that is, net blanket revenue does not display a sharp peak as radial blanket thickness is reduced from 3 rows to 2 rows to 1 row (15 cm per row). Thick blankets are indicated when fabrication and reprocessing costs decrease and/or fissile market value increases.

6.3.3.2 Advantage of Local Fuel Management

Fuel management schemes addressed in this study are characterized as "fixed fuel" schemes; i.e., fuel sees only one position in the reactor. During a refueling event, a fraction, g, of a region's fuel is discharged and replaced with fresh fuel ("scatter" management). If all of the region's fuel (g = 1.0) is replaced, the region is said to be "batch"-managed.

The entire radial blanket may be batch- or scatter-managed, in which case all fuel experiences the same irradiation time. Alternatively, the blanket may be divided into annular regions (rows), with each irradiated to its own local optimum irradiation time, again in a batch or scatter management scheme. The advantage of operating each radial blanket annular region on its own local optimum irradiation

schedule was estimated for the reference LMFBR configuration (45-cm blanket, Na radial reflector). Net radial blanket revenue in mills/KWHe was found to be about 30% higher when local management was assumed. The local optimum irradiation time ranged from 2.5 years (at the core blanket interface) to about 12 years (at the blanket-reflector interface), while the optimum irradiation time for the blanket as a whole was 6.5 years.

Another advantage of local fuel management, not quantified in the present studies, is the power-flattening effect.

6.3.3.3 Sensitivity of LMFBR Fuel Energy Costs to the Economic Environment

Costs generated throughout the fuel cycle are ultimately transferred to the utility company and borne, along with the utility company's carrying charges, by the electricity consumer via the fuel component of the levelized cost (price) of electricity in mills/KWHe. Economic environment is defined here as the unit costs for fabrication* and reprocessing ($/kgHM), the fissile Pu market value ($/kgPu fissile), and the utility company discount rate (%). The sensitivity of reference LMFBR fuel energy costs (mills/KWHe) to components of the economic environment was examined by varying each parameter around the reference values given in parentheses in Table 6.7. Sensitivity of region "s" fuel cost ($\bar{e}_s$) to cost component "q" about reference environment "o" is represented by the "sensitivity coefficient" $(A_{q,s})_o$, defined by

$$(A_{q,s})_o = (C_{q,s}/\bar{e}_s)_o \, (\partial \bar{e}_s / \partial C_{q,s}) \qquad (6.14)$$

Table 6.8 summarizes the sensitivity coefficients for the reference core, axial blanket, and radial blanket. Fabrication and reprocessing components include their respective carrying charges. The material component is the net direct fissile material cost (fissile material purchase less fissile material credit) plus the material carrying charges

* Carrying charges of the fuel cycle industries are included in their unit costs ($/kgHM). Carrying charge components of energy costs refer to utility company carrying charges.

TABLE 6.7

Ranges of Economic Environment Parameters

Unit Processing Costs [$/kgHM]	
Fabrication	
Core	150-(314)-330
Axial Blanket	20-(80)-314
Radial Blanket	20-(69)-100
Reprocessing	
Core	15-(31)- 60
Axial Blanket	15-(31)- 60
Radial Blanket	15-(31)- 60
Nuclide Market Values ($/kg)	
Fertile (C_{28}, C_{40})	0
Fissile (C_{49}, C_{41})	5000-(10,000)-25,000
Utility Company Financial Parameters	
Income Tax Rate (τ)	(0.5)
Discount Rate (x)	0.06-(0.08)-0.10

( ) indicates reference value.

TABLE 6.8

Sensitivity Coefficients, $(A_{q,s})_o^*$, for Reference LMFBR Core, Axial Blanket, and Radial Blanket

q, s	Core	Axial Blanket	Radial Blanket
Fabrication	0.357	-0.495**	-2.15**
Reprocessing	0.025	-0.140**	-0.44**
Material	0.628	1.635	+3.59
	1.000	1.000	1.00

* $(A_{q,s})_o = \dfrac{\Delta \bar{e}_s / (\bar{e}_s)_o}{\Delta C_{q,s} / (C_{q,s})_o}$

** These terms are negative because the $(\bar{e}_s)_o$ for the blankets are negative.

(inventory). For all three regions, the energy costs for fuel are seen to be most sensitive to unit fissile value and least sensitive to unit reprocessing cost.

For the core and axial blanket, irradiation time is set by the burn-up limit of the core. Thus, for these regions, Eq. 6.1 reduces to simple linear relations of the unit costs:

$$\bar{e}_s = a_{fab,s} C_{fab,s} + a_{repr,s} C_{repr,s} + a_{mat,s} C_{fiss} \qquad (6.15)$$

where

$$a_{q,s} = \frac{1000}{ET} M^0_{HM} g(T) = \text{constant.}$$

Hence, for these regions, sensitivity coefficients simply represent the fractions of the regional cost, $\bar{e}_s$, contributed by the respective components:

$$(A_{q,s})_o = \left(\frac{\bar{e}_{q,s}}{\bar{e}_s}\right)_o \qquad (6.16)$$

where

$$\bar{e}_{q,s} = a_{q,s} C_{q,s}.$$

The radial blanket energy cost of interest is the fuel cost at the optimum irradiation time, $(\bar{e}_{RB})_{T\,opt}$. Since the optimum irradiation time is an implicit function of the economic environment parameters, Eq. 6.1 for the radial blanket does not reduce exactly to a simple linear form. However, sensitivity results from the SPPIA program (Figs. 6.2, 6.3 and 6.4) showed that $(\bar{e}_{RB})_{T\,opt}$ is practically linear in C_{fab}, C_{repr}, and C_{fiss} over the expected ranges of these parameters. Thus, Eqs. 6.15 and 6.16 are applicable to the radial blanket near reference economic conditions.

Figures 6.2, 6.3, and 6.4 also show that Topt is approximately linear in C_{fab}, C_{repr}, and C_{fiss}, and that Topt decreases with improvement in the radial blanket's economic environment.

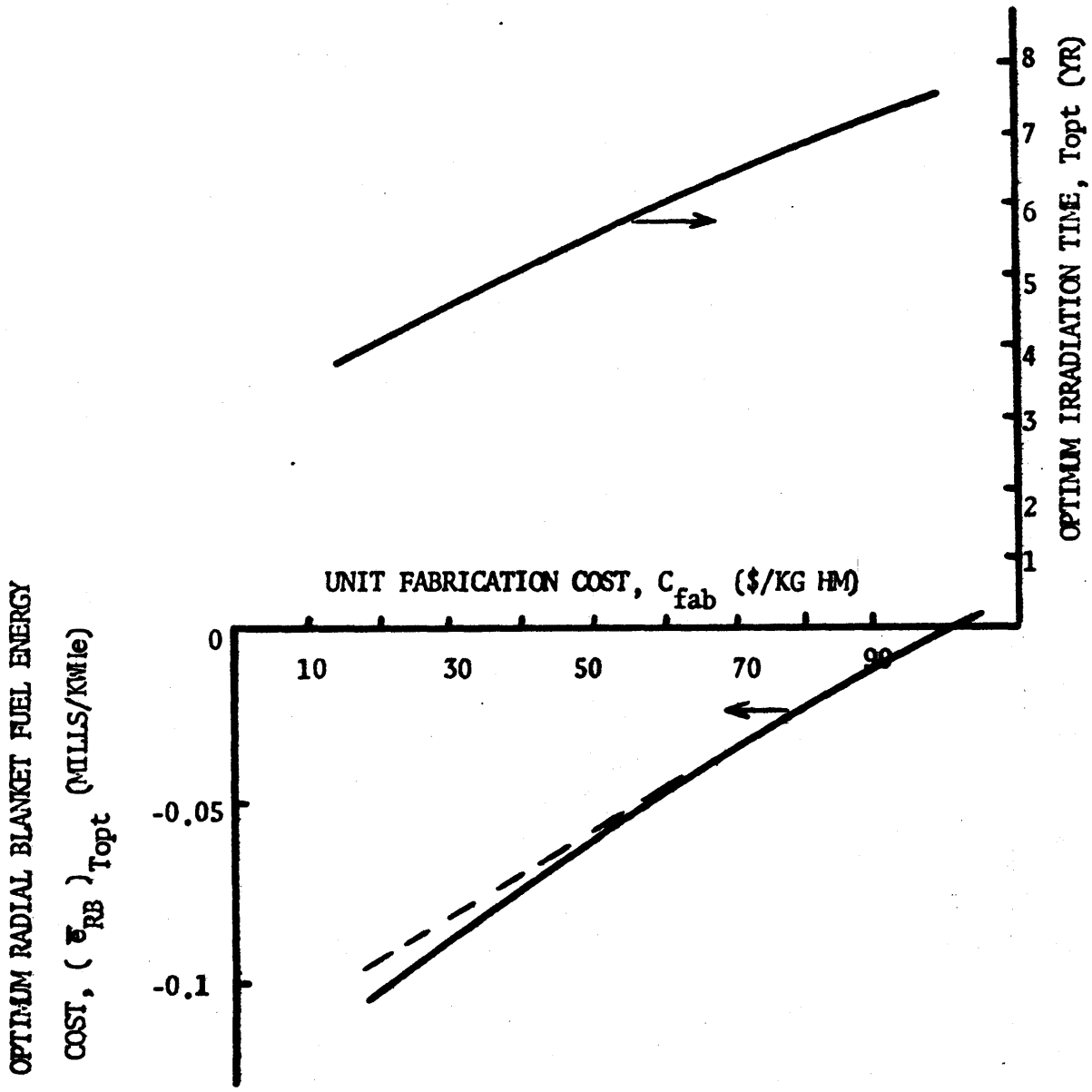

FIG. 6.2 SENSITIVITY OF OPTIMUM RADIAL BLANKET FUEL ENERGY COST TO UNIT FABRICATION COST

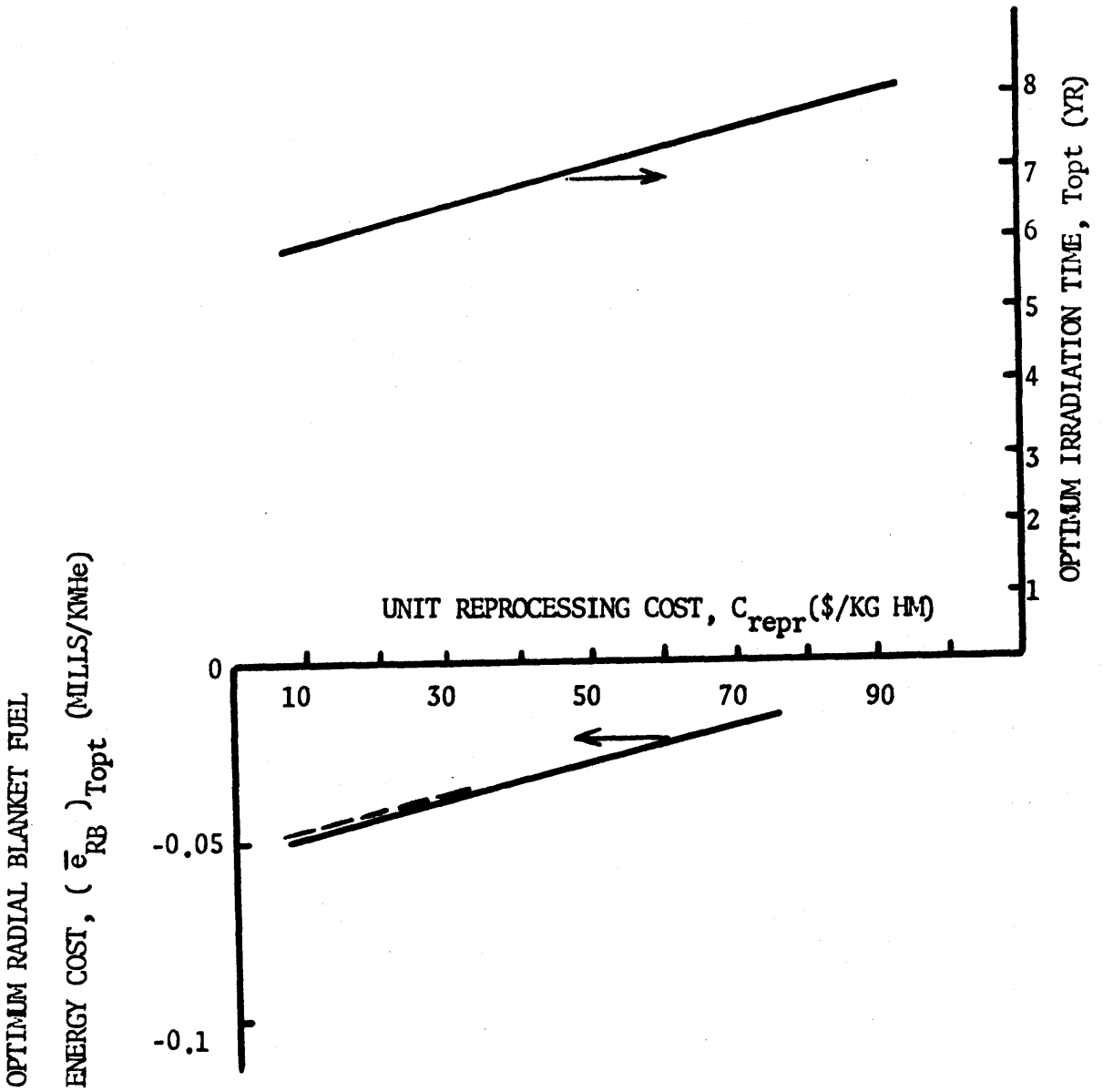

FIG. 6.3 SENSITIVITY OF OPTIMUM RADIAL BLANKET FUEL ENERGY COST TO UNIT REPROCESSING COST

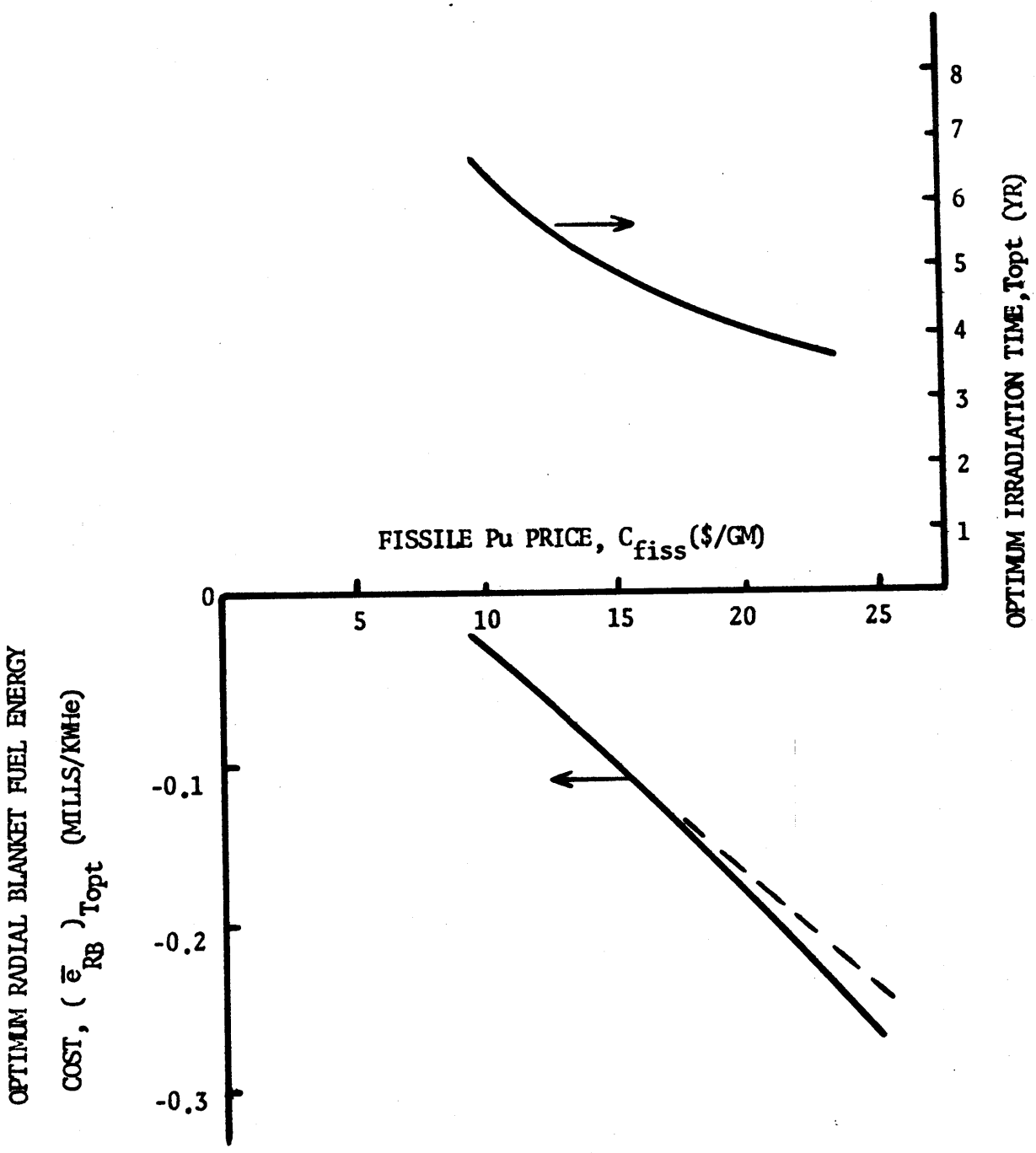

FIG. 6.4 SENSITIVITY OF OPTIMUM RADIAL BLANKET FUEL ENERGY COST TO FISSILE PLUTONIUM PRICE

Figure 6.5 shows the regional (core, axial blanket, and radial blanket) and total fuel costs as functions of fissile plutonium value. Several features are noted:

(a) Due to the core fissile inventory component, the total reactor fuel energy cost, $\bar{e}_{reactor}$, increases with C_{fiss} despite the fact that the reactor produces more fissile plutonium than it consumes.

(b) The axial blanket is more profitable than the radial blanket because the axial blanket sees more neutrons in this particular, but typical, design (H/D = 0.4).

(c) The axial blanket breakeven point occurs at about 3.9 $/gm.

(d) The radial blanket breakeven point occurs at about 7.25 $/gm.

(e) As fissile price increases, the blankets become more viable, substantially offsetting the higher core inventory costs.

It is unlikely that the disparity between axial blanket profit and radial blanket profit would be diminished significantly by reasonable changes in the thickness or composition of either blanket. The axial blanket advantage is largely inherent: the axial blanket enjoys a higher flux and higher fissile generation rate per unit of heavy metal loaded, and a short optimum irradiation time close to that set by the core burnup limit (2 years). Hence, axial blanket fissile credit is not threatened by overwhelming processing and material carrying charges.

6.3.4 Reactor Size and Blanket Fuel Economics

A semiquantitative scoping study was performed to examine the effect of reactor unit rating on the economic viability of blankets. As core size increases (holding core shape fixed), core fuel economics improve due to the decreased critical enrichment and increased internal breeding ratio. At the same time, core surface-to-volume ratio and external breeding ratio diminish, and blanket fuel economics degenerate.

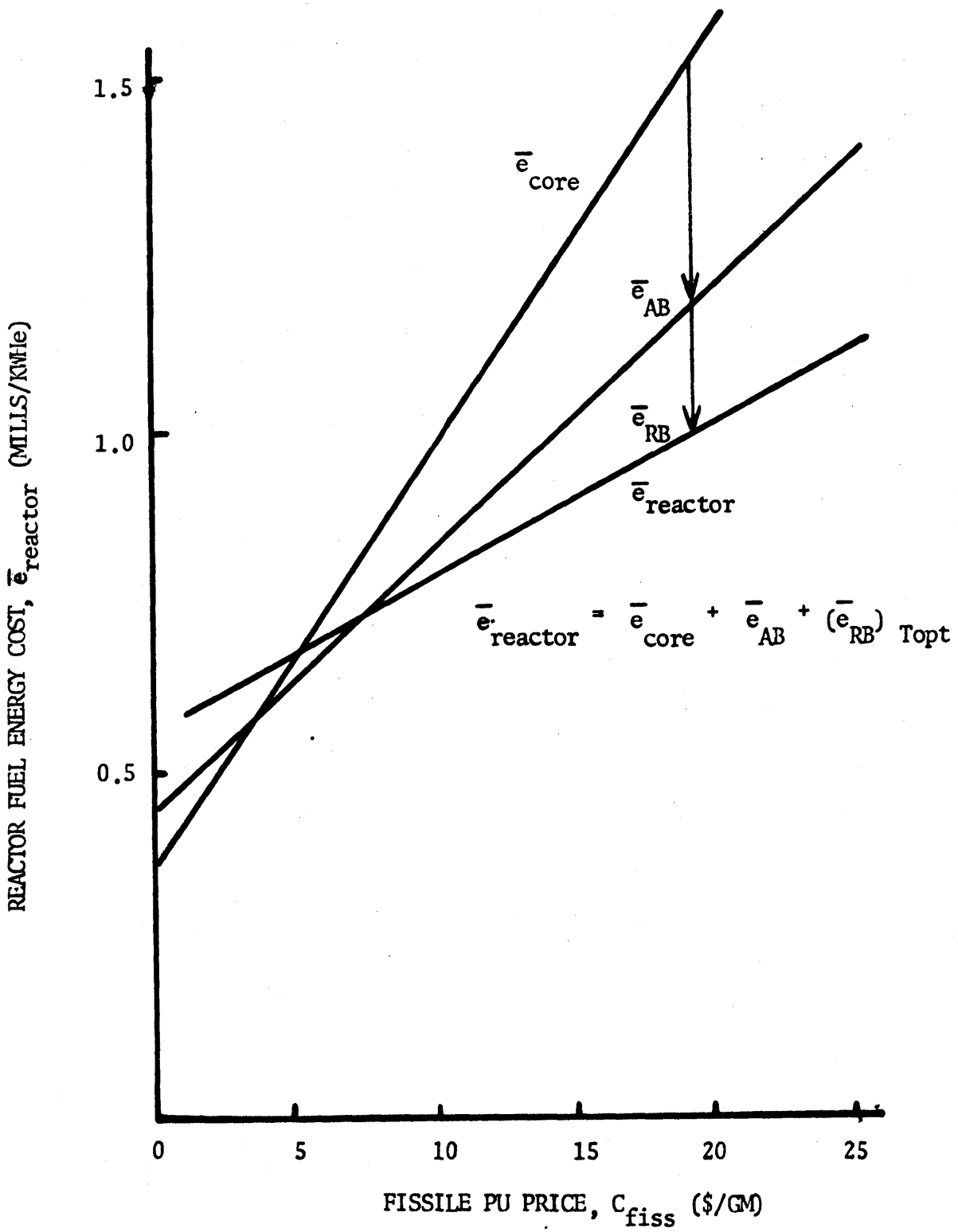

FIG. 6.5 EFFECT OF FISSILE PU PRICE ON TOTAL REACTOR FUEL ENERGY COST

All of the major assumptions in this preliminary study penalized the blanket. A spherical core was assumed throughout the range of core size; that is, core geometry spoiling to maintain negative sodium void coefficients was not accounted for. A one-zone core was assumed, whereas a graded enrichment scheme would have enhanced blanket economics. The increased control requirements and associated costs, involved in increasing the internal breeding ratio much above unity, were ignored.

Figure 6.6 shows that in spite of these (and other) penalties, the blanket concept is economically preferable to a nonbreeding reflector (Na) for reactor ratings well over 1000 MWe. Beyond the "indifference point," the advantage of the "no-blanket" configuration is only very slight. Thus, it is likely that blankets will remain an important part of LMFBR design for the foreseeable future.

6.4 Conclusions and Recommendations

The most significant findings and recommendations are summarized in the following paragraphs.

Choice of fuel cost accounting method has a significant effect on absolute values of energy costs (mills/KWHe) but does not distort comparative and incremental results, design rankings, optimization of fuel residence times, etc. Choice of taxing method can, however, affect the optimized thickness of blankets.

A single, multigroup physics computation, to obtain the flux shape and local spectra for depletion calculations, is sufficient for evaluating blanket/reflector design changes and for scoping and sensitivity studies. The major source of error in depletion results is the assumption of constant local flux over an irradiation cycle.

Choice of radial reflector material is important for radial blankets of one or two rows of subassemblies (15 to 30 cm). The relative advantage of a moderating reflector increases as the reflector is moved nearer the high flux zones of the blanket – that is, as the blanket thickness decreases from three (45 cm) rows to two (30 cm) rows to one (15 cm) row of subassemblies.

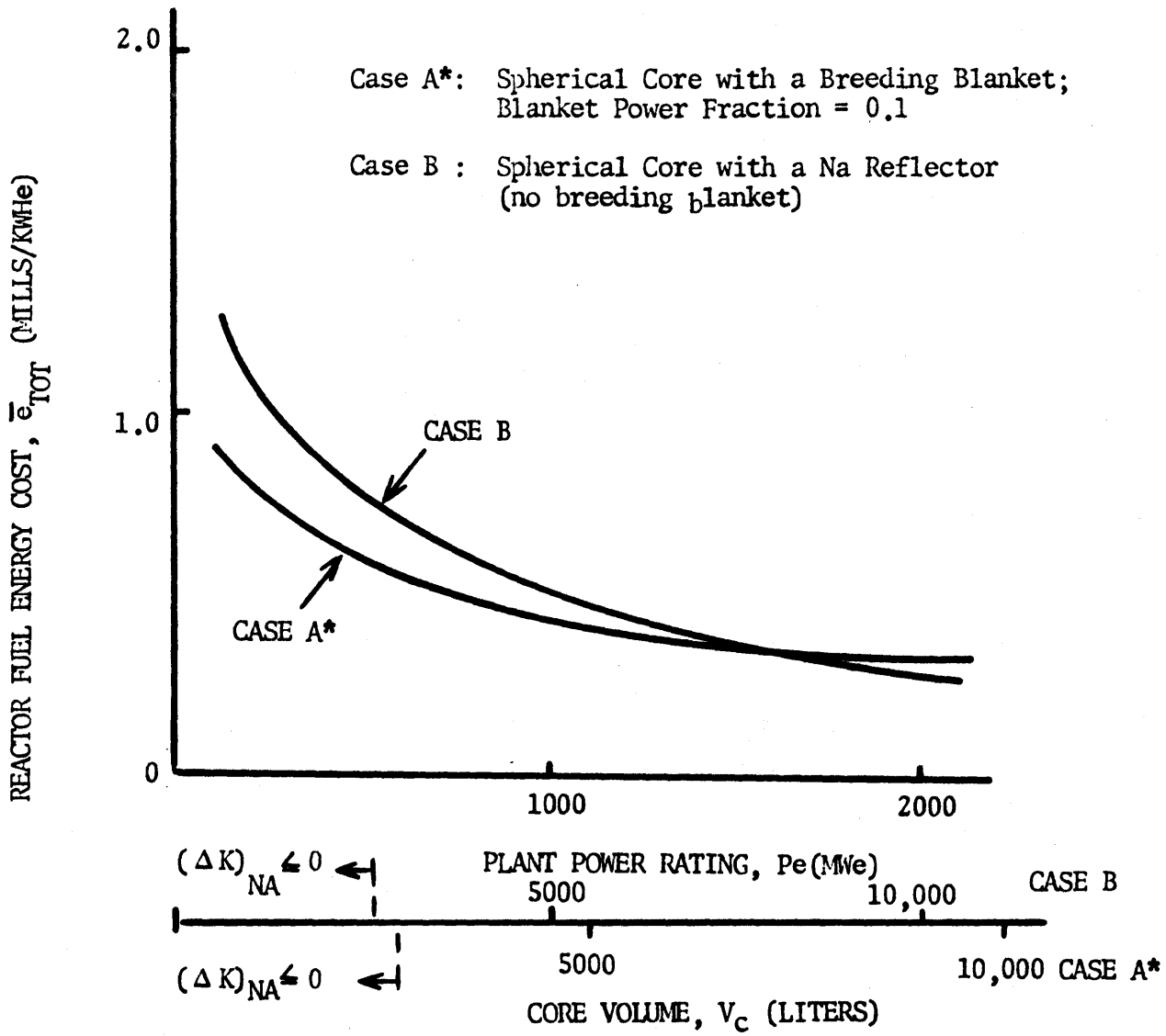

FIG. 6.6 REACTOR FUEL ENERGY COSTS WITH AND WITHOUT A BREEDING BLANKET

Radial blanket thickness optimization is weak; i.e., net blanket revenue does not display a sharp peak as radial blanket thickness is reduced from three rows to two rows to one row. Significant improvement (~30% increase in net blanket revenue) results from irradiating each radial blanket region to its own, local optimum irradiation time.

Both the optimum radial blanket irradiation time and the corresponding radial blanket net revenue are approximately linear functions of the unit costs in dollars per kilogram for fabrication, reprocessing, and fissile material. For increased fissile costs, both blankets (axial and radial) become more important in offsetting the increased core fissile inventory costs.

Based on a simple examination of reactor size versus blanket fuel economics, blankets are expected to remain an important part of LMFBR design for the foreseeable future.

Fast breeder reactor blanket design and fuel management has not received attention, in the open literature, commensurate with its importance. Design and fuel management study results tend to be highly specialized and fragmentary, making normalizations and comparisons difficult. A comparative evaluation of scatter, batch, out-in, and in-out equilibrium radial blanket fuel management schemes, for a fixed reactor configuration, is recommended.

The flexibility of radial blanket fuel management, after the reactor is in operation, presents the opportunity of optimizing reload strategies in accordance with the current and projected economic environments. Further effort in this area is recommended.

Interactions between engineering design and fuel management parameters should be examined with the aim of better understanding and characterizing the blanket. Radial blanket fuel management directly influences the degree of power flattening across the blanket, the power swing over an irradiation cycle, and the core-blanket power split. The associated economic tradeoffs are not well understood. In particular, an analysis of the benefits and penalties of blanket fissile seeding is recommended.

In brief, the most important recommendation is that, whatever aspects of blanket fuel management are subjected to further scrutiny,

this be done on a more global basis, at the minimum taking into consideration the strong interaction of management schemes and the flow orificing pattern adopted.

Since unit sizes are projected to increase to 2000 MWe and beyond after the year 2000, a more thorough parametric study of blanket performance versus reactor rating is recommended.

6.5 References

(1) Forbes, I.A., "Design, Construction, and Evaluation of a Facility for the Simulation of Fast Reactor Blankets," MIT-4105-2, MITNE-110 (February 1970).

(2) "LMFBR Blanket Physics Project Progress Report No. 1," Massachusetts Institute of Technology, MIT-4105-3, MITNE-116 (June 30, 1970).

(3) Westinghouse 1000-MWe LMFBR Follow-On Studies

"1000-MWe LMFBR Follow-On Study. Task I. Final Report," WARD-2000-33 (June 1968).

"1000-MWe LMFBR Follow-On Study. Task I. Topical Report. Moisture Separation or Steam Reheat vs. Sodium Reheat. Plant Cycle Technical and Economic Evaluation," WARD-2000-20 (April 1968)

"1000-MWe LMFBR Follow-On Study. Task I. Topical Report. Steam Generator Concept Selection," WARD-2000-22 (January 1968).

"1000-MWe LMFBR Follow-On Study. Task I. Topical Report. Survey of State-of-the-Art of Intermediate Heat Exchanges," WARD-2000-23 (March 1968).

"1000-MWe LMFBR Follow-On Study. Task I. Topical Report. Evaluation of Vented-to-Coolant Design for Sodium-Bonded Carbide Fuel Rods," WARD-2000-31 (February 1968).

"1000-MWe LMFBR Follow-On Study. Task V Report. Safety Studies," WARD-2000-84 (December 1968).

(4) Klickman, A.E., et al., "The Design and Economic Evaluation of Fixed Blankets for Fast Reactors," APDA-156 (August 1963).

(5) Hasnain, S.D., and D. Okrent, "On the Design and Management of Fast Reactor Blankets," NSE, 9, 314-322 (1961).

(6) Mayer, L., "Blanketoptimierung am Beispiel eines dampfgehuhlten Schnellen Brutreaktors," Nukleonik 11, 193 (1968).

(7) Atomics International 1000-MWe LMFBR Follow-On Studies

"ANL 1000-MWe LMFBR Follow-On Study Task I Report," Vols. 1 and 2, AI-AEC-12765 (rev.) (May 1968).

"1000-MWe LMFBR Follow-On Study Task II Report – Conceptual Systems Design Descriptions," Vols. I, II, III, AI-AEC-12791 (May 1969).

"1000-MWe LMFBR Follow-On Study Task III – Conceptual Design Report," Vols. I, II, III, IV, V, AI-AEC-12792 (June 1969).

"1000-MWe LMFBR Follow-On Study Task IV Report – Research and Development Requirements," AI-AEC-12793 (June 1969).

(8) Babcock and Wilcox 1000-MWe LMFBR Follow-On Studies

"1000-MWe Follow-On Study Task I Report," BAW-1316
- Vol. 1. Task I Report (June 1967)
- Vol. 2. Task I Concept I System Description Report (April 1967)
- Vol. 3. Task I Concept II System Description Report (June 1967)
- Vol. 4. Task I Concept III System Description Report (July 1967)
- Vol. 5. Task I Concept IV System Description Report (August 1967)

"1000-MWe LMFBR Follow-On Study Task II and III Final Report," BAW-1328
- Vol. 1. Summary Description and Cost Estimate (February 1969)
- Vol. 2. Conceptual System Design Description (March 1969)
- Vol. 3. Conceptual System Design Description (February 1969)
- Vol. 4. Trade-Off Studies (November 1968)
- Vol. 5. Parametric Studies (January 1969)

"1000-MWe LMFBR Follow-On Study – Control Studies," BAW-1330 (December 1968).

"Sodium Parameter Study Code NAPS – Topical Report," BAW-1326 (April 1968).

"1000-MWe LMFBR Follow-On Study – Task IV Final Report – Research and Development Requirement," Vols. I and II, BAW-1331 (June 1969).

(9) Combustion Engineering 1000-MWe LMFBR Follow-On Studies

"1000-MWe LMFBR Follow-On Study. Task I Report. Preliminary Studies for a Reference Conceptual Design," CEND-322 (December 1967).

"1000-MWe LMFBR Follow-On Study. Task II and III Report. A Conceptual Design," CEND-337
Vol. I Conceptual System Design Descriptions (July 1968)
Vol. II Static Design and Performance Analysis (May 1968)
Vol. III Safety and Control Analyses (September 1968)

"1000-MWe LMFBR Follow-On Study. Task IV Report. A Research and Development Program Needed for the CE Reference Concept," CEND-346 (February 1969).

(10) General Electric 1000-MWe LMFBR Follow-On Studies

"Comparison of Two Sodium-Cooled, 1000-MWe Fast Reactor Concepts. Task I Report of 1000-MWe LMFBR Follow-On Work," GEAP-5618 (June 1968).

"Conceptual Plant Design, System Descriptions, and Costs for a 1000-MWe Sodium-Cooled Fast Reactor. Task II Report of 1000-MWe LMFBR Follow-On Work," GEAP-5678 (September 1968).

"Methods System Optimization, and Safety Studies for a 1000-MWe Sodium-Cooled Fast Reactor. Task III and V Report of 1000-MWe LMFBR Follow-On Work," GEAP-5710 (February 1969).

"Research and Development Requirements for a 1000-MWe Sodium-Cooled Fast Reactor. Task IV Report of 1000-MWe LMFBR Follow-On Work," GEAP-5769 (April 1969).

(11) Maeder, C., "Optimization of Gas-Cooled Fast Reactor Blankets," NSE 42, 89-111 (1970).

(12) Elias, D. and F.J. Munno, "Reactor Fuel Management Optimization in a Dynamic Environment," Nuclear Technology 12 (September 1971).

(13) Perks, M.A. and R.M. Lord, "Effects of Axial and Radial Blanket Design on Breeding and Economics," Proceedings of the Conference on Breeding, Economics and Safety in Large Fast Power Reactors, Argonne, Illinois, ANL-6792 (December 1963).

(14) Golubev, V.I., M.N. Nikolaev, et al., "The Effect of Reflectors Made of Various Materials on the Increase in the Number of Neutron Captures in the Uranium Blanket of a Fast Reactor," Soviet Atomic Energy 15, No. 4 (October 1963).

(15) "Guide for Economic Evaluation of Nuclear Reactor Plant Designs," NUS Corporation, NUS-531 (January 1969).

(16) "Guide to Nuclear Power Cost Evaluation," USAEC, TID-7025 (March 1962).

(17) "A Uniform Procedure for Use in the Evaluation of Nuclear Power Reactors," Atomic Industrial Forum (September 1959).

(18) Dragoumis, P. et al., "Estimating Nuclear Fuel-Cycle Costs," Nucleonics (January 1966).

(19) Little, W.W. and R.W. Hardie, "2DB User's Manual – Revision No. 1," BNWL-831, Battelle Northwest Laboratory (August 1969).

(20) Bondarenko, I.I., et al., "Group Constants for Nuclear Reactor Calculations," Consultants Bureau, New York (1964).

(21) Little, W.W. and R.W. Hardie, "1DX, A One-Dimensional Diffusion Code for Generating Effective Nuclear Cross Sections," BNWL-954, Battelle Northwest Laboratory (March 1969).

(22) Hirons, T.J. and R.E. Alcouffe, "Heterogeneity Effects on Large Fast Breeder Fuel Cycle Calculations," Trans ANS 13, 1 (June 1970).

7. ANALYSIS OF ADVANCED BLANKET DESIGNS

7.1 Introduction

Work has recently been initiated in three areas, involving evaluation of:

(1) the effects of variations in blanket and reflector composition,
(2) the advantages of the use of an interior blanket, the so-called parfait blanket concept, and
(3) the economic benefits which may be achieved through use of thorium in place of depleted uranium in LMFBR blankets.

Since this work is still in its early stages, we will merely describe the underlying motivation and outline the projected scope of the research in the successive sections of this chapter.

7.2 Variations in Blanket Composition

This investigation is in large measure an outgrowth of previous work described in a forthcoming topical report (1). Major objectives will be evaluation of the economic advantages of the use of high-albedo reflectors, blanket pre-enrichment and power flattening in the radial blanket. The economic analysis developed in reference (1) will be expanded to consider the thermal-hydraulic aspects of blanket design, which have been treated in preliminary fashion in reference (2). In addition, gamma heating – which can be an important contributor to blanket power, particularly in the outermost row – will be analyzed.

7.3 The Parfait Blanket

Although the primary emphasis of the work conducted under the aegis of the MIT Blanket Research Project has been on the external axial and radial blankets typical of present LMFBR designs, preliminary studies have identified one unconventional internal blanket configuration which merits further investigation: the totally enclosed or

parfait blanket concept. As shown in Fig. 7.1, the parfait blanket is surrounded both axially and radially by core.

Preliminary calculations indicate the following potential advantages of the parfait blanket design over a conventional LMFBR core:

(1) decreased reactivity swing over lifetime due to the presence of bred plutonium in a high worth central position,
(2) better axial and radial power flattening with no sacrifice of subassembly power equalization over core lifetime,
(3) lower peak flux due to higher fissile loading in core zones surrounding the blanket, hence the possibility of reduced stainless steel swelling,
(4) the potential of selecting blanket size to permit use of a single fissile enrichment in the two core zones.

Potential disadvantages identified to date, which do not appear to be serious, are:

(1) less flexible fuel management (e.g., out-in movement between core zones is precluded) which may be acceptable if the present trend toward region scatter management for LMFBR's continues,
(2) slightly higher clean critical mass before (and perhaps after) burnup effects have been taken into account,
(3) a larger positive component for the whole-core sodium void reactivity (but smaller for voiding at the core hot spot),
(4) a large power density discontinuity in the fuel rod at the core-blanket interface, somewhat larger than that at the core-axial blanket interface.

Work is planned to quantify these varied factors and, in particular, to translate them into economic terms to permit a detailed comparison between the parfait and conventional designs.

7.4 Thorium in LMFBR Blankets

The final area in which it was thought that major innovations in blanket design may occur involves the use of thorium in place of uranium as blanket fertile species. The motivation for this choice

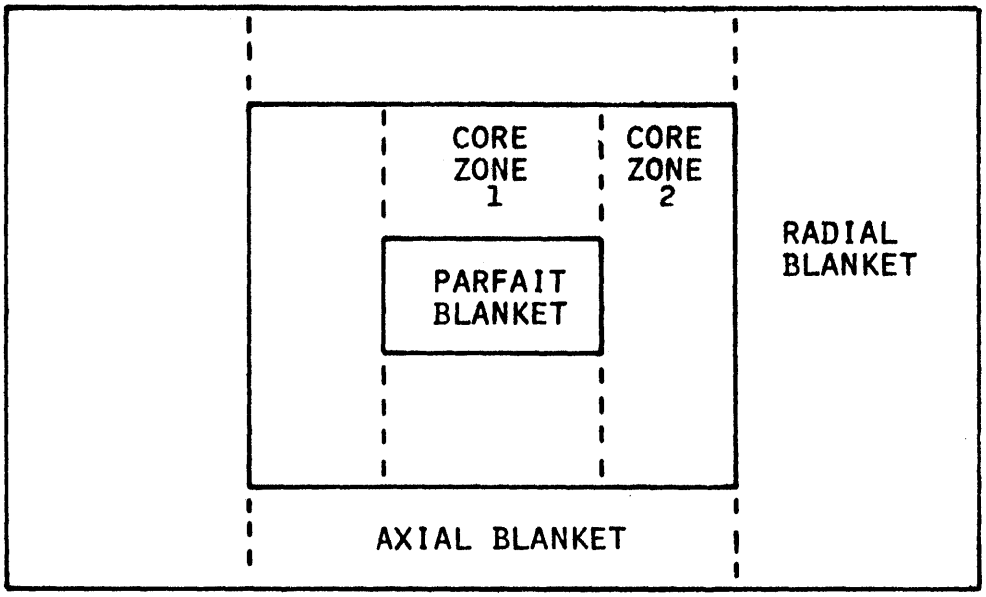

VERTICAL CROSS SECTION THROUGH CYLINDRICAL CORE

FIG. 7.1 THE PARFAIT BLANKET CONFIGURATION

has become more substantial in the past year with the increasing penetration of the U.S. power reactor market by the HTGR. Roughly speaking, U^{233} is worth a factor of two more than Pu^{239} as HTGR fuel. Thus it is at least superficially attractive to breed U^{233} in LMFBR blankets for sale to HTGR operators, and to purchase make-up plutonium for the LMFBR from LWR operators. The resulting fuel cycle economy of all three reactor types may in turn encourage more rapid adoption of the LMFBR by the utility industry.

This evaluation will include a parallel economic comparison between U^{238} and Th^{232} blankets using many of the tools developed in reference (1).

7.5 Discussion

Although the work described in this chapter will primarily involve application of computer-oriented tools such as the economic models of reference (1) and the 2-DB burnup code, close integration with the experimental program, which is the major focus of project effort, is being enforced. For example, the overall study of composition variation discussed in section 7.2 is being carried out in conjunction with the experiments on Blanket No. 3, reported in Chapter 4, which are designated to verify physics design calculations for advanced blanket designs employing high-albedo reflectors: both phases of the work will be reported in the same topical report. Similarly, irradiations in Blanket No. 4 will include as many thorium capture and fission traverses as practicable to provide direct experimental confirmation of the numerical computations used in the remainder of the study.

7.6 References

(1) Brewer, S.T., E.A. Mason and M.J. Driscoll, "The Economics of Fuel Depletion in Fast Breeder Reactor Blankets," COO-3060-4, MITNE-123 (November 1972, est.).

(2) Brown, G.J., "A Study of High-Albedo Reflectors for LMFBR's," S.M. Thesis, M.I.T. Nuclear Engineering Department (March 1972).

8. PARAMETRIC STUDIES

8.1 Introduction

A considerable number of parametric and sensitivity studies have been performed as part of the effort required to design and analyze the experiments. It is convenient to arrange the discussion according to the particular blanket mock-up which served as the base-case computer model, even though many of the conclusions are more generally applicable. Unless otherwise specified, all calculations were made using the ANISN program in the S_8 option, and the ABBN 26-group cross section set.

8.2 Studies Involving Blanket No. 2

The following variations have been investigated:

(1) Blanket No. 2 driven by two different "cores": the ZPPR-2 core and the MIT BTF converter plate.

(2) Blanket No. 2 using two different cross section sets: the ABBN 26-group set and a HEDL 29-group set.

(3) Comparison of Blanket No. 2 to Demonstration and 1000-MWe LMFBR's.

Figure 8.1 compares the spectrum calculated at the center of Blanket Mock-Up No. 2 to the expected spectrum if the same blanket were driven by the ZPPR-2 core.* As can be seen, the BTF-driven mock-up has a softer spectrum. One consequence of this spectral difference can be seen in the calculated U^{238} capture traverses of Fig. 8.2, in which the softer BTF driver produces an enhancement in the first half of the blanket. As will be discussed subsequently, the above observations are part of the justification for selecting hardened driver spectrum as the governing criterion for designing Mock-Up No. 4.

---

*Note that although the driver is being compared to the ZPPR-2 core, the MIT Blanket No. 2 is not intended to mock up ZPPR-2 blankets.

FIG. 8.1 SPECTRUM AT CENTER OF RADIAL BLANKET MOCKUP NO. 2

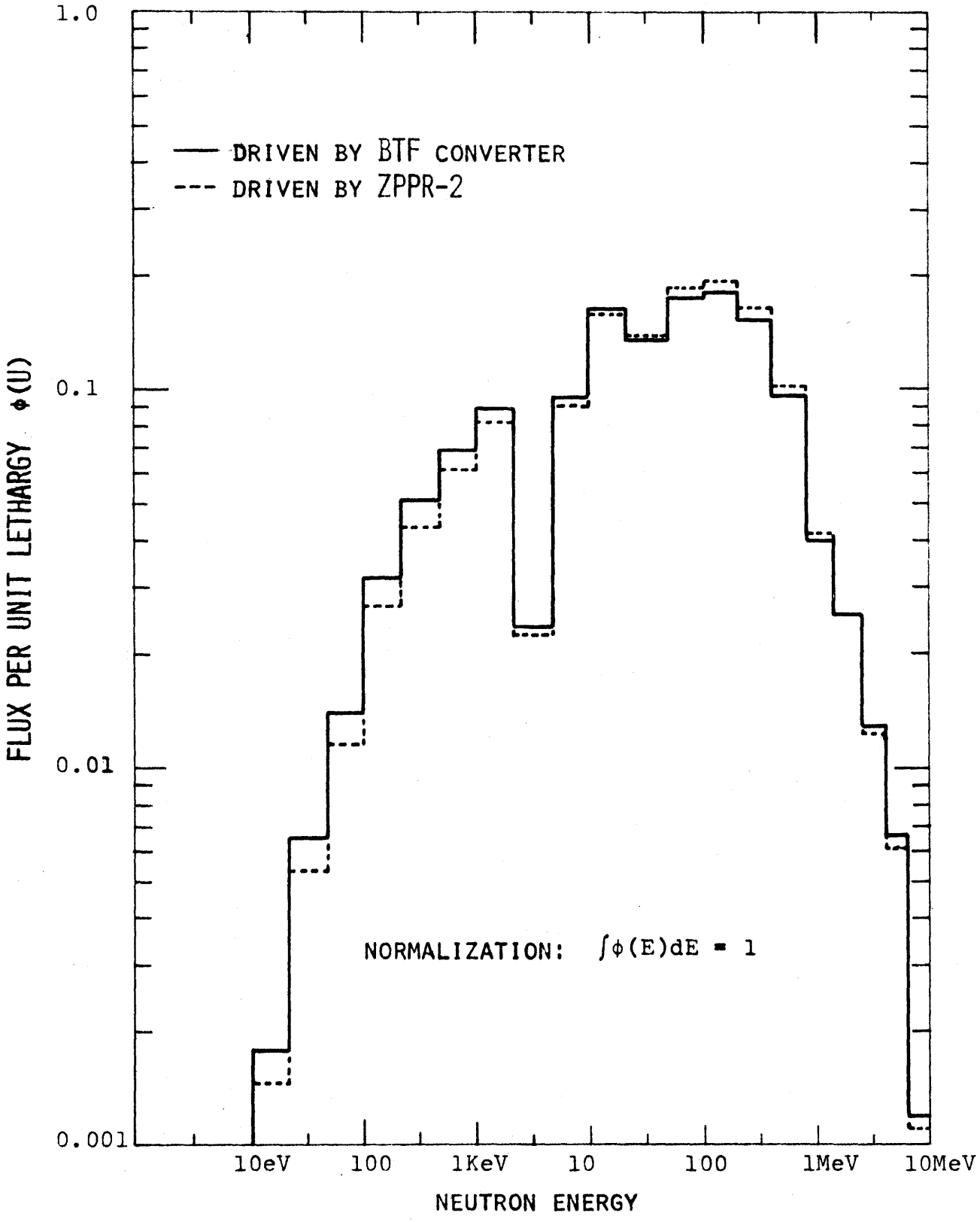

FIG. 8.2 U-238 CAPTURE RATE IN MOCKUP NO. 2 BLANKET AND REFLECTOR (EX-ROD FOILS)

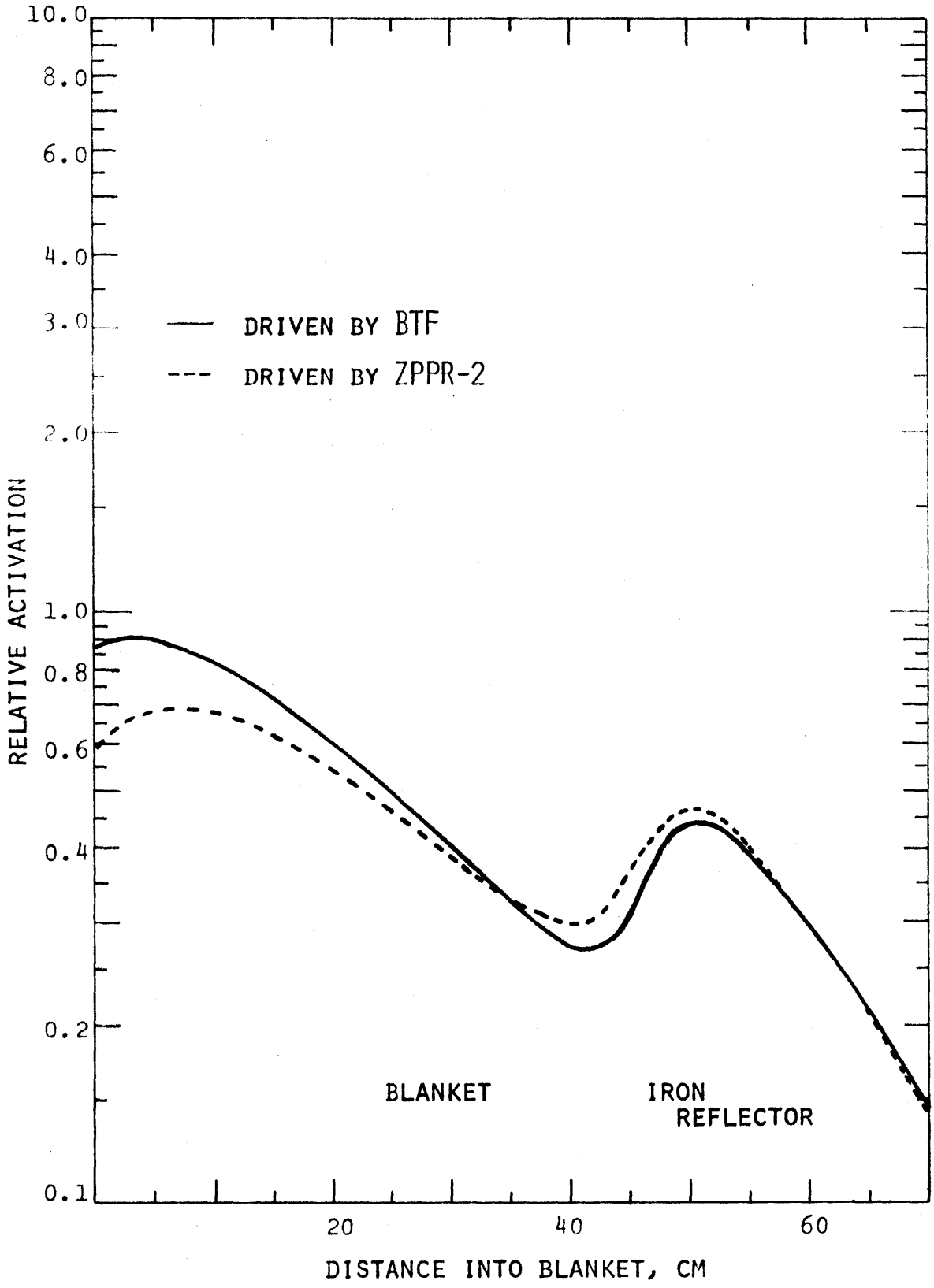

The second category of parametric studies carried out on Mock-Up No. 2 is of particular interest in that two different cross section sets were employed. Although the Hansen-Roach 16-group set was used in the very early stages of the initial design of the BTF, the ABBN or Russian 26-group set (1) has been the standard for essentially all of the work carried out to date within the MIT Blanket Research Project. In the present group of comparisons, a set obtained from HEDL (2), which was developed from ENDF/B data, was compared to the ABBN set. In order not to confuse the issue, infinite dilution U^{238} cross sections were used. Figure 8.3 shows the spectrum at the inner edge of the blanket, while Figs. 8.4 and 8.5 show U^{238} capture and fission traverses. The overall agreement is quite good, from which the tentative conclusion may be drawn that errors in cross section sets would have to arise from a common source in data or processing if such errors are to explain discrepancies between calculated and measured results. For example, both sets yield roughly comparable slopes for the U^{238} fission traverse in the iron reflector, and thus both are in major disagreement with the measured slope. From other work, it is also clear that specification of the U^{238} self-shielding is the single most important cross section variation: the previous parametric studies reported by Leung (3) show that substantial changes in the calculated activation traverses can be thereby effected. Another tentative conclusion suggested by the present results is that it would be difficult to use blanket measurements to justify selecting between cross section sets except with regard to the specific foil reactions themselves: one could not, for example, justify arbitrary adjustment of the U^{238} inelastic cross sections to force better agreement. On the other hand, calculations for single component bulk media such as the iron reflector do show more significant differences which might be interpretable in terms of cross section discrepancies of the medium itself.

The last group of intercomparison studies deals with the effect of reactor core size on the blanket. Figure 8.6 shows the variation in driving spectrum between demo-size and 1000-MWe cores: the differences are small but not negligible, and, as expected, the smaller core

FIG. 8.3 SPECTRUM AT INNER EDGE OF RADIAL BLANKET FOR DIFFERENT σ-SETS

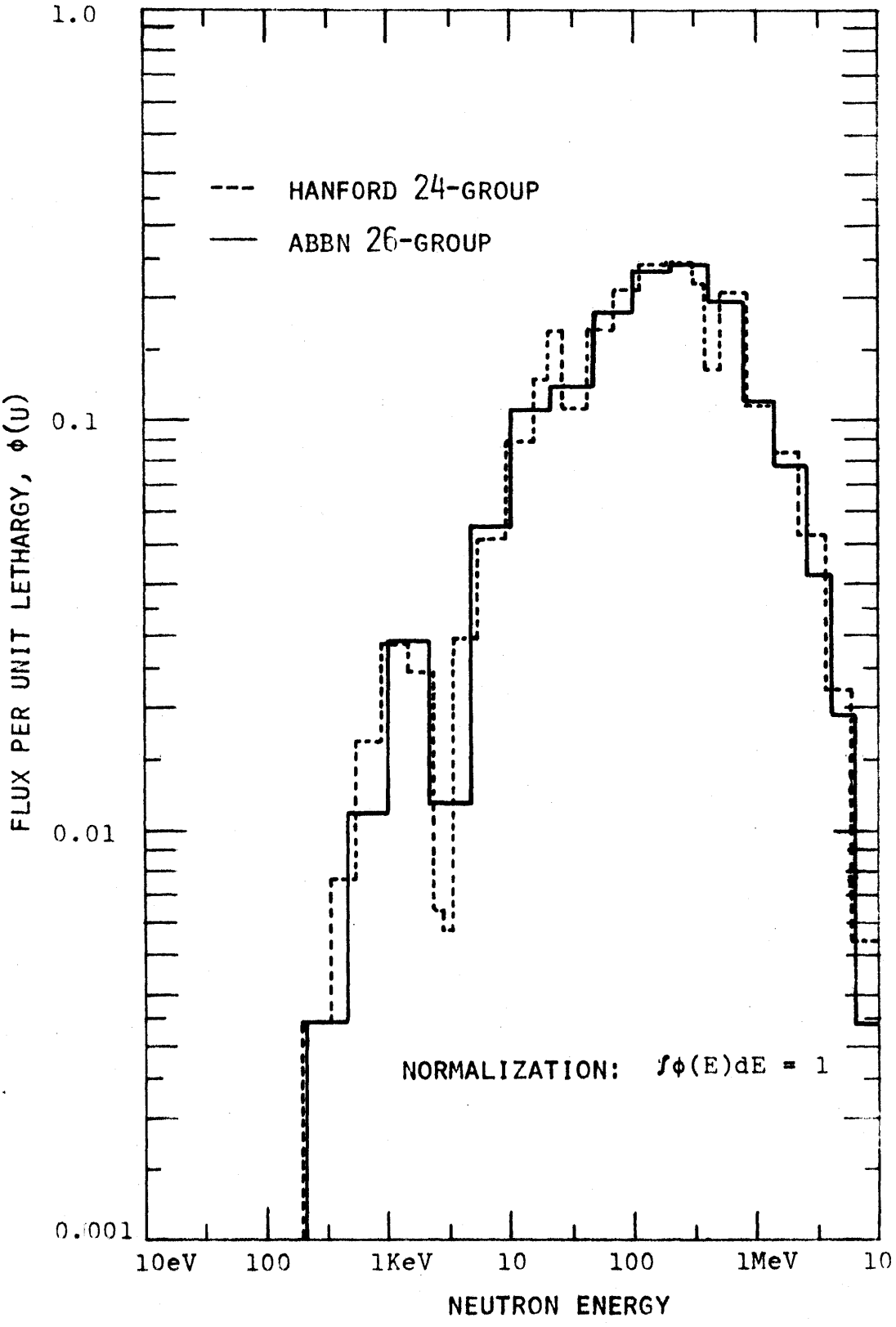

FIG. 8.4 U-238 CAPTURE RATE IN BLANKET AND REFLECTOR FOR DIFFERENT σ-SETS

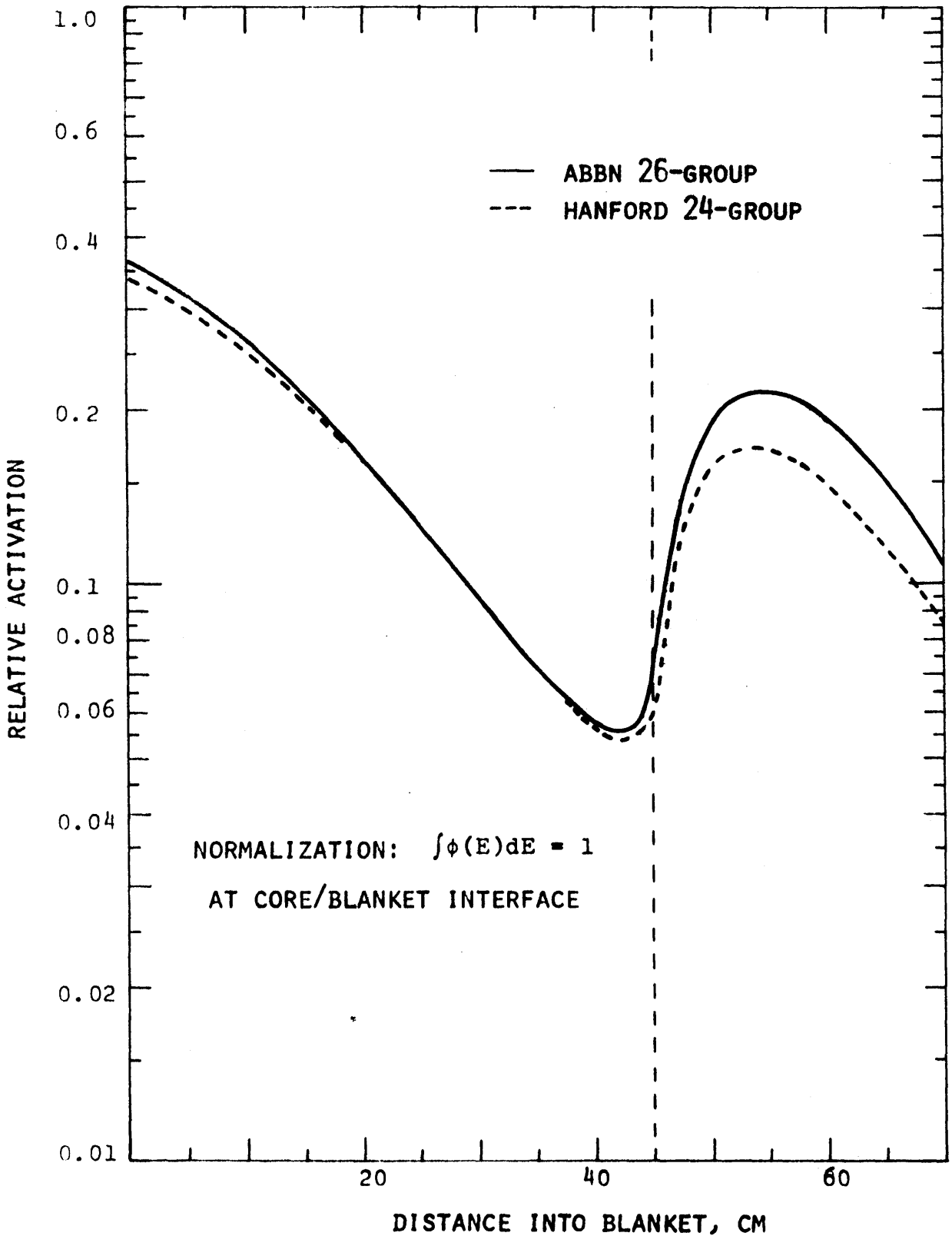

FIG. 8.5 U-238 FISSION RATE IN BLANKET AND REFLECTOR FOR DIFFERENT σ-SETS

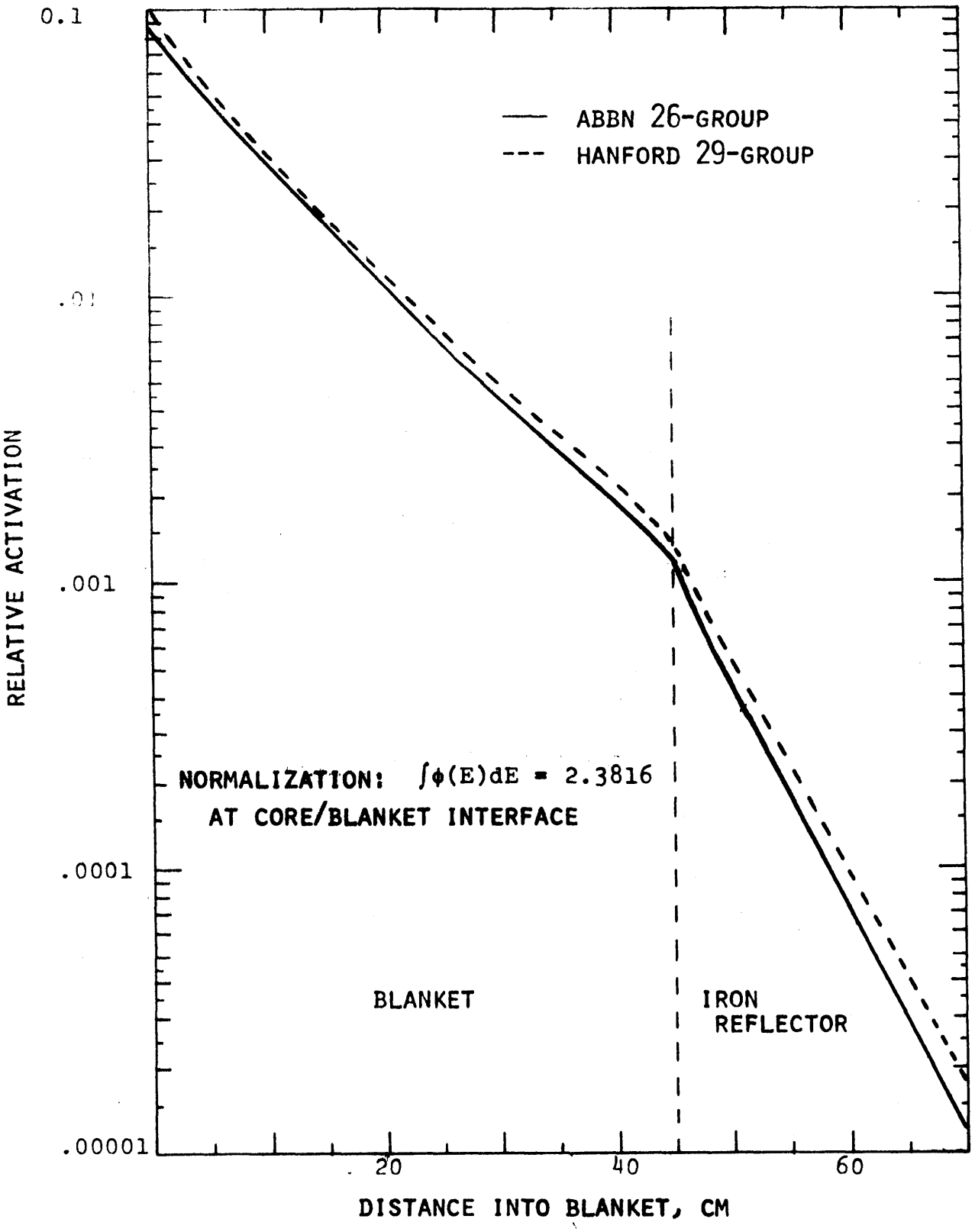

FIG. 8.6 SPECTRUM AT INNER EDGE OF RADIAL BLANKET FOR DIFFERENT LMFBR CORES

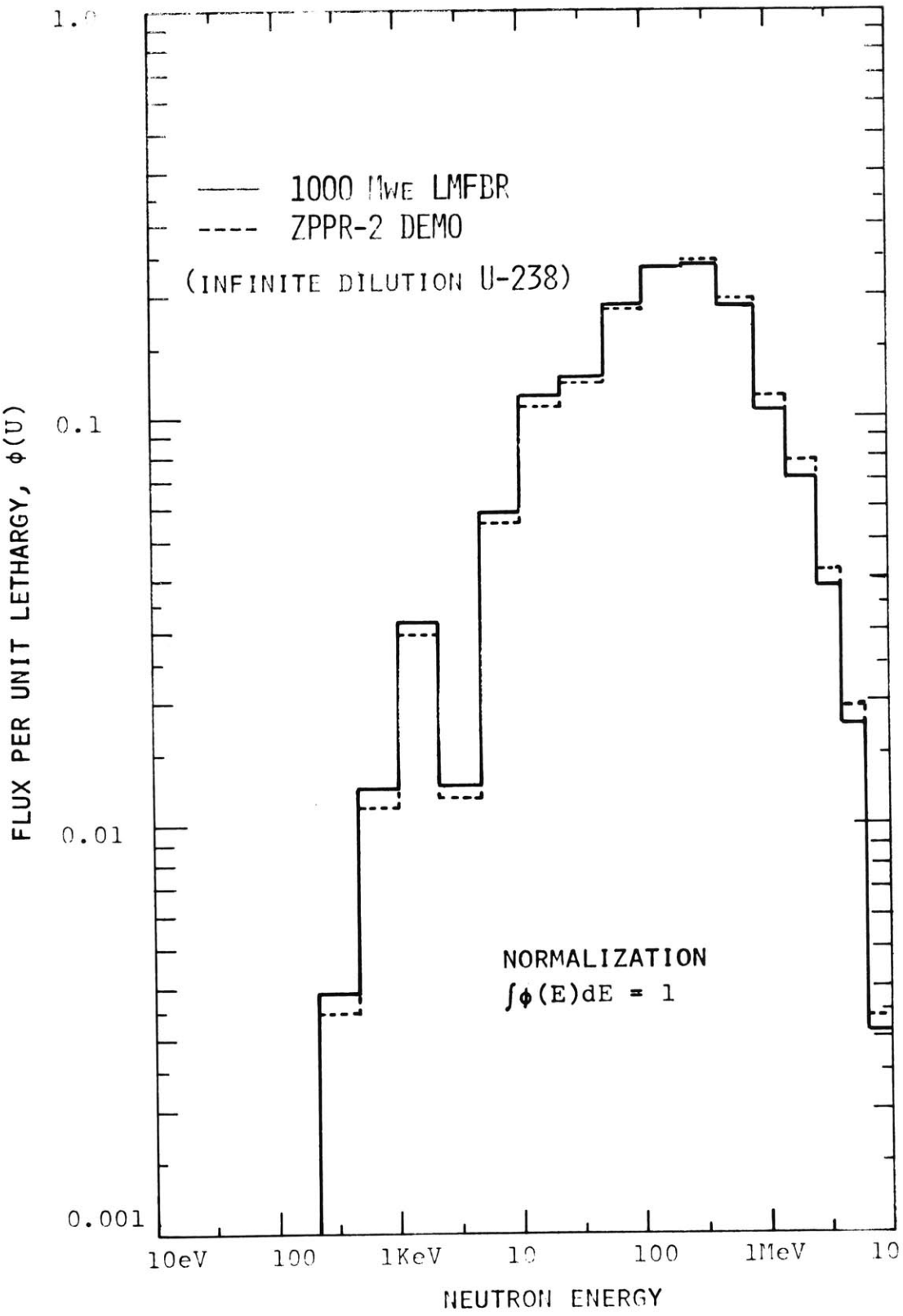

provides the harder driving spectrum. From the detailed calculations, it was found that:

(1) The BTF converter drives the blanket with a computed spectrum softer than the 1000-MWe LMFBR by about the same margin as the difference between the 1000-MWe and demo-size driving spectra.

(2) The spectrum mismatch at the core-blanket interface tends to wash out at deeper penetrations into the blanket, as evidenced by both spectrum and U^{238} capture traverse calculations.

Figure 8.7 summarizes in a succinct form the general conclusions of this investigation: The present BTF converter's soft driving spectrum is of importance comparable to that of U^{238} self-shielding in its effect upon the observed blanket spectrum. In fact, the two effects are even more inextricably linked, since self-shielding occurs primarily in the region below 1 keV. Thus, driving the blanket with a soft spectrum creates a proportionally greater demand for an accurate description of self-shielding.

8.3 Parametric Investigations for Blanket No. 3

Considerably fewer parametric investigations have been made on Blanket No. 3 than were done for Blanket No. 2. Since Blanket No. 3 is driven by the same converter, and uses the same first two rows of blanket as No. 2, many of the results carry over. In particular, calculations show that the graphite reflector of Blanket No. 3 affects primarily the adjacent blanket row, and hence none of the many variations investigated by Leung appeared to require repetition. Thus, the present study was focused upon the effect of the graphite reflection alone.

A number of obvious variables were found to have an insignificant effect: ± 10% variation in assumed graphite density about 1.66 gm/cc, inclusion of 300 ppm by weight of hydrogen (in the form of moisture), ± 10 cm variation in the extrapolated width and height (hence transverse buckling).

FIG. 8.7 SPECTRUM AT INNER EDGE OF RADIAL BLANKET

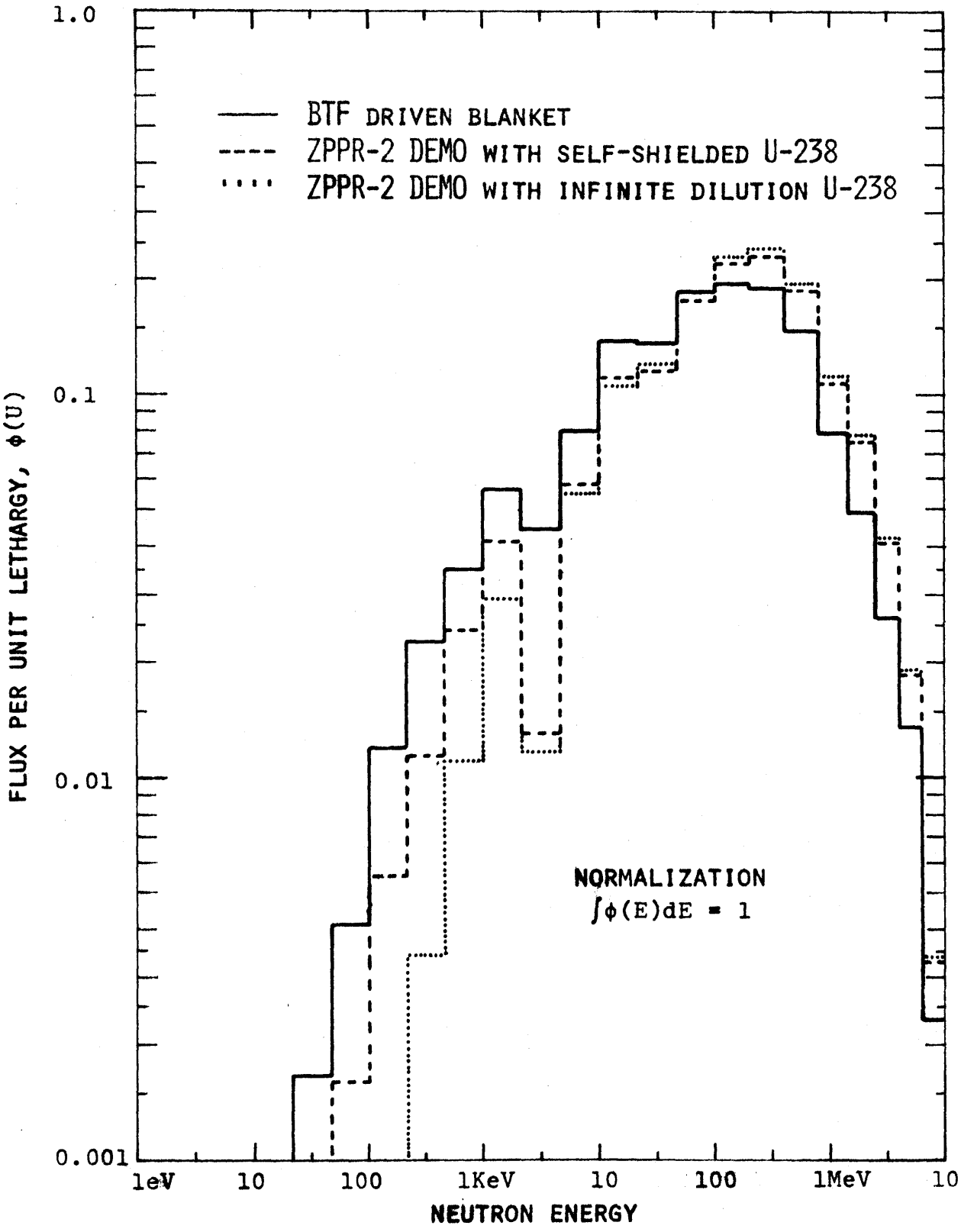

Self-shielding of both the U^{238} fuel and the detector foils was found to be an important consideration, as expected. In order to account for decreased U^{238} self-shielding at the blanket-reflector interface, the MIDI code was used to generate U^{238} cross sections for a 3.9-cm-wide interface region in the blanket. These interface-modified U^{238} cross sections are compared to the infinite-dilution and infinite-blanket-medium values in Table 8.1. Approximate cross sections were also estimated for 10-mil gold foils to match quoted effective resonance integral values for this thickness; the values adopted are shown in Table 8.2. Figure 8.8 compares the measured and calculated gold traverses with and without both Au and modified U^{238} self-shielding. In the blanket, the boundary-corrected U^{238} clearly improves the agreement; in the graphite reflector, the gold self-shielding over-corrects the traverse but at least indicates that the effect can more than account for the observed discrepancies.

8.4 Design Calculations for Blanket No. 4

Blanket Mock-Up No. 4 will use the same blanket elements and iron reflector as Blanket No. 2; however, the converter assembly will be modified to provide a harder driving spectrum, similar to the leakage spectrum from the core of a demonstration LMFBR plant.

For Blanket No. 4, the converter configuration was optimized by comparison to a reference demonstration LMFBR design. The reference design consisted of a core having composition and dimensions very similar to ZPPR Assembly 2 (the ANL Demonstration Reactor Benchmark), coupled with a radial blanket and iron reflector having the same composition and (radial) thickness as BTF Blanket Assembly No. 2.

The optimum converter design for Blanket No. 4 was found to consist of a 5-cm-thick graphite reflector region and 10 rows of UO_2 fuel. (The previous converter configuration employed for Blankets 1, 2 and 3 was 20 cm of graphite and 15 rows of UO_2 fuel.) All design calculations were made using the ANISN code and an updated version of the ABBN 26-group cross section set, with self-shielded U^{238} cross sections generated by the MIDI code.

TABLE 8.1. U^{238} Broad-Group Capture Cross Sections

Group	E_L	U^{238} Capture Cross Section		
		Infinite Dilution	Infinite Blanket Medium	3.9-cm Blanket-Reflector Interface
10	21.5 keV	0.50	0.50	0.50
11	10.0 keV	0.75	0.428	0.501
12	4.65 keV	0.78	0.626	0.809
13	2.15 keV	1.2	0.536	0.737
14	1.0 keV	2.1	0.566	0.820
15	465 eV	3.6	0.725	0.666
16	215 eV	4.5	0.633	1.114
17	100 eV	17	1.058	1.793
18	46.5 eV	15	2.894	4.973
19	21.5 eV	58	2.384	3.895
20	10.0 eV	82	6.621	10.160
21	4.65 eV	171	7.043	10.750
22	2.15 eV	0.54	0.54	0.54

TABLE 8.2. $Au^{197}(n,\gamma)Au^{198}$ Activation Cross Sections

Group	E_L (eV)	Au Activation Cross Sections	
		Infinite Dilution	10-mil Foil (Approx.)
13	2150	3.82	3.82
14	1000	9.32	7.50
15	465	16.78	8.39
16	215	23.68	9.66
17	100	24.43	9.97
18	46.5	55.97	22.84
19	21.5	15.96	6.51
20	10.0	7.83	3.20
21	4.65	1677.44	167.55
22	2.15	285.12	28.48
23	1.0	24.75	24.75

FIG. 8.8 GOLD AXIAL ACTIVATION TRAVERSES IN BLANKET NO. 3

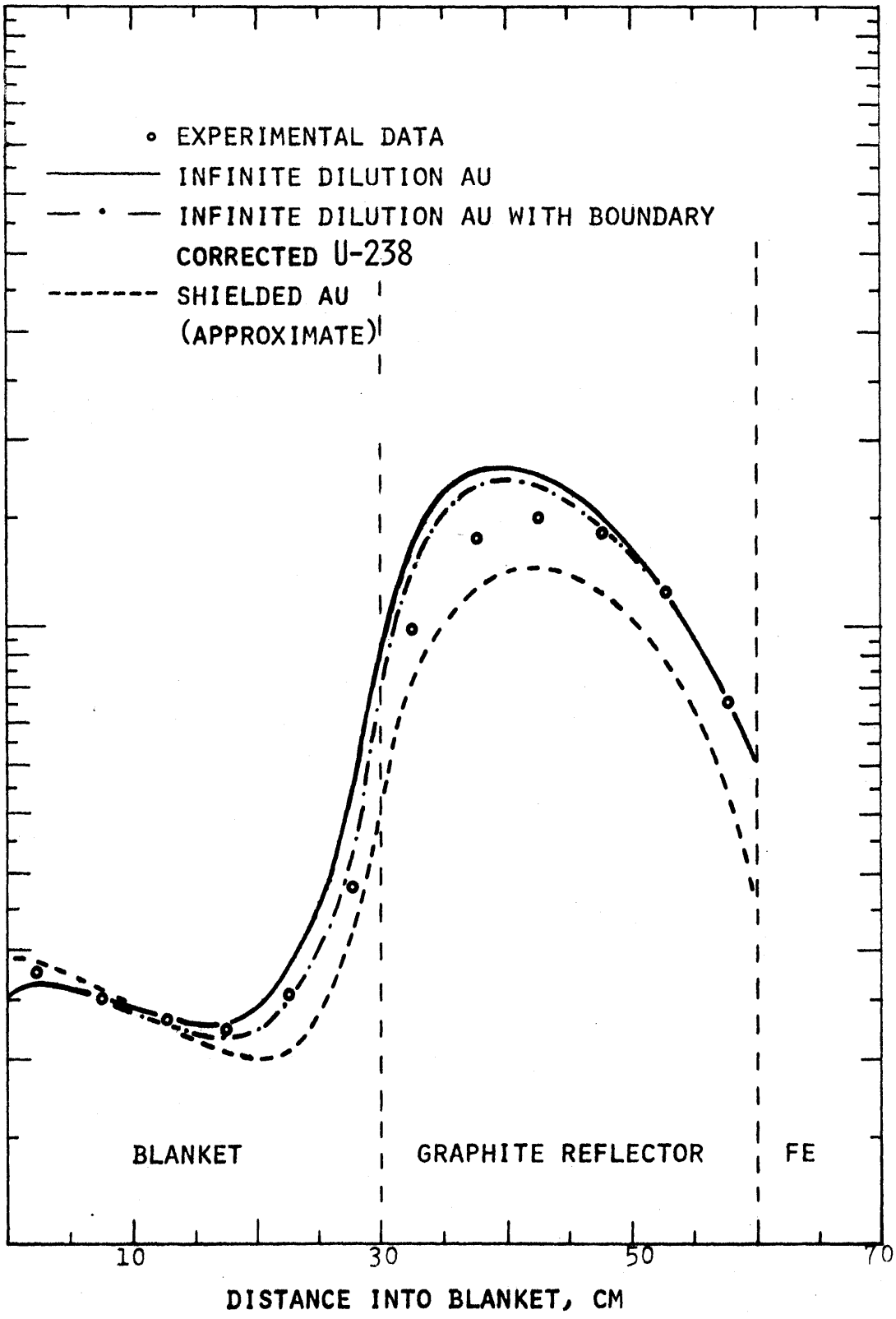

Table 8.3 compares the spectrum at the inner edge of Blanket No. 4 with that at the core-blanket interface of the ZPPR-2 reference design. Figure 8.9 shows the same data in graphical form. The agreement is seen to be good except in the neighborhood of the 3-keV sodium resonance; this is a result of the absence of sodium in the converter assembly. It can also be seen from Table 8.3 and Fig. 8.9 that the Blanket No. 4 driving spectrum is considerably harder than that of Blanket No. 2.

Table 8.4 compares the Blanket No. 4 and ZPPR-2 reference design spectra at a depth of 9.5 cm into the blanket. Figure 8.10 shows the same data in graphical form. The agreement is seen to be excellent throughout the entire energy range, save for a small discrepancy above 1 MeV.

Reduction of the converter graphite region thickness from 20 cm to 5 cm for Blanket No. 4 should also result in about a factor of three increase in fast flux over previous blanket assemblies, which will facilitate deep penetration traverse measurements in the reflector region.

8.5 Parametric Studies of Fast Neutron Penetration in the Reflector

In both the graphite reflector of Blanket No. 3 and the iron reflector of Blanket No. 2, the measured $U^{238}(n,f)$ and In (n,n') threshold detector traverses have shown far greater than calculated fast neutron fluxes: The calculated activation (which is approximately linear when plotted as log activity vs. distance) has an e-folding distance a factor of two shorter than the measured data. The following variables have been eliminated as possible causes for this discrepancy by an extensive series of parametric studies:

(1) reflector density variations;

(2) cross section set idiosyncrasies in the sense that both the HEDL and ABBN sets gave comparable results;

(3) order of quadrature: S_{16} results did not differ substantially from S_8 results;

TABLE 8.3

Neutron Spectrum at Inner Edge of Blanket

Group	ZPPR-2	Blanket No. 4	Blanket No. 2
1	0.00156	0.00168	0.00111
2	0.00888	0.00972	0.00642
3	0.0194	0.0194	0.0124
4	0.0428	0.0423	0.0280
5	0.0610	0.0568	0.0387
6	0.130	0.132	0.102
7	0.159	0.154	0.131
8	0.152	0.145	0.135
9	0.133	0.136	0.140
10	0.0878	0.0932	0.104
11	0.0844	0.0850	0.105
12	0.0442	0.0450	0.0610
13	0.00981	0.0208	0.0334
14	0.0317	0.0272	0.0430
15	0.0184	0.0157	0.0265
16	0.00937	0.00905	0.0170
17	0.00417	0.00436	0.00910
18	0.00123	0.00151	0.00316
19	0.000485	0.000554	0.00127
20	0.0000988	0.000121	0.000275
21	0.0000300	0.0000302	0.0000725
22	0.0000336	0.0000263	0.000296
23	0.0000111	0.0000152	0.000259
24	0.0000057	0.0000069	0.000134
25	0.0000020	0.0000808	0.0000348
26	0.0000005	0.0000063	0.0000040
Total	1.000	1.000	1.000

TABLE 8.4

Neutron Spectrum 9.5 cm Into Blanket

Group	ZPPR-2	Blanket No. 4
1	0.000779	0.000923
2	0.00443	0.00532
3	0.00936	0.0106
4	0.0232	0.0252
5	0.0377	0.0382
6	0.0999	0.103
7	0.142	0.141
8	0.149	0.145
9	0.143	0.142
10	0.101	0.102
11	0.103	0.103
12	0.0564	0.0564
13	0.0138	0.0140
14	0.0463	0.0457
15	0.0314	0.0304
16	0.0199	0.0193
17	0.0111	0.0109
18	0.00444	0.00443
19	0.00191	0.00193
20	0.000508	0.000514
21	0.000147	0.000148
22	0.000119	0.000119
23	0.0000777	0.0000784
24	0.0000421	0.0000426
25	0.0000165	0.0000357
26	0.0000044	0.0000082
Total	1.000	1.000

FIG. 8.9 NEUTRON SPECTRUM AT INNER EDGE OF BLANKET

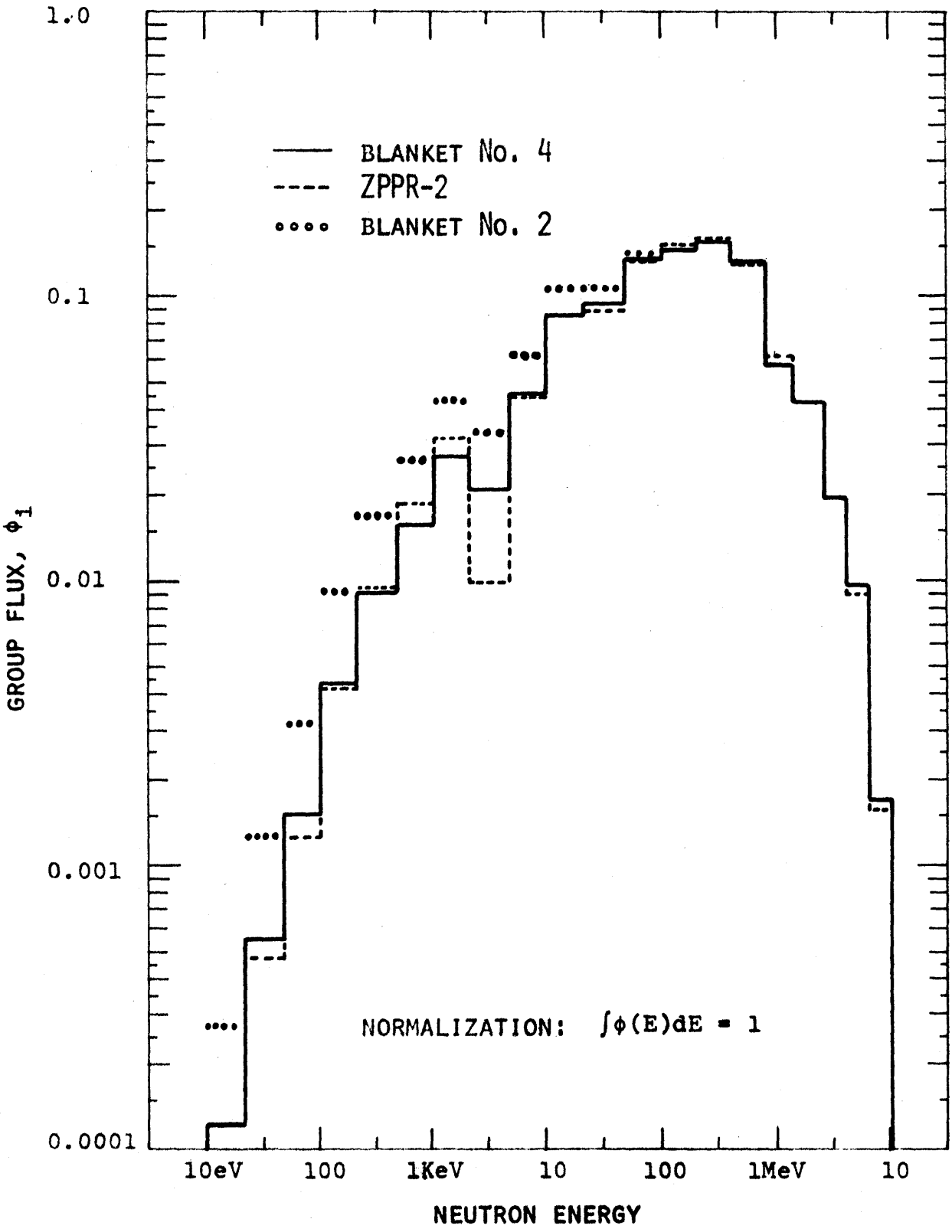

FIG. 8.10 NEUTRON SPECTRUM 9.5 cm INTO BLANKET

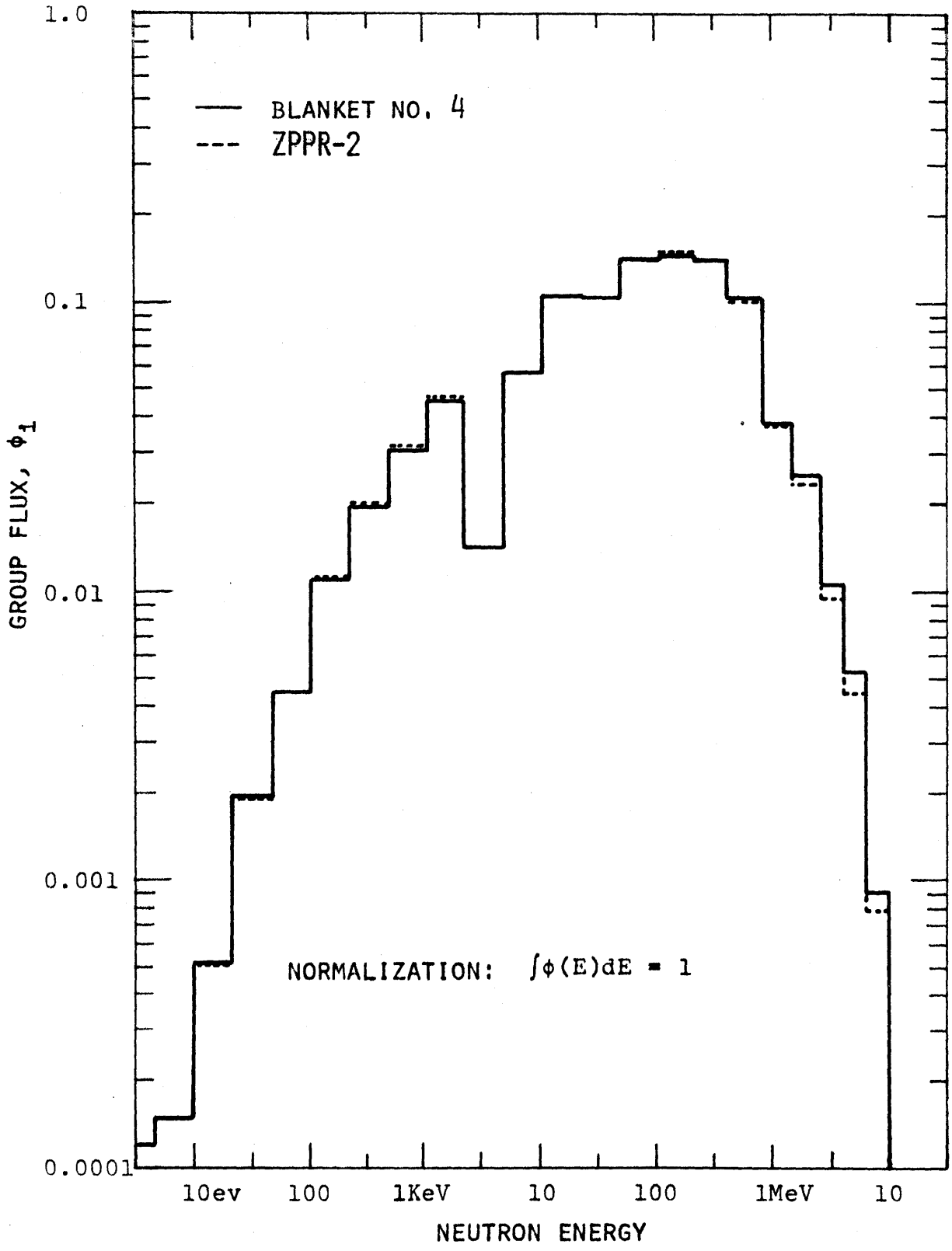

(4) variations in transverse buckling used in the 1D calculations: even setting $B_x^2 = B_y^2 = 0$ had no appreciable effect;
(5) reflector outer boundary condition;
(6) impurity content of the reflector, such as moisture in the graphite;
(7) higher-order scattering as opposed to the transport approximation;
(8) impurity content of the foil detectors (e.g., the 18-ppm U^{235} in our depleted uranium).

It is also interesting to note that the thorium (n,f) traverse in Blanket No. 3 is in acceptable agreement with the calculated results. This suggests that the problem may lie in a narrow band of neutron energies around 1 MeV where, perhaps not coincidentally, both carbon and iron have some scattering resonance fine structure in their cross sections. Two approaches are being pursued to follow up on this line of reasoning: Instrumental measurements will be made of the shape of the spectrum near 1 MeV in the iron reflector of Blanket No. 4 to see whether neutrons are in fact streaming through a window; and a numerical analysis of the cross section collapsing algorithm and weighting spectrum shape will be made to determine the adequacy of the coarse-group multigroup cross sections in the groups around 1 MeV. A thorough re-examination of experimental techniques employed for the U^{238} and In foil traverses will also be carried out.

8.6 References

(1) Abagyan, L.P., et al., "Group Constants for Nuclear Reactor Calculations," Consultants Bureau (1964).

(2) Kidman, R.B. and R.E. Schenter, "Group Constants for Fast Reactor Calculations," HEDL-TME-71-36, ENDF-143 (March 1971).

(3) Leung, T.C., et al., "Neutronics of an LMFBR Blanket Mock-Up," COO-3060-1, MITNE-127 (January 1972).

9. SUMMARY, CONCLUSIONS AND FUTURE WORK

9.1 Introduction

This is the third annual report of the LMFBR Blanket Physics Project at M.I.T. During the past year, work has been concerned primarily with the following areas:

(a) Measurements on Blanket Mock-Up No. 3, a graphite-reflected assembly, designed to test the concept of using high-albedo materials to enhance blanket performance.

(b) Evaluation of various concepts which have promise for improving blanket design and economics.

(c) Completion of the effort to acquire and apply state-of-the-art instrumental neutron spectrometry methods, and expansion of the parallel effort on foil techniques.

(c) Numerical and experimental investigations of important variables such as heterogeneity.

9.2 Discussion

The most important conclusions which may be drawn from the past year's work are as follows:

(1) The generally good agreement between experimental data and the results of multigroup calculations continues. This is particularly important in that the graphite-reflected Blanket No. 3 is as severe a test of FBR calculation methods as is likely to be encountered in practice.

(2) Fast neutron propagation in the reflector, whether in graphite or in iron, remains the area of most prominent discrepancy.

(3) Blankets Nos. 2 and 3 have been on the soft-spectrum side of the range of interest. Hence, hardening the driving spectrum is a priority item for future effort. Table 9.1 compares blanket-average U^{238} capture cross sections

TABLE 9.1. Effect of Various Factors on Average Blanket U^{238} Capture Cross Sections*

VARIABLE	% CHANGE	COMMENT
1) 1000-MWe radial blanket, BOL, 3 rows Na (or Fe) reflector	≡ 0	Reference case for all comparisons which follow.
2) Blanket thickness: 1, 2, 3 rows	~ 0	Thickness with conventional reflector has no effect on $\bar{\sigma}$ for a given row.
3) High-albedo reflector, 2-row blanket; Be (also BeO or C vs. Na (or Fe))	+9.5%	(+4.8% for 3 rows; +31% for 1 row) Being studied in Mock-Up No. 3.
4) Homogeneous (and infinitely dilute) vs. heterogeneous	+12%	Important to accurately characterize self-shielding for all blankets.
5) Burnup, EOL vs. BOL	- 12%	EOL Pu enrichment (mean) is ~2.5%; value includes effect of FP's and a - 2% shift in core enrichment.
6) Composition: axial vs. radial blanket	+17%	Fuel: coolant v/o is 30:50 for axial and 50:30 for radial blankets.
7) Driver spectrum: change in adjacent core enrichment from 1000 MWe @ ~15% to demo @ ~24%	- 7%	Axial blanket also sees comparably different core enrichment in a 2-zone core.
8) Adjacent core	- 21%	Core spectrum is much harder than blanket's.
9) U^{NAT} vs. U^{DEP}	- 3%	Approaching range where effect is hard to measure.

*Note that N and $\bar{\phi}$ also change; hence capture rate is not proportional to $\sigma^{28}_{n,\gamma}$ alone.

under various ambient conditions: As items 7 and 8 indicate, driving spectrum is of comparable importance to reflector, blanket composition, heterogeneity, and burnup effects.

9.3 Future Work

During the coming contract year, July 1, 1972 through June 30, 1973, work will be concerned mainly with the following:

(1) Completion of the documentation of the work performed on Blanket Mock-Up No. 3.

(2) Completion of the foil irradiation experiments scheduled for Blanket No. 4.

(3) Completion of the studies under way on the economic analysis of advanced blanket design performance and on the effects of heterogeneity.

(4) Further investigation of excessive fast neutron penetration in the reflector region.

(5) Expanded efforts in the area of foil methods for neutron spectrometry.

(6) Initiation of methods development for gamma heating measurements planned for Blanket No. 5.

(7) Design of reflector subassemblies for Blanket No. 5.

In general, work is evolving from an initial emphasis on acquisition of general purpose experimental capabilities, and their application, to the coming emphasis on specific experimental objectives such as gamma heating measurements and special purpose foil spectrometry. A similar evolution has occurred in the analytical effort: development followed by applications, and subsequently by a focus on specific problems. These trends will continue through the coming year.

Appendix A

BIBLIOGRAPHY OF BLANKET PHYSICS PROJECT PUBLICATIONS

In this appendix are tabulated all publications associated with work performed in the MIT Blanket Physics Project. Sc.D. theses are listed first, followed by S.M. and B.S. theses and then by other publications.

A.1 Doctoral Theses

(Also see section 3 for corresponding topical reports)

Forbes, I.A.

Design, Construction and Evaluation of a Facility for the Simulation of Fast Reactor Blankets, Feb. 1970.

Sheaffer, M.K.

A One-Group Method for Fast Reactor Calculations, Aug. 1970.

Tzanos, C.P.

Optimization of Material Distributions in Fast Breeder Reactors, Aug. 1971.

Kang, C.S.

Use of Gamma Spectroscopy for Neutronic Analysis of LMFBR Blankets, Nov. 1971.

Leung, T.C.

Neutronics of an LMFBR Blanket Mock-Up, Jan. 1972.

Ortiz, N.R.

Instrumental Methods for Neutron Spectroscopy in the MIT Blanket Test Facility, May 1972.

Brewer, S.T.

The Economics of Fuel Depletion in Fast Breeder Reactor Blankets (est. Oct. 1972).

A.2 S.M. and B.S. Theses

Ho, S.L.

Measurement of Fast and Epithermal Neutron Spectra Using Foil Activation Techniques

S.M. Thesis, MIT Nucl. Eng. Dept., Jan. 1970

Mertens, P.G.

An Evaluation of a Subcritical Null-Reactivity Method for Fast Reactor Applications

S.M. Thesis, MIT Nucl. Eng. Dept., May 1970

Westlake, W.J.

Heterogeneous Effects in LMFBR Blanket Fuel Elements

S.M. Thesis, MIT Nucl. Eng. Dept., June 1970

Shupe, D.A.

The Feasibility of Inferring the Incident Neutron Spectrum from Prompt Capture Gamma-Ray Spectra

S.M. Thesis, MIT Physics Dept., Aug. 1970

Pant, A.

Feasibility Study of a Converter Assembly for Fusion Blankets Experiments

S.M. Thesis, MIT Nucl. Eng. Dept., Jan. 1971

Passman, N.A.

An Improved Foil Activation Method for Determination of Fast Neutron Spectra

S.M. Thesis, MIT Nucl. Eng. Dept., Jan. 1971

Forsberg, C.W.

Determination of Neutron Spectra by Prompt Gamma-Ray Spectrometry

M.S. Thesis, MIT Nucl. Eng. Dept., June 1971

Brown, G.J.

A Study of High-Albedo Reflectors for LMFBR's

S.M. Thesis, MIT Nucl. Eng. Dept., March 1972

Thompson, A.M.

Activation Profiles in Reactor Fuel Elements

B.S. Thesis, MIT Physics Dept., June 1972

A.2 S.M. and B.S. Theses (continued)

Lal, D.

Determination of the Neutron Spectrum in the MITR Transistor Irradiation Facility

B.S. Thesis, MIT Chem. Eng. Dept., June 1972

A.3 Other Publications

I.A. Forbes, M.J. Driscoll, T.J. Thompson, I. Kaplan and D.D. Lanning

Design, Construction and Evaluation of a Facility for the Simulation of Fast Reactor Blankets

MIT-4105-2, MITNE-110, Feb. 1970

M.K. Sheaffer, M.J. Driscoll and I. Kaplan

A One-Group Method for Fast Reactor Calculations

MIT-4105-1, MITNE-108, Sept. 1970

I.A. Forbes, M.J. Driscoll, D.D. Lanning, I. Kaplan and N.C. Rasmussen

LMFBR Blanket Physics Project Progress Report No. 1

MIT-4105-3, MITNE-116, June 30, 1970

I.A. Forbes, M.J. Driscoll, T.J. Thompson, I. Kaplan and D.D. Lanning

Design, Construction and Evaluation of an LMFBR Blanket Test Facility

Trans. Am. Nucl. Soc., Vol. 13, No. 1, June 1970

S.T. Brewer, M.J. Driscoll and E.A. Mason

FBR Blanket Depletion Studies – Effect of Number of Energy Groups

Trans. Am. Nucl. Soc., Vol. 13, No. 2, Nov. 1970

M.K. Sheaffer, M.J. Driscoll and I. Kaplan

A Simple One-Group Method for Fast Reactor Calculations

Trans. Am. Nucl. Soc., Vol. 14, No. 1, June 1971

T.C. Leung, M.J. Driscoll, I. Kaplan and D.D. Lanning

Measurements of Material Activation and Neutron Spectra in an LMFBR Blanket Mock-Up

Trans. Am. Nucl. Soc., Vol. 14, No. 1, June 1971

A.3 Other Publications (continued)

S.T. Brewer, E.A. Mason and M.J. Driscoll

On the Economic Potential of FBR Blankets

Trans. Am. Nucl. Soc., Vol. 14, No. 1, June 1971

I.A. Forbes, M.J. Driscoll, N.C. Rasmussen, D.D. Lanning and I. Kaplan

LMFBR Blanket Physics Project Progress Report No. 2

COO-3060-5, MITNE-131, June 1971

C.P. Tzanos, E.P. Gyftopoulos and M.J. Driscoll

Optimization of Material Distributions in Fast Breeder Reactors

MIT-4105-6, MITNE-128, August 1971

T.C. Leung and M.J. Driscoll

A Simple Foil Method for LMFBR Spectrum Determination

Trans. Am. Nucl. Soc., Vol. 14, No. 2, Oct. 1971

C.S. Kang, N.C. Rasmussen and M.J. Driscoll

Use of Gamma Spectroscopy for Neutronic Analysis of LMFBR Blankets

COO-3060-2, MITNE-130, Nov. 1971

T.C. Leung, M.J. Driscoll, I. Kaplan and D.D. Lanning

Neutronics of an LMFBR Blanket Mock-Up

COO-3060-1, MITNE-127, Jan. 1972

N.R. Ortiz, I.C. Rickard, M.J. Driscoll and N.C. Rasmussen

Instrumental Methods for Neutron Spectroscopy in the MIT Blanket Test Facility

COO-3060-3, MITNE-129, May 1972

V.C. Rogers, I.A. Forbes and M.J. Driscoll

Heterogeneity Effects in the MIT-BTF Blanket No. 2

Trans. Am. Nucl. Soc., Vol. 15, No. 1, June 1972

S.T. Brewer, E.A. Mason and M.J. Driscoll

The Economics of Fuel Depletion in Fast Breeder Reactor Blankets

COO-3060-4, MITNE-123 (est. Nov. 1972)